



UNIVERSITAT POLITÈCNICA DE CATALUNYA
BARCELONATECH

Escola Politècnica Superior d'Enginyeria
de Manresa



Reuse of kaolinitic materials from several bauxite mines of Catalonia, Spain

TREBALL FINAL DE MÀSTER. MÀSTER UNIVERSITARI EN
ENGINYERIA DE MINES
ARNAU MARTÍNEZ ALCALÁ

Directores:

Maria Pura Alfonso Abella

Maria Teresa García Vallès

Agraïments

Voldria agrair a les directores d'aquest treball final de màster, Pura Alfonso Abella i Maria Teresa García Vallés, pel suport i la orientació a la hora de la realització d'aquest treball a la vegada de donar-me impuls per entrar en el món de la recerca.

Agrair al company Cristóbal Bahamonde Padilla, pel seu suport i que gràcies a ell es van trobar alguns afloraments que es trobaven amagats, sent mostres de gran interès per aquest treball.

També agrair als meus pares igualment pel suport que m'han donat de forma incondicional.

Finalment, aquest treball s'ha realitzat a partir del projecte presentat per la obtenció de *Beques de Col·laboració d'estudiants en departaments universitaris destinades a estudiants que vagin a finalitzar els estudis de Grau o que estiguin cursant primer curs de Màsters universitaris oficials (curs 2021-2022)*, amb Resolució de la Secretaria d'Estat d'Educació presentat en el BOE núm 132, de 3 de juny de 2021, amb resolució de la Comissió d'Ajuts Universitaris el dia 15 de desembre de 2021.

Index

Abstract	4
Resum.....	5
Resumen.....	6
Introduction	7
Localization.....	8
Geology	10
Materials and methods	12
Materials	12
Analytical methods.....	14
Results and discussion.....	16
Chemical Composition	16
Mineralogical composition.....	19
Rheological properties	23
Plasticity	23
Thermal properties.....	24
ATD-TG	24
Dilatometry	26
Dilatometric coefficient.....	28
Hot stage microscopy (HSM) or optical dilatometry.....	28
Density.....	30
Technological properties.....	31
Gresification curves.....	31
Colorimetry	34
Conclusions	36
References.....	37
Annex.....	43
Sample localization/field description.....	44

XRF Calibration	49
Chemical Composition	60
Mineralogy	61
Thin plate.....	61
Mineralogical composition.....	70
FTIR.....	71
Thermal Properties.....	74
ATD-TG	74
Dilatometry	79
HSM	80
Technological Properties.....	87
Gresification curves.....	87

Abstract

Bauxitic materials from outcrops, dumps and tailings often contain high amounts of kaolinite that is susceptible to be exploited. This study provides a characterization of materials from outcrops, tailings and dumps of two abandoned bauxite mines located close to Sant Joan de Mediona and Peramola, Catalonia, Spain. Mineralogy was determined by X-ray powder diffraction (XRD) and Fourier transform infrared spectroscopy (FTIR). Thermal properties were measured by differential thermal and thermogravimetric analysis (DTA-TG), and dilatometry. The crystalline phases are 25-68 mass% of kaolinite, 15-54 mass% of boehmite, 10-15 mass%, hematite and minor amounts of anatase. Kaolinite has a medium-high crystallinity, with a Hinckley Index of 0.51-1.39. DTA show two endothermic peaks produced by the deshydroxilation of minerals; the first peak, at 527-538 °C, belongs to boehmite and the second peak, at 564-570 °C, corresponds to kaolinite. An exothermic peak, at 950-978 °C, is associated with the mullite crystallization. TG curves show a total mass loss from 10 to 13 mass%. The FTIR spectra show the characteristic peaks of kaolinite at 3696 and 3620 cm⁻¹, corresponding to structural water and Al-OH stretching, the 1100 and 990 cm⁻¹ bands corresponding Si-O stretching, a 920 cm⁻¹ band represents the Al-OH bending vibrations, and the 790 to 750 cm⁻¹ bands are attributed to OH deformation. Boehmite bands at 3295 and 3090 cm⁻¹ correspond to Al-OH stretching, at 1160 and 1067 cm⁻¹ are produced by H-O-H stretching and at 624 and 490 cm⁻¹ are caused by the Si-O-Al stretching. The dilatometric analysis show a shrinkage at 530-550 °C, which is produced by the loss of OH⁻ groups, at 550-580 °C the transformation of α to β-quartz is recorded, at 875 °C the transformation into spinel structure occurs, and around 1010 °C mullite is formed. The thermal coefficient of expansion ranges from $3.8 \cdot 10^{-6}$ to $7.3 \cdot 10^{-6} \text{ } ^\circ\text{C}^{-1}$. The viability of these resources as ceramic raw materials is limited because of their low amounts of phyllosilicate minerals, low plasticity and high working temperatures. Even so, their use as raw materials of Portland cement substitutes is possible however it has to be studied in further investigations.

Resum

Els materials bauxítics procedents d'afloraments, runams i estèrils soLEN contenir elevades quantitats de caolinita susceptibles de ser explotades. Aquest estudi proporciona una caracterització de materials procedents d'afloraments, estèrils i runams de dues mines de bauxita abandonades situades prop de Sant Joan de Mediona i Peramola, Catalunya, Espanya. La mineralogia es va determinar mitjançant difracció de raigs X (DRX) i espectroscòpia infraroja per transformada de Fourier (FTIR). Les propietats tèrmiques es van mesurar mitjançant anàlisi tèrmic diferencial i termogravimètric (ATD-TG), i dilatometria. Les fases cristal·lines són 25-68% en massa de caolinita, 15-54% en massa de boehmita, 10-15% en massa, hematites i quantitats menors de anatasa. La caolinita té una cristal·lització mitjana-alta, amb un índex de Hinckley de 0,51-1,39. El ATD mostra dos pics endotèrmics produïts per la deshidroxilació dels minerals; el primer pic, a 527-538 °C, pertany a la boehmita i el segon, a 564-570 °C, correspon a la caolinita. Un pic exotèrmic, a 950-978 °C, està associat a la cristal·lització de la mullita. Les corbes TG mostren una pèrdua de massa total del 10 al 13% en massa. Els espectres FTIR mostren els pics característics de la caolinita en 3696 i 3620 cm⁻¹, corresponents a l'aigua estructural i a l'enllaç Al-OH, les bandes de 1100 i 990 cm⁻¹ corresponents a l'enllaç Si-O, una banda de 920 cm⁻¹ representa les vibracions de flexió Al-OH, i les bandes de 790 a 750 cm⁻¹ s'atribueixen a la deformació OH. Les bandes de boehmita a 3295 i 3090 cm⁻¹ corresponen a l'enllaç Al-OH, a 1160 i 1067 cm⁻¹ són produïdes per l'enllaç H-O-H i a 624 i 490 cm⁻¹ són causades per l'enllaç Si-O-Al. Els anàlisis dilatomètrics mostren una contracció a 530-550 °C, que es produeix per la pèrdua de grups OH⁻, a 550-580 °C es registra la transformació de α a β -quars, a 875 °C es produeix la transformació en estructura espinela, i al voltant de 1010 °C es forma mullita. El coeficient tèrmic de dilatació oscil·la entre $3,8 \cdot 10^{-6}$ i $7,3 \cdot 10^{-6}$ °C⁻¹. La viabilitat d'aquests materials com a matèries primeres per a ceràmiques és limitada a causa de les baixes quantitats de fil·losilicats, la baixa plasticitat i les altes temperatures de treball. Tot i això, el seu ús com a matèries primeres de substituts del ciment Portland és possible, encara que ha d'estudiar-se en posteriors recerques.

Resumen

Los materiales bauxíticos procedentes de afloramientos, escombreras y estériles suelen contener elevadas cantidades de caolinita susceptibles de ser explotadas. Este estudio proporciona una caracterización de materiales procedentes de afloramientos, estériles y escombreras de dos minas de bauxita abandonadas situadas cerca de Sant Joan de Mediona y Peramola, Cataluña, España. La mineralogía se determinó mediante difracción de rayos X (DRX) y espectroscopia infrarroja por transformada de Fourier (FTIR). Las propiedades térmicas se midieron mediante análisis térmico diferencial y termogravimétrico (ATD-TG), y dilatometría. Las fases cristalinas son 25-68% en masa de caolinita, 15-54% en masa de boehmita, 10-15% en masa, hematites y cantidades menores de anatas. La caolinita tiene una cristalinidad media-alta, con un índice de Hinckley de 0,51-1,39. El ATD muestra dos picos endotérmicos producidos por la deshidroxilación de los minerales; el primer pico, a 527-538 °C, pertenece a la boehmita y el segundo, a 564-570 °C, corresponde a la caolinita. Un pico exotérmico, a 950-978 °C, está asociado a la cristalización de la mullita. Las curvas TG muestran una pérdida de masa total del 10 al 13% en masa. Los espectros FTIR muestran los picos característicos de la caolinita en 3696 y 3620 cm⁻¹, correspondientes al agua estructural y al enlace Al-OH, las bandas de 1100 y 990 cm⁻¹ correspondientes al enlace Si-O, una banda de 920 cm⁻¹ representa las vibraciones de flexión Al-OH, y las bandas de 790 a 750 cm⁻¹ se atribuyen a la deformación OH. Las bandas de bohemita a 3295 y 3090 cm⁻¹ corresponden al enlace Al-OH, a 1160 y 1067 cm⁻¹ son producidas por el enlace H-O-H y a 624 y 490 cm⁻¹ son causadas por el enlace Si-O-Al. Los análisis dilatométricos muestran una contracción a 530-550 °C, que se produce por la pérdida de grupos OH-, a 550-580 °C se registra la transformación de α a β-cuarzo, a 875 °C se produce la transformación en estructura espinela, y alrededor de 1010 °C se forma mullita. El coeficiente térmico de dilatación oscila entre $3,8 \cdot 10^{-6}$ y $7,3 \cdot 10^{-6} \text{ } ^\circ\text{C}^{-1}$. La viabilidad de estos materiales como materias primas cerámicas es limitada debido a las bajas cantidades de filosilicatos, la baja plasticidad y las altas temperaturas de trabajo. Aun así, su uso como materias primas de sustitutos del cemento Portland es posible, aunque debe estudiarse en investigaciones posteriores.

Introduction

Climate change represents one of the major problems currently affecting the world is. One of the main causes of this change is the high amounts of CO₂ that are continuously emitted into the atmosphere (Rehan & Nehdi, 2005). Therefore, the measures to be taken to mitigate this change, those aimed at reducing CO₂ emissions as much as possible are a priority. In this respect, it should be borne in mind that a significant percentage of the CO₂ emissions is produced by the cement industry. Concrete is a widely consumed material in the world, with production of approximately 26Gt per year (Miller et al., 2018). Between 6-8% of CO₂ emissions are produced by the cement industry (M. Schneider et al., 2011). Between 60-85% of these emissions are due to the decomposition of limestone, which is the main component of the cement formula, during heat treatment and combustion of fossil fuels in the pyroprocessing unit (Benhelal et al., 2021; de Brito and Kurda, 2021; Sanjuán et al., 2020). It is therefore urgent to find cleaner ways of manufacturing cement, in line with the Paris Agreement targets of zero net carbon emissions by 2050 (Fennell et al., 2022)

Alternative binders to Portland cement are now beginning to be developed that are manufactured in a way that does not produce such high CO₂ emissions. A wide literature Examples of such binders under development include fly ash/natural pozzolan-based cement and clay-based cements (Assi et al., 2018; Fransen et al., 2021). However, in recent years, granulated blast furnace slag and coal fly ash, which are currently in significant shortage (Li et al., 2022). Therefore, there is a need to explore novel and sustainable cementitious materials.

Kaolin is considered of great economic interest due its viability to be used as a raw material to make agglomerate materials that can partially substitute the Portland cement and then, they can contribute to reduce the CO₂ emissions produced during cement fabrication (Di Mare et al., 2021; Negrão et al., 2021).

Kaolin can be used as a supplementary cementitious material added to the conventional Portland cement to reduce the CO₂ emissions or as an alternative cementitious material due its reactivity properties when is heated and transformed into metakaolin (Mañosa et al., 2022). The use of kaolin to obtain low emissions concretes was highly studied during this decade. Some cases are the use of Egyptian kaolin to obtain a geopolymmer concrete (Abbas et al., 2020), or as substitute of cement together with limestone (Du and Pang, 2020). Kaolinitic clays show high pozzolanic reactivity after heat treatment, while some other clay minerals, such as montmorillonite and illite, show low reactivity or even remain inert after heating, thus, kaolinite is the most efficient for binder applications (Baki et al., 2022).

In addition, it should be considered that kaolin already has many traditional applications, such as in ceramics, pharmaceutical and medical applications (Murray, 2000; Prasad et al., 1991). Therefore, finding new kaolin reserves is of high importance. For this purpose, different

possible sources have to be considered. Among these are bauxite deposits, which usually contain high kaolin amounts. The abundance of kaolinite in these materials enables them to be used for the manufacture of ceramics by addition of other clays or for obtaining geopolymers.

Another important aspect for the environmental protection is the need for a low generation of mining wastes; in this respect, the use of materials from mining wastes contributes to the waste removal from the environment, where they produce various types of impacts. On the other hand, this reduces the volume of materials that must be extracted from their natural position and thus reduces the energy required for extraction and the formation of new waste.

In Catalonia there is a limited amount of kaolinitic resources. These are largely found in the south, near the border with the Valencian and Aragonese communities (Garcia-Valles et al., 2020, 2022). It is therefore also necessary to consider the possible sources of kaolin obtained from bauxite deposits. In the north-east of Spain multiple occurrences of bauxitic materials have been reported, a general presentation is shown in some reports (Closas i Miralles, 1949; Galán, 1981; Molina, 1991), others are dedicated to a specific area, such as La Llacuna (IGME, 1972; Romero & Prats, 1995), the Catalan Coastal ranges (Reinhardt et al., 2018), and from the Teruel zone (Yuste et al., 2015, 2017). Some of these mineralisations are large enough to be considered exploitable, however the scale of these deposits is generally small. Some bauxite deposits were mined in the past, leaving a large accumulation of wastes in their surroundings. Much of this waste may still be of economic interest. This is important because of the many applications of bauxite and kaolinitic materials today.

The bauxite mining tailings studied are localised in Catalonia, near the Peramola and Sant Joan de Mediona villages. Both were exploited until the 20th century. The aim of this work is to characterise the materials of these bauxite dumps to determine their ability for possible industrial applications.

Localization

The study area is located at Catalonia, north of Spain (Figure 1). Two areas in this region have been selected for this study, one of them is Peramola, situated at the south part of Pyrenees, near Oliana (Figure 1) and the other is Sant Joan de Mediona, which is located in the Prelitoral range, near Igualada (Figure 1). The access to the sampling points can be done by car through a path until the final part of the approach. The main dumps are most accessible materials, and to reach outcrops of bauxitic materials it is necessary to move forward through some trails that in some cases could be more difficult to access, as the case of some outcrops of Peramola samples.

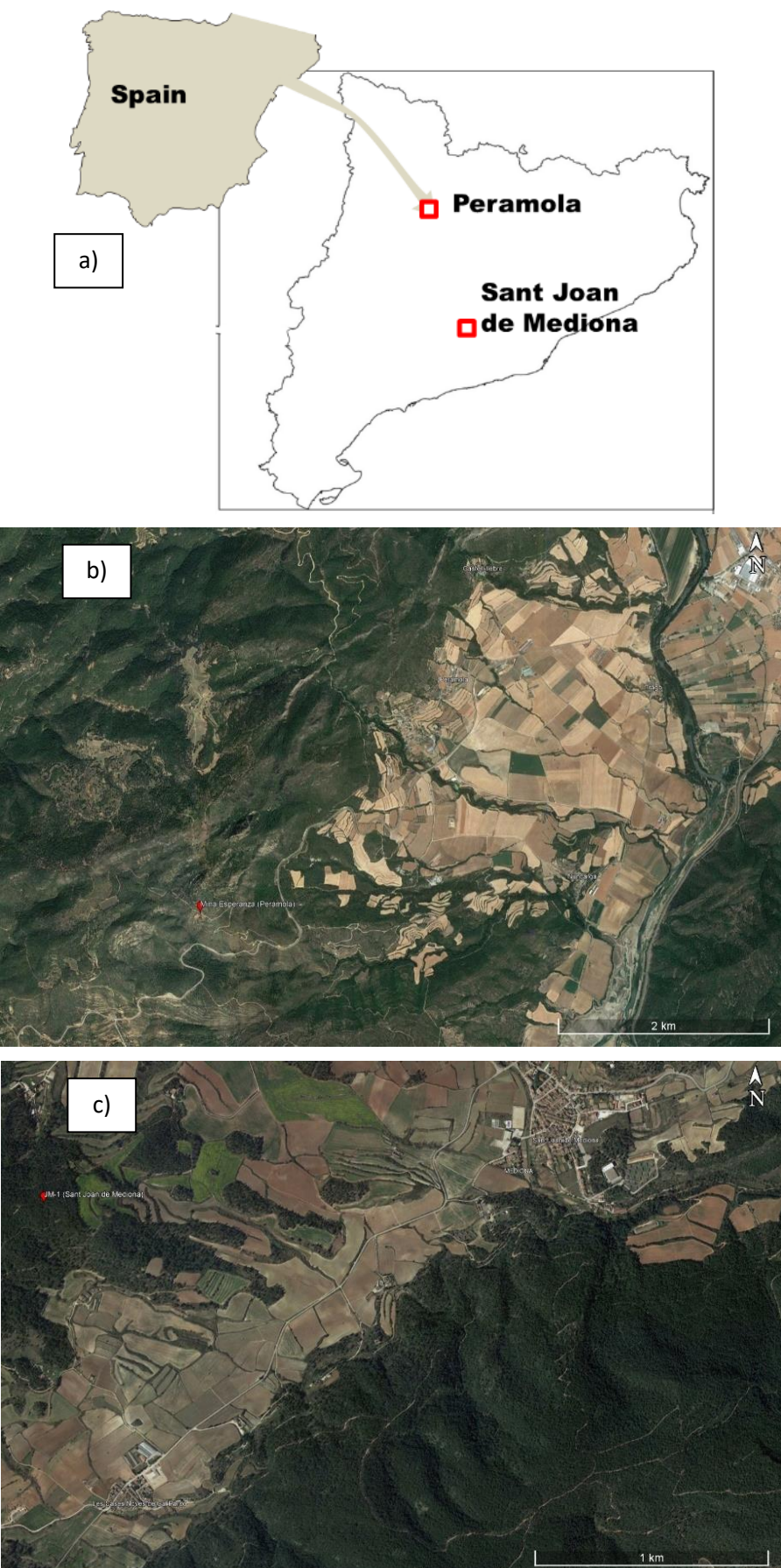


Figure 1. Localization of the study areas. a) Regional localization. b) Peramola localization. c) Sant Joan de Mediona localization.

Geology

In Catalonia there are several locations with bauxite mineralisation. All of them have a karstic origin. The deposits occur in the contact of carbonate rocks of Mesozoic age with tertiary materials. They are close to the limits of the Ebro Basic with the Catalan Coastal Ranges or the southern Pyrenees. The Peramola bauxites are located in the South-Central Unit of the Pyrenees. This unit is divided from north to south, into the Boixols, Montse and Sierras Marginales sub-units (Vergés and Muñoz, 1990), being the Peramola bauxites in the Sierras Marginales sub-unit. The Sierras Marginales unit is composed of Mesozoic rocks overlain by Tertiary detrital rocks.

The Permola bauxites occur in the boundary between the SW end of the Oliana anticline, and the Middle Jurassic materials (Lias). This is a boundary formed through complex thrust tectonics. This specific boundary corresponds to the Segre thrust, which delimits the South-Central Unit of the Pyrenees with the Ebro depression (Burbank et al., 1992). The Oliana anticline is oriented NNE-SSW and constituted by Eocene materials. The materials in the area correspond to Jurassic limestones of the Lias period, followed by massive dolomites of Dogger age and limestones and marls from Malm age. They are covered by Upper Cretaceous rocks. These materials are in tectonic contact with materials from the middle Eocene, corresponding to the Igualada marls, of Bartonian age, which are found in the core of the Oliana anticline (Burbank et al., 1992). In the study area above them are Upper Eocene detrital materials, formed by ochre-coloured sandstones and clays from the Priabonian. These materials grade towards the west to coarser materials, with conglomerates coming to the surface. Massive alluvial conglomerates appear on top of them. The Peramola bauxites (Figure 2) are hosted in limestones from the Middle Jurassic (Closas i Miralles, 1954; Molina, 1991). At this site, the thickness of the bauxite layers is variable, from few cm to 10 m.

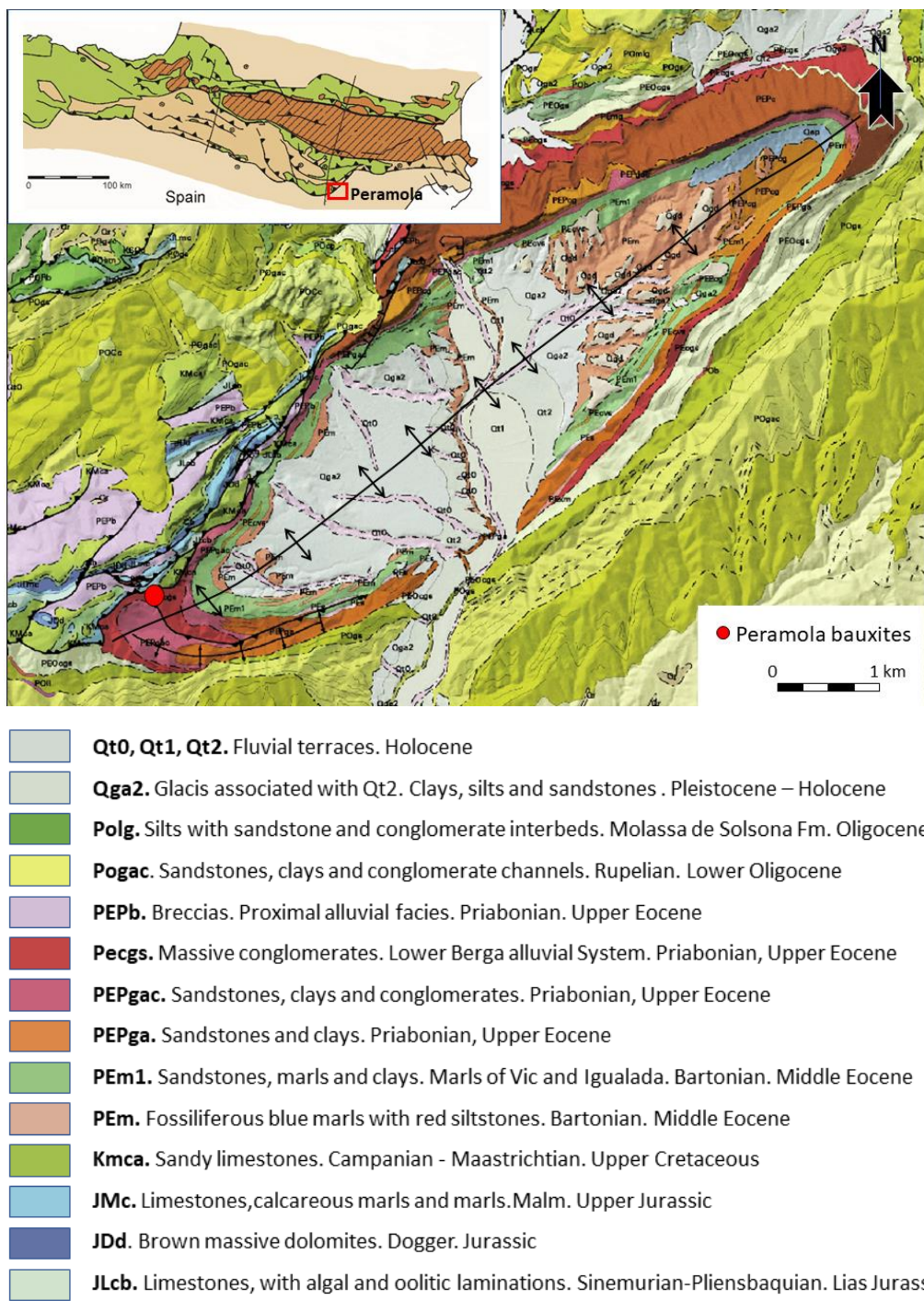


Figure 2. Geological map of the Oliana anticline, woth the location of the bauxite from Peramola. Inset image of the Pyrenees with the location of the main map.

The bauxites of Sant Joan de Mediona are located in the Prelitoral range. This is an area with abundant evidence of bauxites, including those of La Llacuna, Santa Maria de Miralles and Sant Quintí de Mediona. In this area the bauxites are found in karstic pockets within Mesozoic carbonate materials, which in some cases correspond to the Lower Muschelkalk and in others to the Upper Muschelkalk (Molina, 1991), and even in the Keuper units (Closas i Miralles, 1954) , such as the Sant Joan de Mediona (Figure 3).

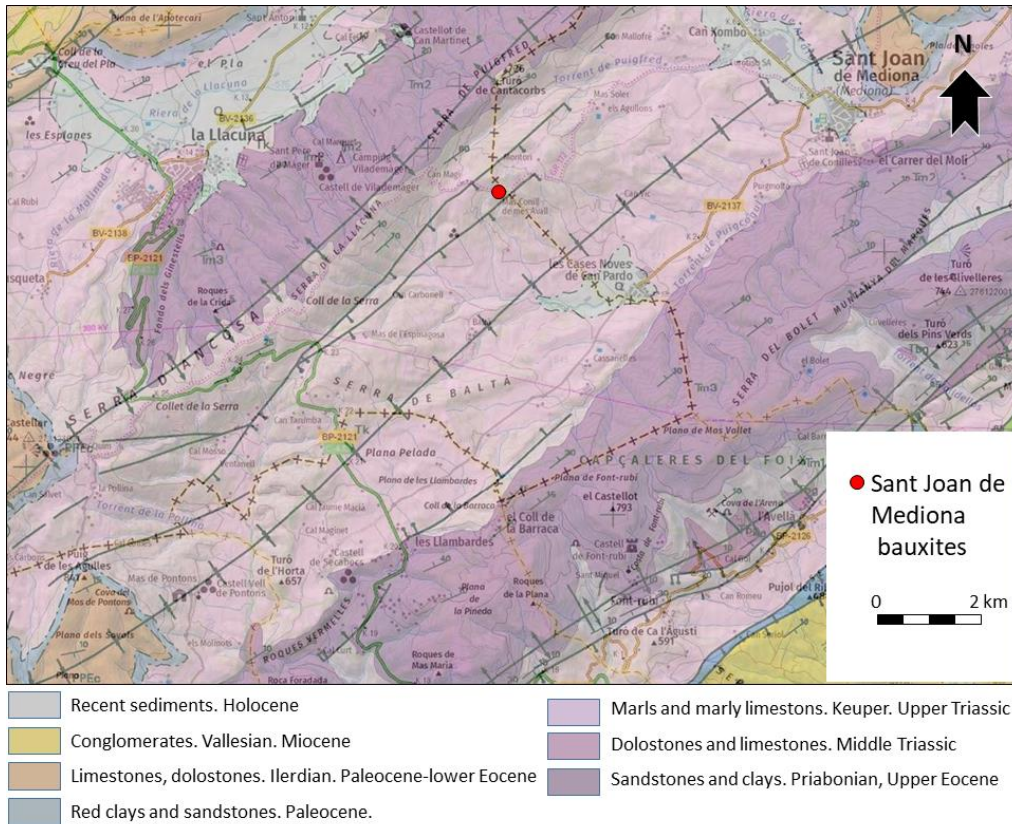


Figure 3, Geological map of the Sant Joan de Mediona bauxites.

Materials and methods

Materials

The bauxitic materials studied come from two old bauxite mines in Catalonia. The Esperanza mine from Peramola, is located in the Pre-Pyrenean range while the mine from Sant Joan de Mediona is in the Prelitoral range, both located at the limit of these units with the Ebro depression. In the both cases the sample have been obtained by aggregating material from different points so the sample is representative of whole waste or the geological unit in which the deposit is located (Ordoñez, 1977).

The materials obtained from the field can be divided first of all by area, using the prefix PER for the materials from Peramola and JM for the materials form Sant Joan de Mediona. Peramola samples were taken from a gallery of Esperanza mine, from dumps of this mine and from bauxite outcrops in the nearby area from the mine entrance (Figure 4). The Esperanza mine has been exploited by means of small galleries and trenches. The type of materials found at the area are grey sandstones and yellow and brown clays, with spots of conglomerates (Figure 5). The samples taken have different origins. On one hand, some of them, PER-1, PER-3, PER-12, PER-14 and PER-15, come from dumps created during the operation of Esperanza mine. There have been spotted three different dumps. The first one is located in front of the gallery

entrance from mine, samples PER-3 and PER-14-2, these materials. The second one can be found nearly 20m below the gallery entrance, where probably the material from the mine was taken to be prepared for its transportation. The samples taken there are PER-1 and PER-15, being materials mixed with organic materials as plants. Also, at that point an outcrop could be spotted. The third one can be found in upper levels, between the mine entrance and the upper outcrops. The materials are distributed heterogeneously through the area, some of them are spotted at a side of the path of access, were PER-12 was taken. On the other hand, up to three outcrops could be found, the biggest one, PER-10, is located at the top side of the mountain. PER-10 V is a red material, PER-10B is a white material and PER-10G is a yellow material in contact with the white material, and this one is in contact with the red material. Near the first outcrop is located the second one, PER-11, being PER-11A the material spotted at the front side of the outcrop and PER-11B the material at the back side of the outcrop. Finally, material from inside the mine gallery was taken, PER-2 and PER-14-3. The material found there had large amount of clay and crystals of calcite could be spotted.

In the case of Sant Joan de Mediona, materials were taken from different outcrops. They belong to the area of la Llacuna, where the first bauxitic deposits from Spain were reported. Sant Joan de Mediona samples have been taken from abandoned dumps and from an outcrop close to the underground activity were extracted during the life of the mine.

The outcrop and the dumps from where the samples have been taken have a relatively small scale, being difficult to be industrially exploited.

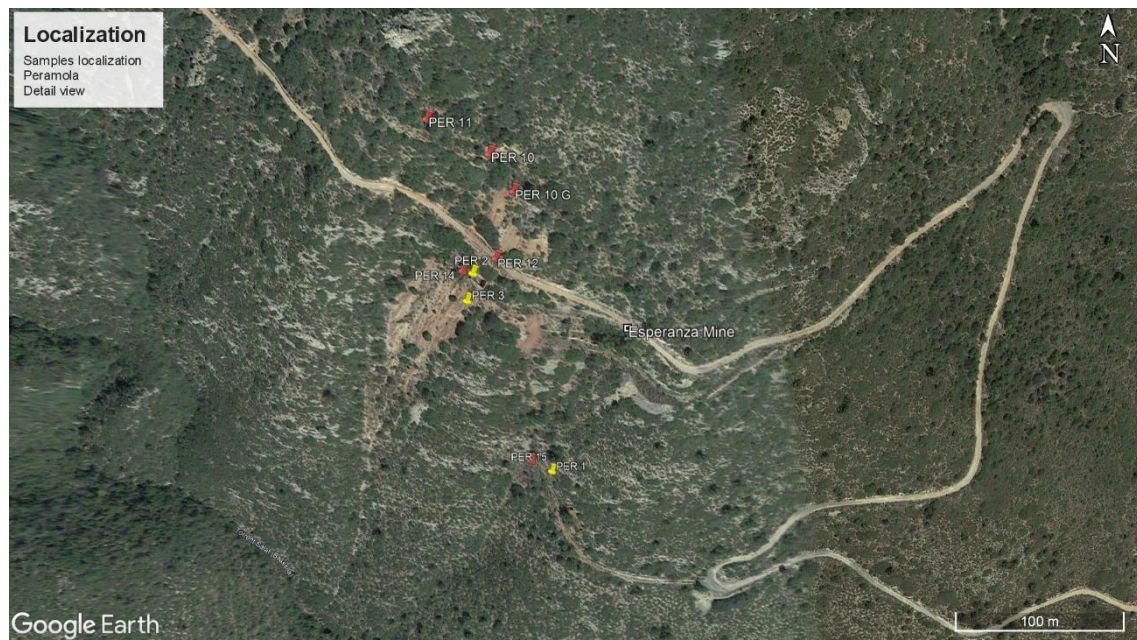


Figure 4. Localization of samples of Peramola bauxites.

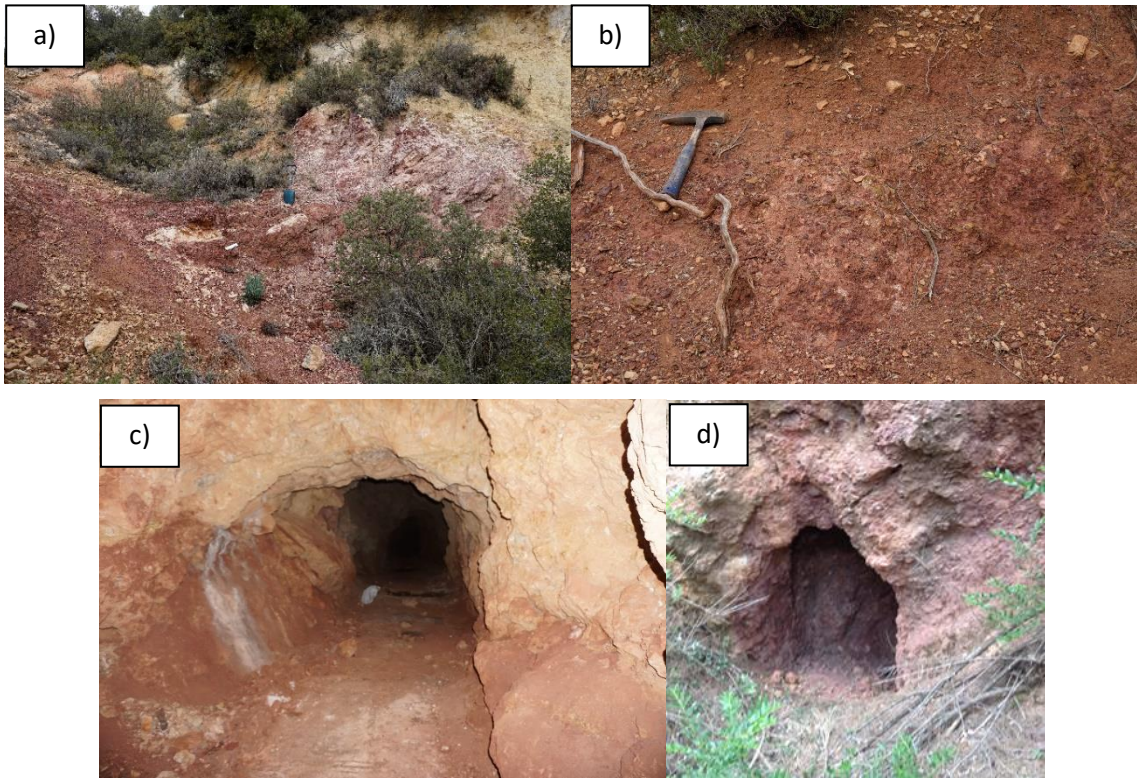


Figure 5. Pictures of places from samples were taken. a) PER-10, b) PER-11, c) PER-2 and PER-14-3, d) JM.

Analytical methods

The chemical composition was obtained by Inductive coupled analysis (ICP) in the ALS Global laboratories. Additional chemical analyses have been made with X-ray Fluorescence (XRF) with an Epsilon 1 equipment of Malvern Panalytical company, detecting from Na to Am. Thanks to this device standardless analysis could be done for a first approach to the materials composition when this were unknown. The standardless analysis are possible thanks to the software of the device, with previous theoretical standards loaded. The results given by this automatic analysis sometimes is not enough to achieve good results for elements quantification, in that case is important to create standards to generate a program of analysis for the specifics materials that have to be analysed. Due to the similarity of some samples could be useful generate an specific analysis program with its own standards. For this reason, is necessary to have some samples previously analysed through other analytical methods. After knowing the composition of the standards in order to know how much difference exist between the chemical composition obtained from a trusted laboratory and the EPSILON 1 XRF equipment. The results given by the automatic program of the XRF devise are similar as the results obtained by ICP, the standards have to be prepared. It has been necessary check the different compositions from 5 to 10 samples.

Between them, the elements of interest such as silica, aluminium and iron, have to be represented with multiples concentrations, from the lower levels until the maximum concentration that could be found. Having the multiples standards with enclosed limits and others values between the limits, the calibration for a specific analytical program could be carried out. Ich standard is introduced into the device where it will be analysed while the known concentrations are introduced into the software, which will correlate the signal of cps/eV detected and the concentrations introduced. After all the standards have been introduced into the software, to end with calibration program, the final step is creating a correlation line for ich element. Finally, the calibration program for these specific materials can be considered done and to prove the calibration is have been done correctly, some samples of known composition are analysed and the results are compared, if they are the same the calibration can be considered correct.

Mineralogy of the materials sampled was determined by X-ray powder diffraction (XRPD) using oriented aggregates. Fourier transform infrared (FTIR) and scanning electron microscopy (SEM) completed the characterization. XRPD measurements were taken using an automatic X'Pert PANalytical diffractometer with graphite monochromator, automatic gap, K α -radiation of Cu at $\lambda = 1.54061 \text{ \AA}$, powered at 45 kV and 40 mA, scanning range 4–100° with a 0.017° 20 step scan and a 50 s measuring time. In addition, oriented aggregates of the samples were prepared following the standard XRPD procedures (Moore and Reynolds, 1989). Calculation of the Hinckley crystallinity index of kaolinite was obtained according to (Plançon et al., 1988). The XRD patterns were obtained for oriented samples after the following pre-treatments: air drying at room temperature, saturation with ethylene glycol and after heating 550 °C for 1 h (Moore and Reynolds, 1989). Identification and semiquantitative evaluation of phases were made on PANanalytical X'Pert HighScore software, Version 2.0.1.]. FTIR spectra were obtained using a 2000 FTIR Perkin–Elmer spectrometer. Vibrational spectra were obtained in the 400–4000 cm⁻¹ range. Back-scattered electron images and qualitative chemical analyses of the kaolin samples were obtained using a Hitachi TM-1000 table-top SEM equipped with an energy dispersive X-ray spectrometer (EDS).

Plasticity was determinate by the Atterberg limits: liquid limit (LL), plastic limit (PL) and plasticity index (PI), using the Casagrande Cup test following the method described in Spanish standards (AENOR, 1976, 1993) standards.

Thermal analyses of samples were obtained by simultaneous Differential Thermal Analysis and Thermogravimetry (DTA–TG), using a TASCH 414/3 equipment. Analyses were carried out in the temperature range from 25 to 1300 °C under air atmosphere, at a constant flow rate of 80 mL/min, in an alumina crucible and at a heating rate ramp of 10 C/min. The sample analysed was about 150 mg of powder. The dilatometric curves of the raw samples were measured using a L76/1550 Linseis dilatometer. The test was carried out from room temperature to 1300 °C, at

a heating rate of 10 C/min and cooling was registered in a static-air atmosphere. Dilatation coefficient connect volumetric variation and temperature variation. To calculate it for ceramics, and fired clays it is used the expression (1).

$$\alpha_{phys}(k) = \frac{1}{L_0} * \frac{d(\Delta L_k)}{dT} ; K = (1 \dots N) \quad (1)$$

Where: L_0 is the dilatation of the sample at 20°C; and ΔL_k : is the variation of dilatation for a T_k temperature

To determine the water absorption and linear shrinkage tests pieces have been made following the UNE-EN ISO 10545-3 standard (AENOR, 2018). Firstly, the raw bauxitic clays were air-dried and then oven-dried up to 105 °C. Then test pieces of 10x6x1 cm were prepared. These pieces were sintered in an electric furnace at several temperatures between 1050 and 1300 °C. The increase of temperature was at a rate of 1 °C from room temperature to 70 °C and at 1.5 °C up to the sintering temperature, where a holding time of 120 min was applied before cooling. The textures in the test pieces were observed by SEM.

The firing curves were obtained from the dilatometric data following the method indicated in (Vasić et al., 2017). The colour properties were measured in the fired samples using a CM-700d Konica-Minolta spectrophotometer over the visible range(Garcia-Valles et al., 2022) .

Results and discussion

Chemical Composition

Chemical composition of samples is presented in

Table 1. SiO₂ content is ranges between 10,39 and 48.00 mass%, except or one sample of 7.91 mass%. The Al₂O₃ content vary between 10.42 and 59.67 mass%. Alkali content is very low in the two locations, with. Na₂O ranging between 0.04 and 0.20 mass%, and K₂O is between 0.02 and 3.14 mass%. The Fe₂O₃ content is highly variable, from 8.44 to 27.70 mass%. TiO₂ is between 1,14 and 3.98 mass%. Respect to the major elements, the most important of them are Si, Al and Fe. In addition, some samples show presence of Ca, probably because they include a part of enclosing material. In the matter of rare earth elements (RREE), they have been analysed but their concentration is lower than the XRF limits, showing less than the minimum concentration satisfactorily. In this case, it can be considered that the concentration of these elements are low enough to be considered as not interesting or suitable to be analysed with more detail.

According to the Fe₂O₃-Al₂O₃+TiO₂-SiO₂ ternary diagram (Bárdossy & Aleva, 1990) the San Joan de Mediona materials are clayey bauxites whereas those from Peramola plot also in

the bauxitic clay to the iron-rich bauxite (Figure 6). However, the composition of the materials analysed have high variability, having multiple types of material but a great part of them can be considered iron-rich bauxites and clayey bauxites. The samples can be group according to this chemical composition, obtaining sample families that will help for further discussions. At first sight, the groups formed agree with the origin of the sample and the location from where they were obtained (Figure 7).

Comparing with other bauxite locations (Reinhardt et al., 2018) it can be seen that part of the studied materials from the present work have similar chemical composition to other bauxitic materials around Catalonia (

Table 2). The most important difference is that the iron and aluminium concentrations in some samples are higher than the bauxitic materials of other points of Catalonia, having the highest concentrations some outcrops from Peramola area, especially the reddest samples such as PER 1 or PER-10V.

Table 1. Chemical composition, mass%, of major elements from Peramola and Sant Joan de Mediona.

Oxides	PER-1	PER-2B	PER-3	JM-1	JM-2
SiO ₂	9.51	48.00	30.50	24.00	23.43
Al ₂ O ₃	47.20	27.10	34.60	42.80	16.69
Fe ₂ O ₃	27.70	8.44	19.40	18.00	8.21
CaO	0.15	0.32	0.32	0.16	24.52
MgO	0.07	0.64	0.10	0.10	0.43
Na ₂ O	0.04	0.20	0.04	0.05	0.06
K ₂ O	0.02	1.99	0.10	0.02	0.06
TiO ₂	2.16	1.14	1.71	2.39	0.95
MnO	0.00	0.00	0.01	0.01	0.01
P ₂ O ₅	0.05	0.06	0.02	0.06	0.08
LOI	12.40	11.85	12.95	12.85	25.10
Total	99.30	99.74	99.75	100.44	99.54

Table 2. Chemical composition, mass%, major elements (Reinhardt et al., 2018).

Oxides	MM-1	MM-2	MM-3	MM-4	MI-0	MI-2	RU-1
SiO ₂	15.12	34.17	31.03	38.31	24.62	38.39	35.08
Al ₂ O ₃	48.98	29.55	26.73	32.57	39.43	34.18	29.45
Fe ₂ O ₃	19.57	22.71	28.66	13.33	19.95	12.56	14.97
CaO	0.08	0.12	0.11	0.13	0.14	0.20	2.53
MgO	0.03	0.04	0.04	0.08	0.07	0.05	0.45
Na ₂ O	0.02	0.02	0.02	0.03	0.03	0.04	0.06
K ₂ O	0.02	0.03	0.02	0.14	0.13	0.06	0.49
TiO ₂	2.34	1.59	1.43	1.96	2.21	1.74	1.86
MnO	0.01	0.04	0.04	0.08	0.07	0.05	0.45
P ₂ O ₅	0.09	0.05	0.04	0.10	0.14	0.10	0.07
LOI	12.77	11.55	10.67	12.78	12.36	12.96	14.77
Total	99.03	99.87	98.79	99.51	99.15	100.33	100.18

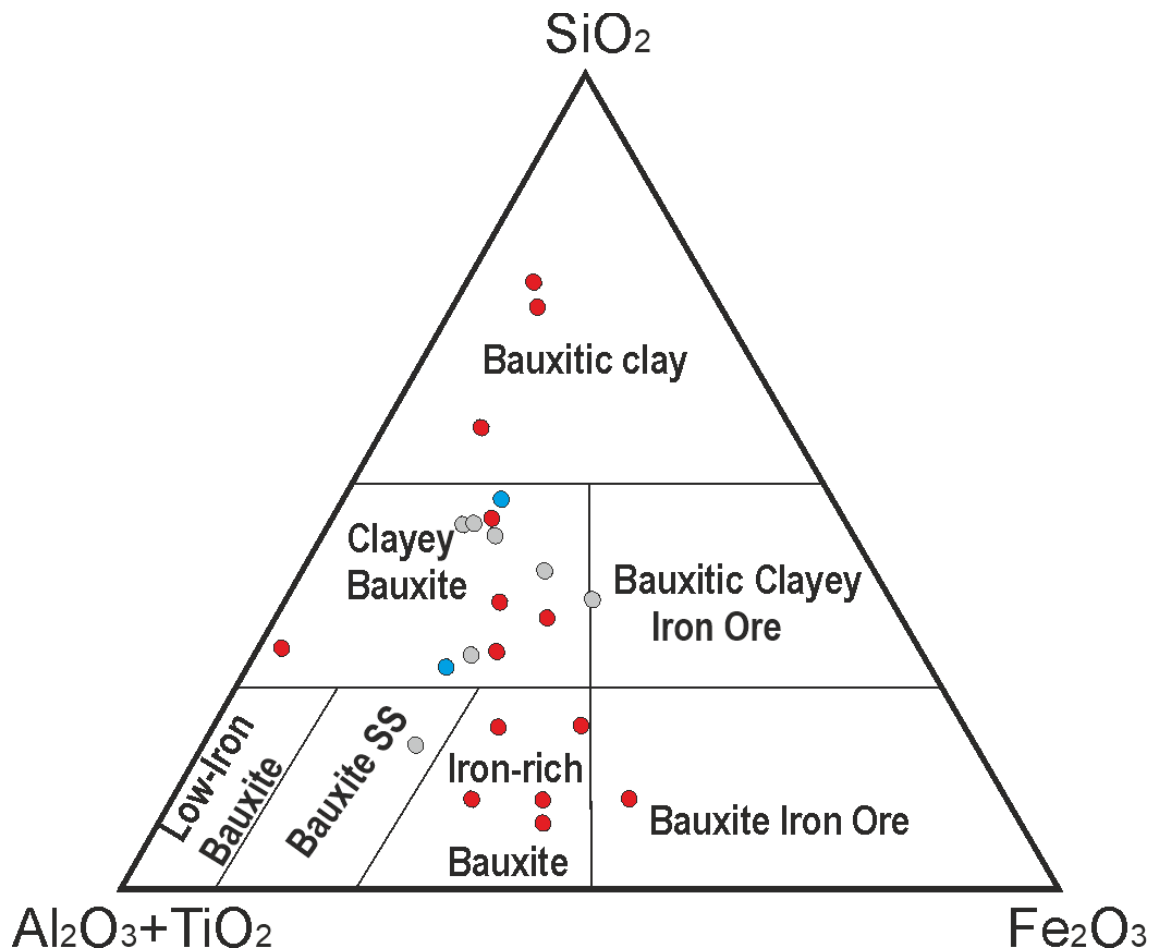


Figure 6. Ternary diagram. Red dots: Peramola samples, Blue dots: Sant Joan de Mediona Samples, Grey dots: Samples from (Reinhardt et al., 2018).

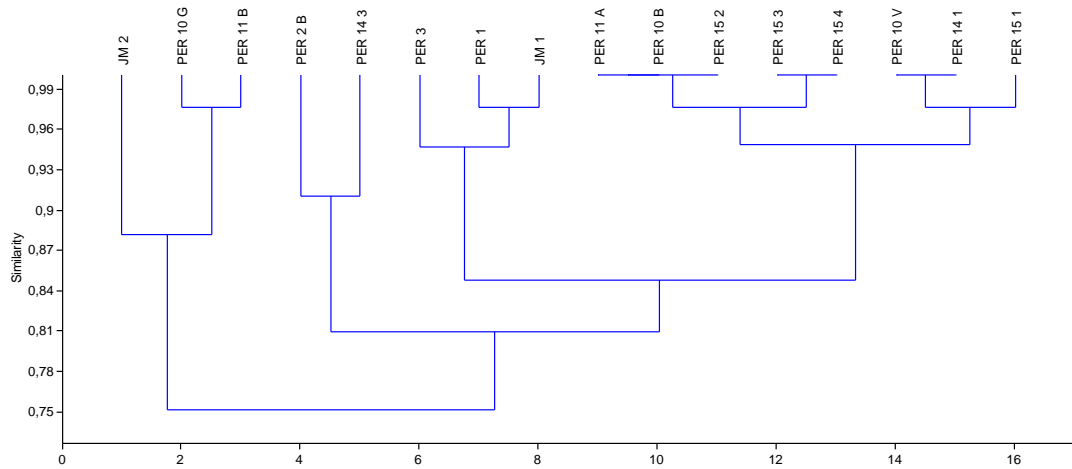


Figure 7. Families of samples according to chemical composition.

Mineralogical composition

The mineralogical composition of waste materials from the studied locations is presented in (Figure 8). In Peramola the mineralogy is quite variable. In general, kaolinite is the predominant mineral, accounting for up to 68 mass% of the deposit, except in one area where kaolinite accounts for 23 mass%, in which case boehmite is the major mineral, with 61 mass%. Hematite is found in the range of 4-22 mass%. Calcite is found in minor amounts, less than 1 mass% from absent to 25 mass%. Minor amounts of rutile and anatase are also present, generally around 1-3 mass%. However, these materials are found together with calcite-rich materials. In the case of Sant Joan de Mediona, kaolinite can reach up to 60 mass%, while boehmite is around 25 mass%. Another sample from San Joan de Mediona has presented up to 54 mass% of calcite, probably because the sample taken had contiguous material, being the main mineral calcite.

Also comparing with (Reinhardt et al., 2018), the mineralogical composition has more differences than the chemical composition. Peramola and Sant Joan de Mediona samples are less kaolinitic than the samples of bauxites presented on (Reinhardt et al., 2018), instead, boehmite concentrations are higher and hematite are more less the same, around 16 mass%. Compared to other bauxitic materials (Earnest et al., 2018; Rivas Mercury et al., 2010; Wang et al., 2015), the amount of aluminium minerals is higher in our materials. The concentration of iron oxides is lower than the red muds but these samples are more kaolinitic than them. Compared to kaolinitic materials (Alfonso et al., 2022; Garcia-Valles et al., 2015, 2020, 2022), more used for ceramic applications, our samples contain less kaolin compared to the most kaolin rich samples but more kaolin compared to the least rich samples. Also, Peramola and Sant Joan de Mediona materials have much less quartz than these others materials, including the lack feldspar presence.

Due to the presence of clay minerals, orientated aggregates have been made (Figure 9). Thanks to them only the presence of kaolinite could be detected on all samples analysed. In addition, in only one sample could detect another clay mineral, in this case illite in the sample PER-2B. Other clay minerals as chlorite or smectite could not be detected. The mineralogical results are suitable to the chemical composition obtained previously.

In the case of samples PER-2A and PER-2C, due to their difference with other samples and that their composition is far from the target compositions, they will not be considered.

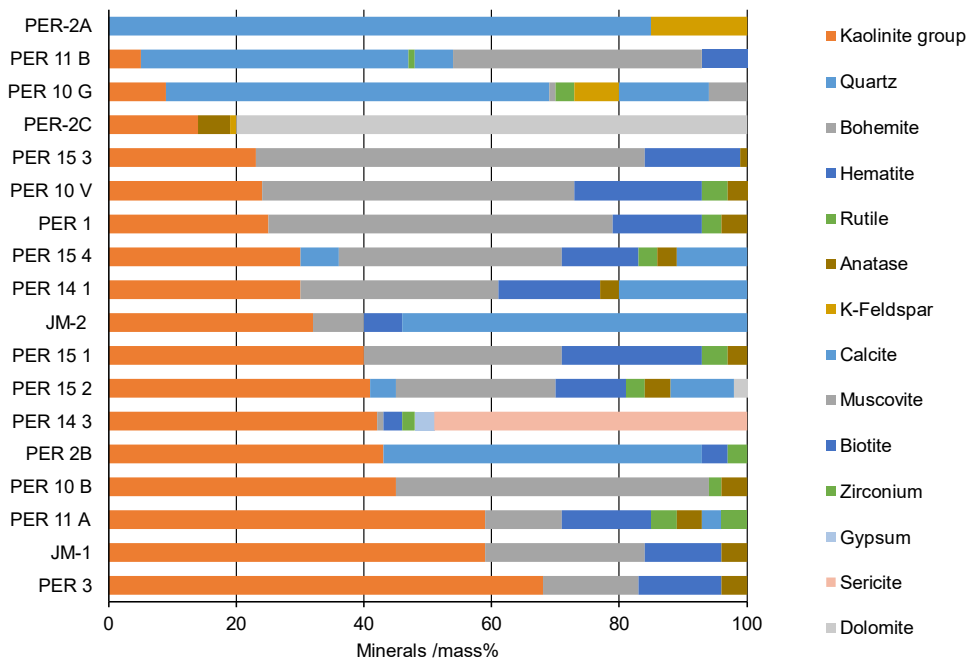


Figure 8. Mineralogical composition of Peramola and Sant Joan de Mediona samples. Arranged by kaolinite amount.

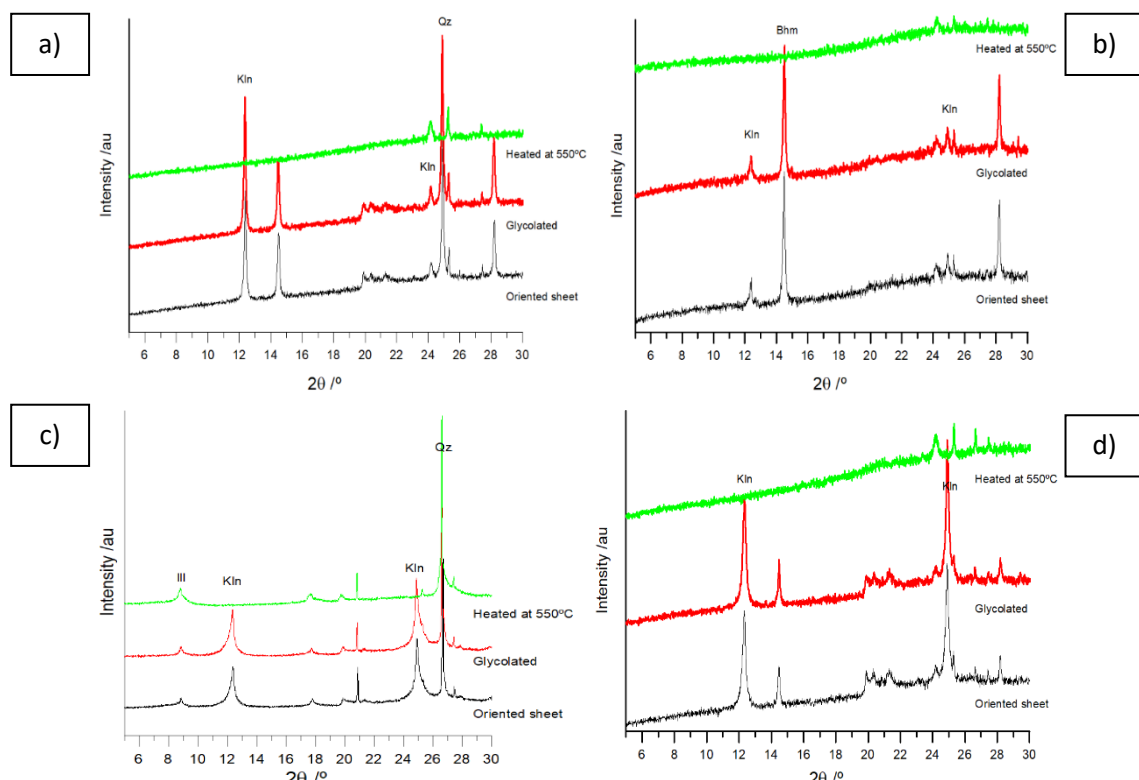


Figure 9. Plots of orientated aggregates. Mineralogy of representative samples from Peramola (PER) and Sant Joan de Mediona (JM): (Kln) Kaolinite, (Qz) Quarts, (Bhm) Boehmite, (III) illite. a) JM-1, b) PER-1, c) PER-2B, d) PER-3.

With the results obtained through XRD, in the samples that show presence of kaolinite has been calculated the Hinckley Index (HI) (Dill, 2016; Hinckley, 1965) to determine the crystallinity of kaolinite. Higher values represent better degree of crystallization, a value near 1 or above are considered crystallized meanwhile lower values like 0.5 implies low grade of crystallization of kaolin (Aparicio and Galán, 1999). The samples show different types of crystal qualities, from samples with an HI near 1 and some other samples with an HI of 0.5 (Table 3). The samples with lower crystallinity grades belong to areas where the materials have been more altered, meanwhile the values of 1 or higher coincide with less altered samples. The samples with lower values are the ones which are nearer to the contact material, for these samples, calcite. Nearly all the remaining samples have an HI near 1, symbolising the good crystallization of kaolin, however, there is an exception, PER-10V, showing 2.14, value that could be considered out of range because. For further discussions it will be considered as well crystalized. The results of crystallinity index for kaolinite are very similar to the results presented on (La Iglesia and Ordoñez, 1990) of other kaolin around bauxitic deposits of NE Spain.

Table 3. Results of Hinckley Index for JM and PER samples.

Sample	HI
JM-1	1.02
JM-2	0.52
PER-1	1.39
PER-2B	0.51
PER-3	0.96
PER 10 B	1.12
PER 10 V	2.14
PER 11 A	0.95
PER 14 1	1.06
PER 14 3	1.22
PER 15 1	1.28
PER 15 2	0.86
PER 15 3	0.97
PER 15 4	0.94

Through the observation of the samples with SEM, textures can be determined. Kaolinite occurs as regular lamellar hexagonal flakes crystals and in some point of the samples halloysite can be spotted al tubular crystals between 1 and 10 μm , being a minority (Figure 10). Similar textures were found from the kaolinitic clays of the Camarillas Formation (Bauluz et al., 2014). Kaolinite is the major mineral and halloysite is a in minor amounts. Due to similarities of kaolinite and halloysite in composition and the pattern in XRD, is difficult to differentiate them

through these analytical methods, however through SEM it is possible to differentiate the crystals of ich mineral (Garcia-Valles et al., 2015; Worasith et al., 2011).

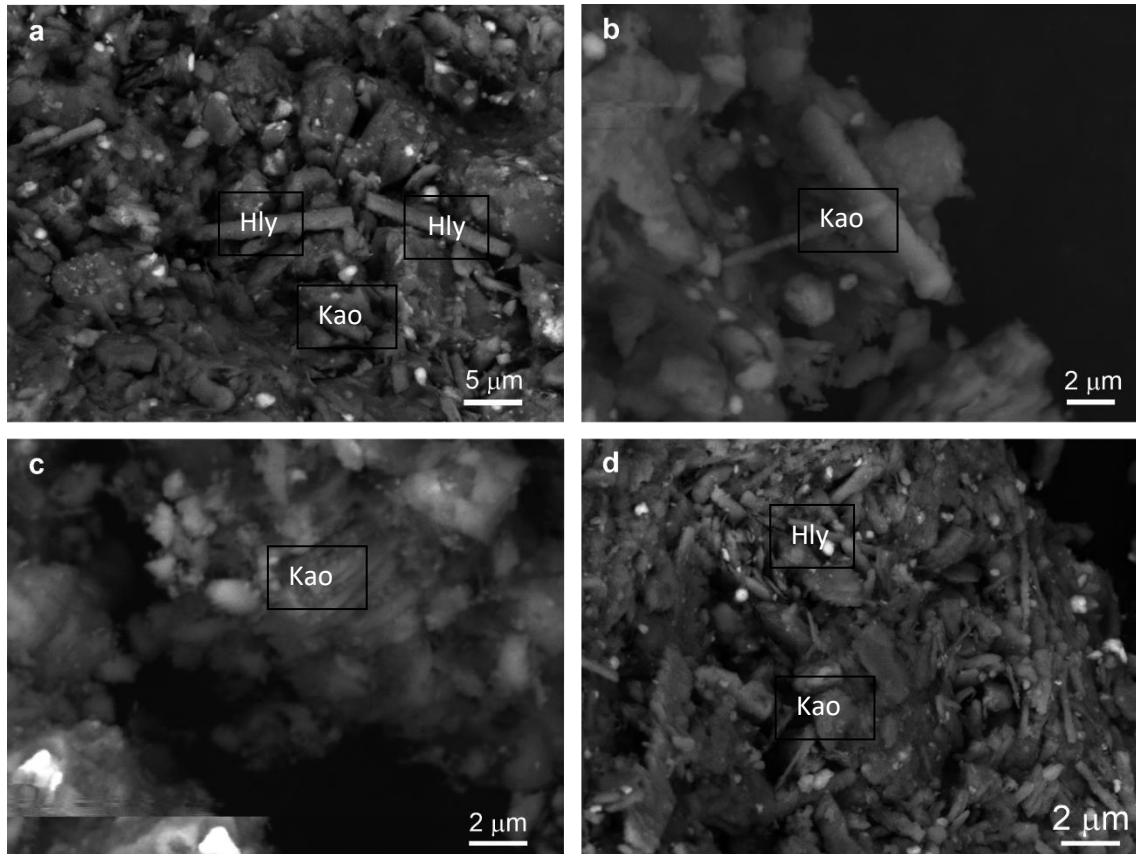


Figure 10. SEM images from representative samples from Peramola and Sant Joan de Mediona, showing presence of kaolinite (Kao) and halloysite (Hly).

FTIR spectra confirm the XRD results, being kaolinite and boehmite the most abundant minerals. Therefore, these are the minerals that will have the greatest influence on thermal and rheological behaviour of these materials. Bauxitic materials from Peramola and Sant Joan de Mediona present the typical bands of kaolinite (Alfonso et al., 2022; Ekosse, 2005; Farmer, 1968; Garcia-Valles et al., 2022; Guatame-Garcia and Buxton, 2018; Martinez Manent and Ballbe Llonch, 1985; Vaculíková et al., 2011), corresponding to structural bonds: $\text{SiO}_4 - \text{Al}_2\text{O}_3$ bonds (Si O-Al), octahedral aluminium bonds (Al-O and Al-OH) and tetrahedral silica bonds (Si-O). In the rank between 3800 and 3600 cm^{-1} the most characteristic absorption bands appear, which are related to Al-OH stretching. Also, appear coincidence in 1120 and 945 cm^{-1} regions corresponding to Si-O stretching. The same happens with boehmite as with kaolinite. However, only the Sant Joan de Mediona sample is fully represented, in other samples only part of the stretching are detected, this could even be related to the concentration of boehmite. The stretching band detected are Al-OH and H-O-H, corresponding to boehmite bonds (Figure 11) (Balde et al., 2021; Kloprogge et al., 2002).

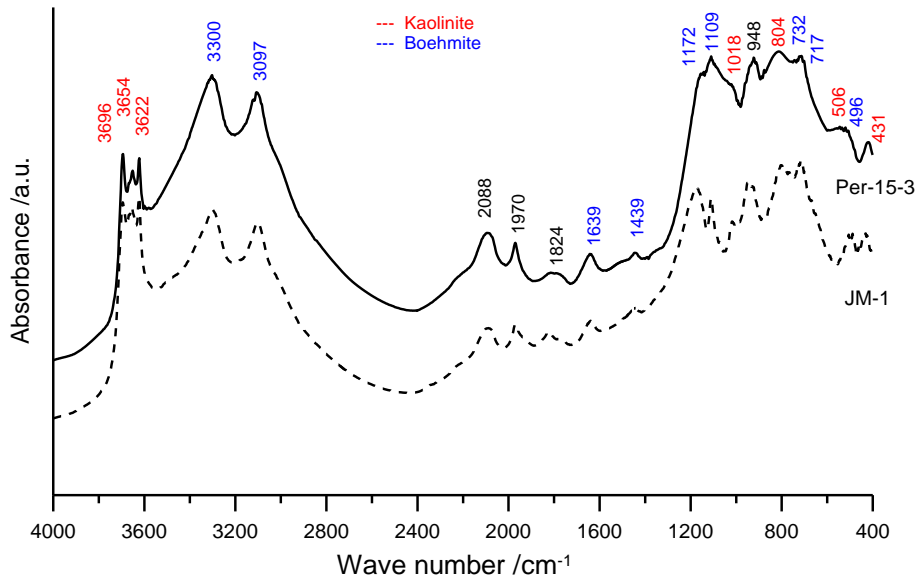


Figure 11. IR spectra from representative samples from Peramola and Sant Joan de Mediona.

Rheological properties

In this section, only plasticity will be showed. After dilatometric results, density results will be presented because the samples used to calculate the materials density are the materials tested previously in dilatometry test.

Plasticity

The plastic limit (PL), liquid limit (LL) and plasticity index (PI) are shown in Table 4 and the Casagrande plasticity chart in Figure 12.

Table 4. Table of plasticity indexes from Peramola and Sant Joan de Mediona Samples.

Sample	PL (%)	LL (%)	PI (%)
PER-1	20.22	26.35	6.14
PER-2B	26.45	50.26	23.81
PER-3	25.00	31.76	6.76
JM-2	26.42	32.18	5.76
PER-10V	20.87	23.70	2.83
PER-10B	30.13	30.27	0.14
PER-11A	25.29	27.51	2.22
PER-14-3	26.18	35.45	9.27
PER-15-1	21.79	22.09	0.30

The Atterberg limits showed by the main part of the samples have very similar limits. The values obtained are low, for plastic limit (PL= 20.22-30.13) and liquid limit (LL= 22.09- 50.26) (Day, 1999; Garcia-Valles et al., 2020). The plastic index is also low for the main part of the samples (PI= 0.14- 23.81). The plastic behaviour is different depending on their mineralogical composition. The plasticity index increases with kaolinite and other clay minerals contents; however, high crystallinity index of kaolinite implies lower plasticity (Bartolomé, 1997). As well as decrease with the quantity of oxides, hematite and boehmite growth. Nearly all the materials tested give very poor plasticity index, according to the amounts of different types of oxides, as boehmite and hematite.

PER-2B, PER 14-3 and JM-2 are medium plastic materials. Other samples are even less plastic.

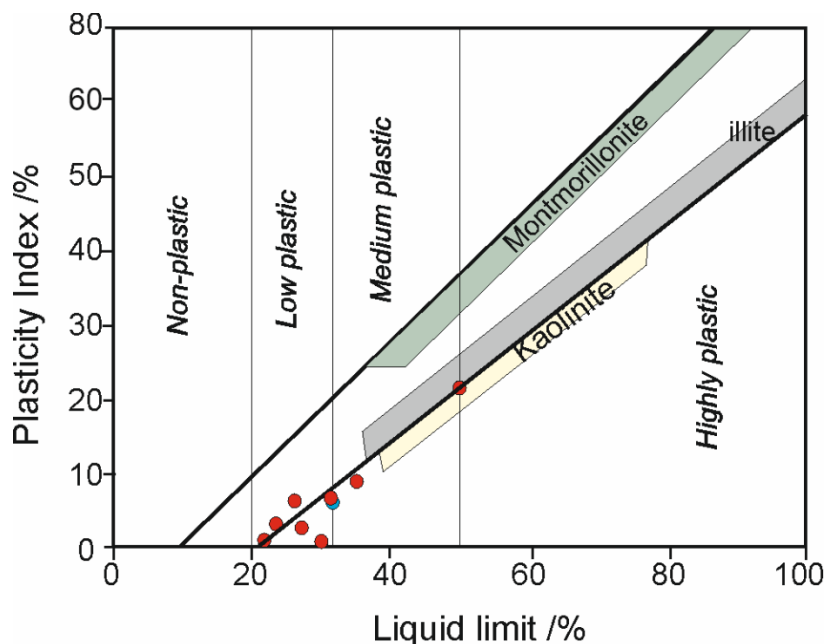


Figure 12. Casagrande plasticity plot (Casagrande, 1948). The bauxitic materials studied are low plastic, except for a few which are medium plastic.

Thermal properties

ATD-TG

The differential thermal analysis and thermogravimetric analysis (DTA-TG) curves of the bauxitic materials indicates the changes produced with the temperature (Table 5). Two endothermic peaks are observed in the DTA curves. The endothermic peak at 527-538 °C is produced by the dehydroxylation of boehemite to form γ -Al₂O₃ (Bokhimi et al., 2001; Filho et al., 2016). The endothermic at t 564-570 °C is produced by the dehydroxylation of kaolinite. An exothermic peak occurs at 950-978 °C due to the transformation of metakaolinite and γ -Al₂O₃

into mullite. The first derivate of DTA plot is useful to detect picks which can be hidden due to the lack of sufficient differentiation (Figure 13).

The mass loss at a temperature up to 110 °C is produced by the release of humidity, and it is about 1.34 mass%. The loss associated with the release of the hydroxyl groups is about 10.5 mass% (Figure 14) (Földvári, 2011; Ramachandran et al., 2002; Todor, 1976).

The results obtained through DTA-TG are according to the mineralogical results. The difference of the amount of kaolinite and boehmite can be seen with the highest pick, where if the 530 °C is the highest mean that boehmite is predominant and if the 560 °C pick is the highest means that kaolinite is predominant (Figure 15).

Table 5. Characteristic picks from DTA-TG from representative samples from Peramola and Sant Joan de Mediona.

Sample	Temperature / °C				Weight loss / %		
	endothermic		exothermic		adsorbed water <200°C	structural water 400-550°C	related to 2 endothermic
	1 boehmite	2 kaolinite	$\theta\text{-Al}_2\text{O}_3 \rightarrow \alpha\text{-Al}_2\text{O}_3$	mullite			
Per-1	538	568	----	978	0.48	5	5.5
Per-2B	----	547	950	1.89	4	4	
Per-3	530	568	952	972	1.49	6	5
JM-1	536	564	---	966	0.31	5.33	6
PER-10B	530	547	954	970	1.91	7.24	7.4

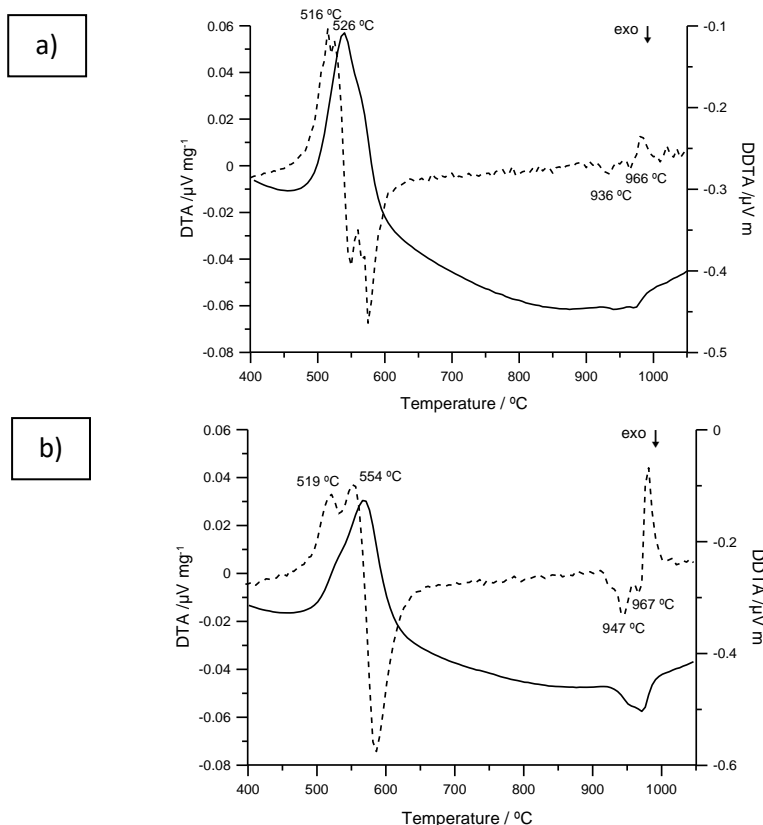


Figure 13. DTA and first derivate of DTA plot. a) PER-1, b) PER-3.

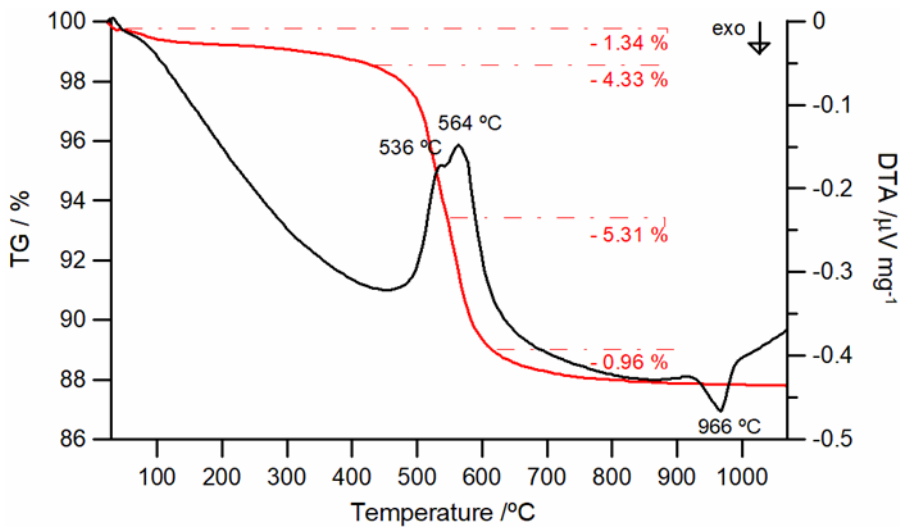


Figure 14. DTA-TG from Sant Joan de Mediona sample (JM-1).

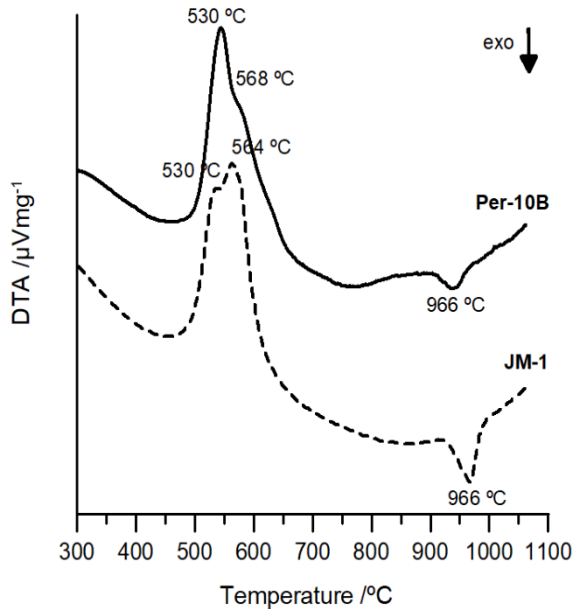


Figure 15. Comparison between boehmite rich sample (PER-10B) and kaolinite rich sample (JM-1) DTA plots.

Dilatometry

The dilatometric curves from the bauxitic clays show that during firing three main stages of shrinkage are produced (Figure 16) (Garcia-Valles et al., 2015, 2020; Gippini, 1979). The first stage is produced between 515-535 °C a contraction is due to release of the structural hydroxyl group of boehmite with the formation of γ -alumina (2):



Later, at 950 °C spinel-like structure lead to a shrinkage and finally, at 1010 °C a new shrinkage is caused by sintering and densification processes with the formation of $\alpha\text{-Al}_2\text{O}_3$.

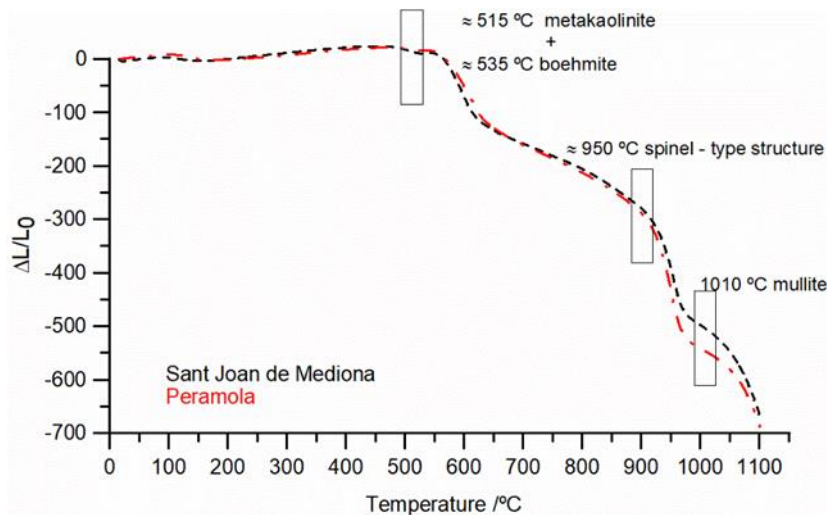
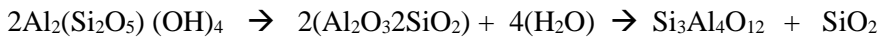


Figure 16. Dilatometry from representative samples from Peramola and Sant Joan de Mediona.

Samples PER-3 and JM-1 show very similar patterns, PER-1 show as well shrinkage at similar temperatures but the deformation is lower than the other samples. They show their main shrinkage near 600 °C, 1050 °C and 1200 °C, associated to boehmite transformations, in addition can be seen shrinkage near 890 and 1010 °C due to transformations of kaolinite. The most different sample is PER-2B, only showing the transformations of kaolinite. The shrinkage that could be identified are (Figure 17):

- Related to Kaolinite

Shrinkage (890 °C) produced by the collapse of metakaolinite into a spinel-like structure.



Metakaolinite Kaolinite Spinel-like structure

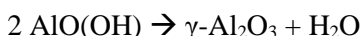
Shrinkage (1010 °C). at the beginning of the sintering, when the spinel-like phase is transformed to mullite and amorphous SiO₂.



Metakaolinite Mullite

- Related to Boehmite

a) Shrinkage (600 °C - 1000 °C) due to departure of structural hydroxil group of boehmite with the formation of gamma-alumina:



b) Shrinkage (1050 °C) due to necking formation between particles.

c) Shrinkage (1200 °C) due to sintering and densification processes. Formation of α-Al₂O₃

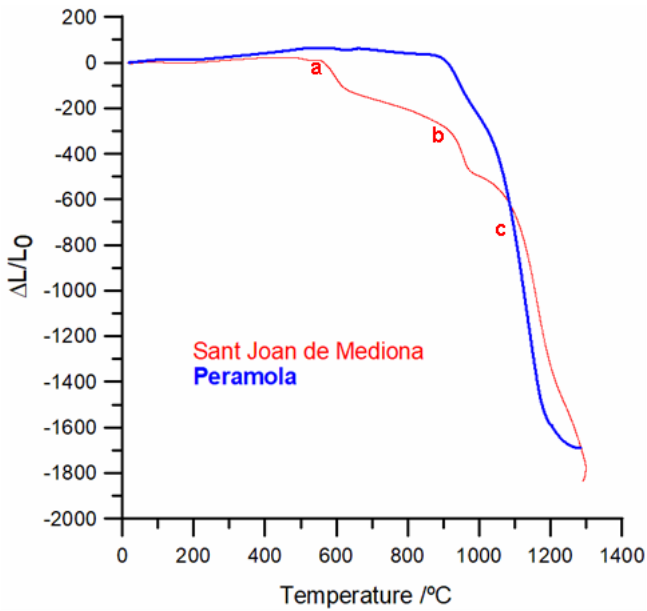


Figure 17. Dilatometry from representative samples from Peramola and Sant Joan de Mediona.

Dilatometric coefficient

Samples with higher amounts of boehmite show less deformation, being represented through the thermal dilatometric coefficient (Table 6).

Table 6. Dilatometric coefficient from dilatometry tested samples.

Sample	Dilatometric Coefficient ($^{\circ}\text{C}^{-1}$)
JM-1	$5,8 \cdot 10^{-6}$
PER-1	$3,8 \cdot 10^{-6}$
PER-2B	$7,3 \cdot 10^{-6}$
PER-3	$4,7 \cdot 10^{-6}$

Hot stage microscopy (HSM) or optical dilatometry

All test arrived to 1450 °C, with a heating ratio of 5 °C/min. Only one sample melted and showed all the different stages, from the first shrinkage 763°C, softening 1320 °C, the formation of ball shape 1328 °C, half ball shape 1366 °C and flow 1378 °C (Figure 18). This sample is the one which had more amount of calcite, being Ca a flux making easier the material melting. All the other samples analysed only presented some notable shrinkage from around 900 °C and above, without reaching the softening point at temperatures of 1450 °C (Figure 19). This fact can be attributed to the main presence of kaolinite well crystallized, Hinckley Index near or above 1, and high amounts of boehmite (Rivas Mercury et al., 2010).

Results obtained through HSM show similar results to the results obtained from dilatometry, having shrinkage at nearby temperatures and similar shrinkage. Figure 20 shows the two plots for comparison. Their units are different, however they show qualitatively the variation of the linear shrinkage data obtained with HSM and dilatometry.

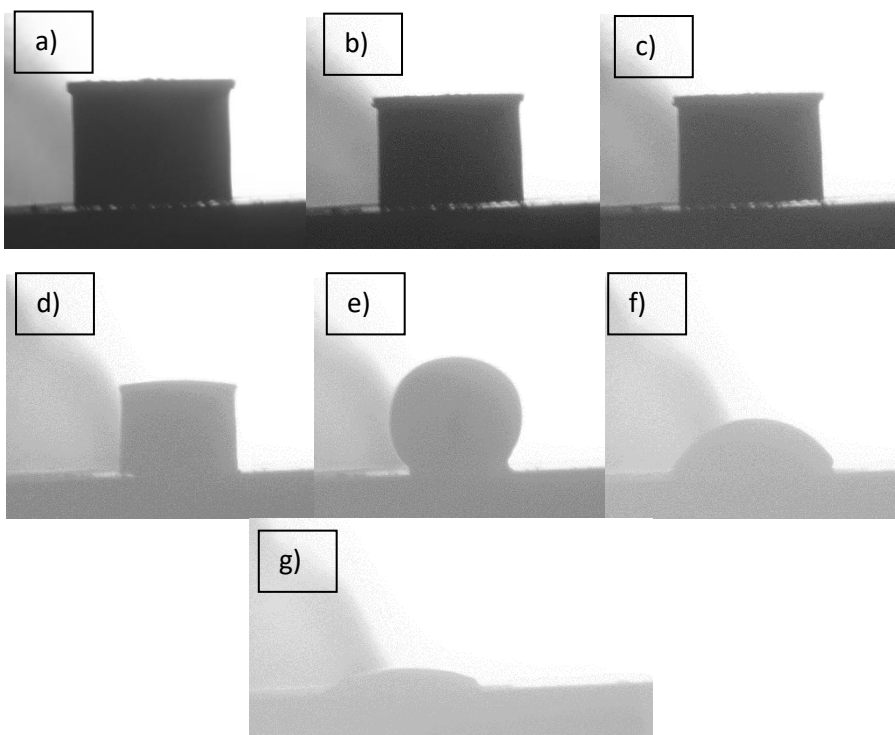


Figure 18. HSM images from JM-2. a) 763°C , First shrinkage; b) 987 °C; Shrinkage stop; c) 1206°C, Shrinkage; d) 1320°C, Softening; e) 1328 °C, Sphere; f) 1366°C, Semiesphere; g) 1378 °C, Flow.

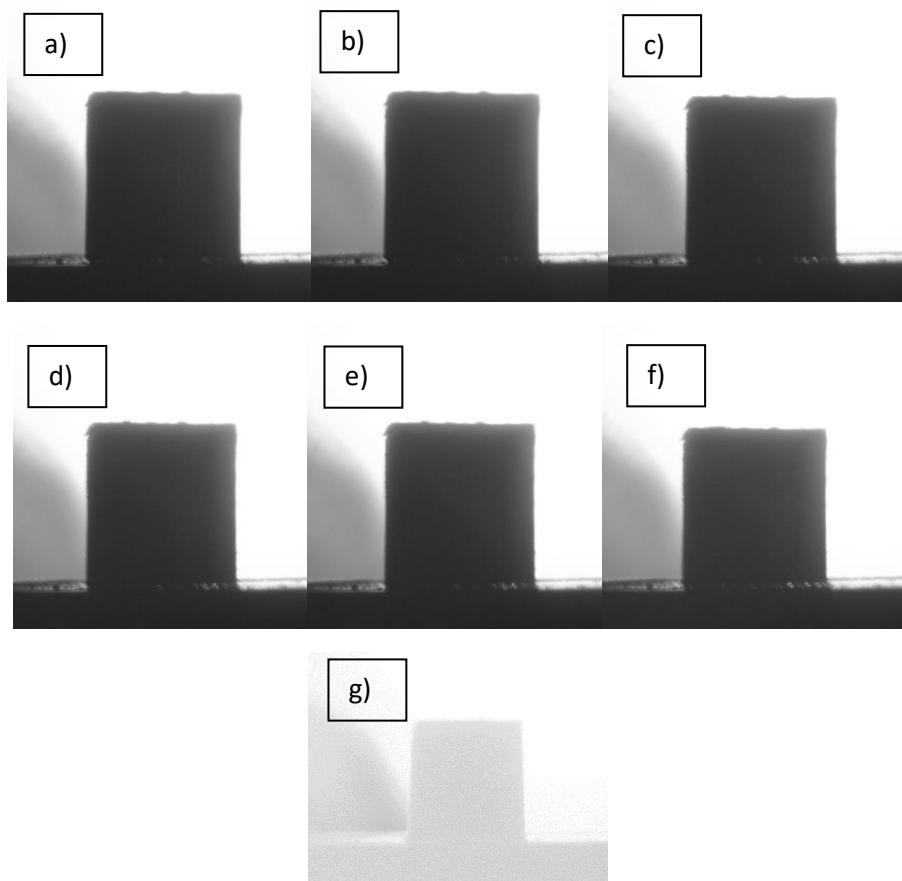


Figure 19. HSM images from PER-3. a) 246°C, Beginning; b) 297°C, First shrinkage; c) 700 °C, Shrinkage; d) 950 °C, Shrinkage; e) 1000 °C, Stop shrinkage; f) 1050 °C, Shrinkage restart; g) 1450 °C, End.

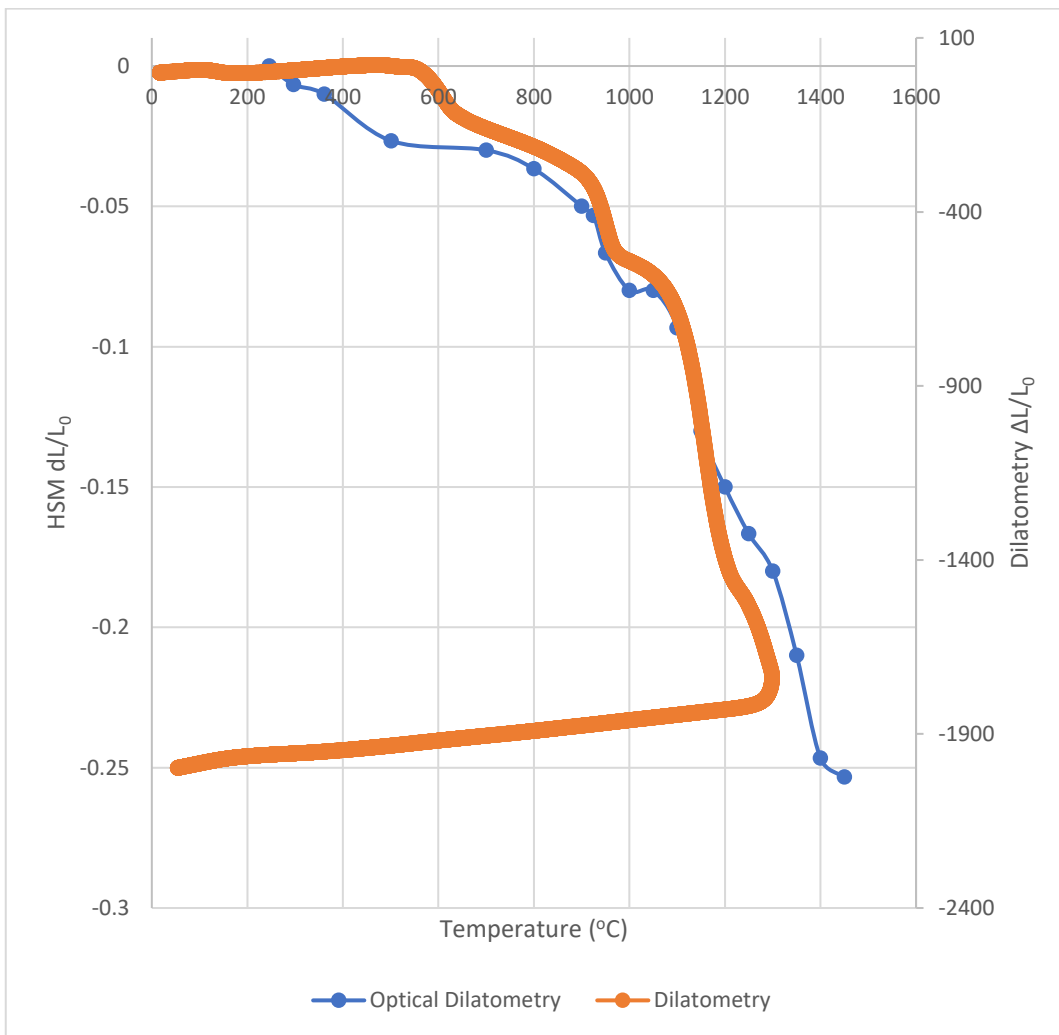


Figure 20. Comparison between shrinkage detected through HSM (optical dilatometry) and dilatometry. PER-3 sample.

Density

The densities obtained depends mainly on the mineralogy of the materials, being the densest the richest in boehmite. These correspond to the materials obtained inside the Peramola mine, samples from the waste material have similar density, 2.9 g/cm^3 (Table 7). The materials treated at 1300°C . Compared to other samples bauxitic samples, the Peramola and Sant Joan de Mediona samples are heavier than other materials, such as the 2.65 g/cm^3 of (Rivas Mercury et al., 2010) red mud. Except for PER-1 sample and PER-2B, the other samples are near the density, the little difference, apart from mineralogical composition, could be due to the thermal treatment were the samples have been compacted.

Table 7. Density of the Bauxitic materials from Peramola and Sant Joan de Mediona.

Sample	Density, g/cm ³
PER-1	3.26
PER-2B	2.45
PER-3	2.88
JM-1	2.89

Technological properties

Gresification curves

To analyse the behaviour of the samples through different temperatures and determine the viability of these material as raw material for ceramics. Gresification curves are the representation of linear shrinkage and water absorption respect the temperature in the same plot (Baccour et al., 2009; Garcia-Valles et al., 2022). This representation helps to predict the optimal firing temperature of the raw material and allow to determine the balance between hardness of the ceramic and the minimum porosity achieved, minimizing the processing costs.

The analysis has been made until 1300 °C. with an increase of 2°C/minute and a final dwell of 1 hour. There were prepared 9 tiles for each sample analysed and each one has been tested until a certain degree is temperature (

Table 8). The results obtained of firing shrinkage and the water absorption are showed through Figure 21Figure 21. Gresification curves of bauxitic materials from Peramola and Sant Joan de Mediona. a) PER-2B, b) JM-2, c) PER-3.. The relationship between firing shrinkage and water absorption has an inverse correlation, whereas linear shrinkage increase, water absorption decrease. Samples show a progressive shrinkage, (PER-3), In the case of JM-2, from around 1150 °C shrinkage ratio increase. For PER-2B sample there is a first shrinkage until 1175 °C and from this point start an expansion stage. At the same time, water absorption does the opposite, for all samples exists a decrease of water absorbance while the temperature increase, except for one sample. PER-3 show a progressive decrease of water absorption from the starting point until the end. For JM-2 sample, as it happens with the lineal shrinkage, water absorption ratio also decreases faster after around 1150 °C (Cargnini et al., 2015). Finally, PER-2B sample, at 1150 °C achieve the minimum water absorbance until around 1200 °C. This minimum is near the 0% of water absorption, implying that a ceramic material fired to this range of temperature would be a waterproof layer.

Thanks to these graphics, sintering temperatures can be determined searching for the intersection between the firing shrinkage and the water absorption plots. The optimal sintering temperatures would be near 970 °C for Peramola samples and near 1190 °C for Sant Joan de

Mediona samples. The decrease of water absorption can be also seen through SEM images where intergranular porosity decrease at higher temperatures (Figure 22). The closing porosity is due to the anisotropic expansion of clays during heating (Çelik, 2017; Darbari et al., 2017; Garcia-Valles et al., 2022). The loss of intergranular porosity is proportional to the firing shrinkage, which also has similarity to the dilatometric curves observed previously. The samples show a uniform structure in a macroscopic observation. With SEM observation, the image of 1250 °C shows the samples sintered, meanwhile the previous images were not sintered yet. The traces of hematite can be spotted in all temperatures (Figure 23), but the amount of it decrease when temperature increase. Also, mullite can be seen in the samples, from near 1150 °C (Montoya et al., 2010)

In mineralogy affairs, changes through temperature increase have been shown. The samples have an appreciable amount of amorphous phase, meaning that from XRD results it is not possible to obtain accurate quantification results. Also, the mineralogical characterization is more difficult because of the amorphous phase, hiding and distorting characteristic picks of other minerals. For the sample with calcite, JM-2, from 900 °C appear gehlenite, anorthite and some traces of hematite. At 1200 °C appear hedenbergite, and hematite cannot be spotted. For Peramola sample, PER-2B, at 900 °C can be found quartz, sillimanite and traces of hematite and rutile. At 1100 °C and above, mullite can be added in the list. For this material, the sample tested at 900 °C is when metakaolinite has to start converting into mullite (Montoya et al., 2010), but they cannot be detected because of the amorphous phase. In each case exists minerals, such as spinel group minerals or cristobalite, which should appear according to the mineralogical transformations described at dilatometry, however, most probably these materials can be found inside the amorphous phase, not being able to detect them through XRD analysis. The only sample with quartz is PER-2B, so this sample should show presence of cristobalite (Lyu et al., 2021; H. Schneider et al., 1986).

Sample PER-1 has been also tested but the tiles prepared started to separate with the first thermal treatment, most probably due to lack of plasticity and cohesion.

Table 8. Table determining Temperature for each tile for gresification curves.

Temperature (°C)	Tile number
900	1
1000	2
1050	3
1100	4
1150	5
1175	6
1200	7
1250	8
1300	9

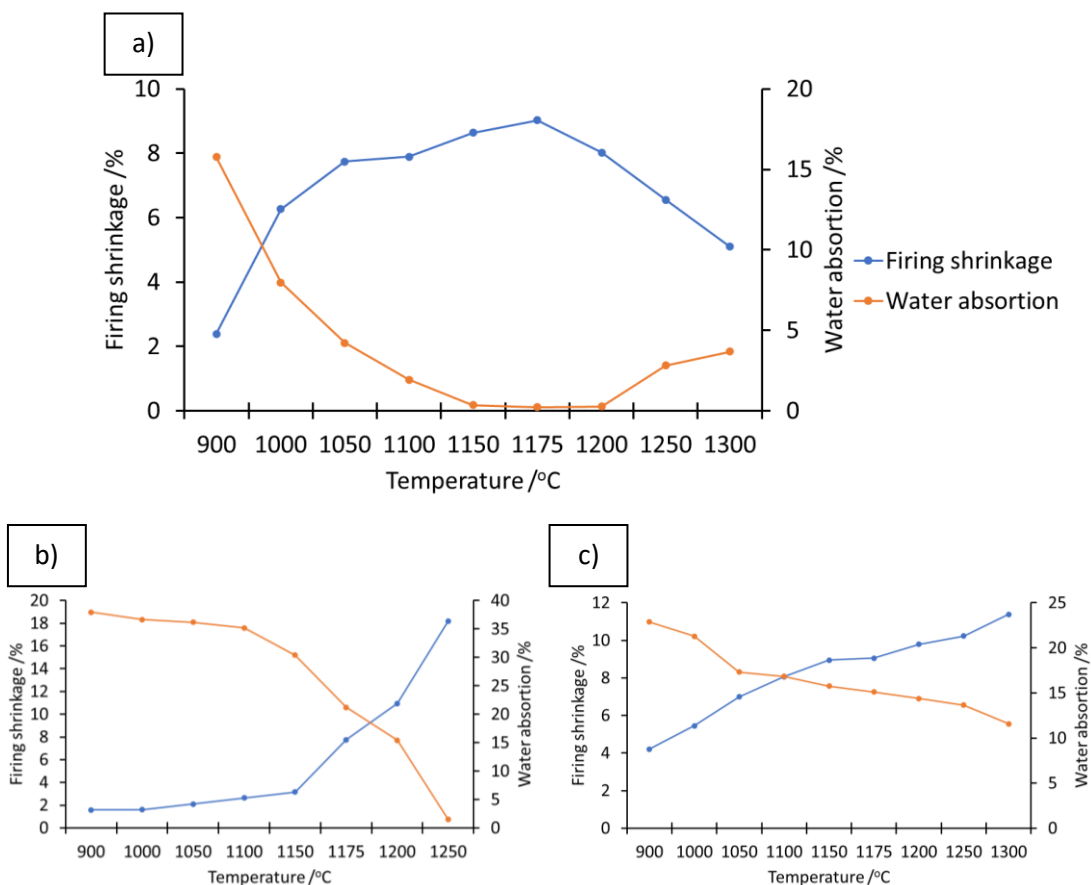


Figure 21. Gresification curves of bauxitic materials from Peramola and Sant Joan de Mediona. a) PER-2B, b) JM-2, c) PER-3.

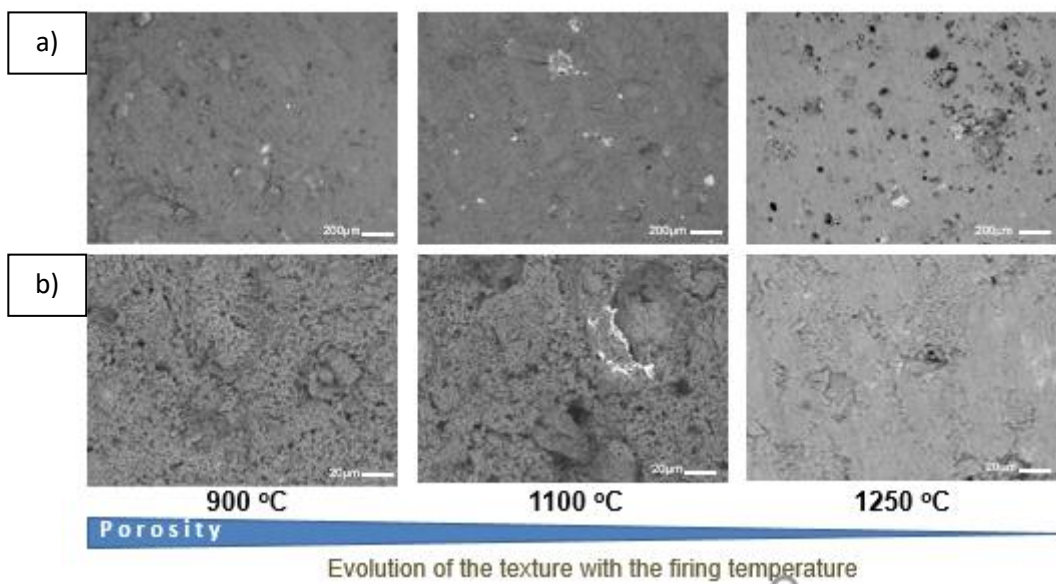


Figure 22. Texture evolution through different firing temperatures. a) PER-2B, b) JM-2.

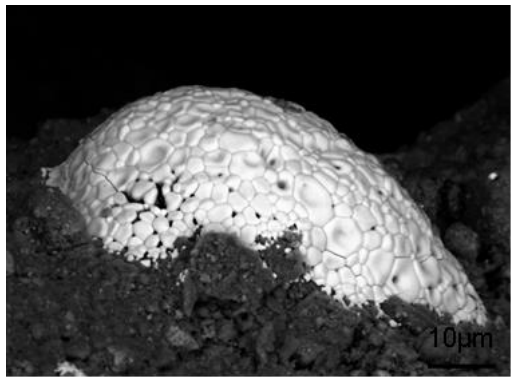


Figure 23. Hematite formation in a fired sample from Peramola.

Colorimetry

Due to the firing temperatures and the transformation of minerals, tile colour change. The colour of the tiles principally depends on Fe_2O_3 and TiO_2 content, but mineralogy also have influence. In all cases the tiles got darker with the temperature increase, caused because of the change of mineralogical composition. Colour can be described through parameters L^* , a^* and b^* (Barba et al., 1997):

- $L^*=100$ is white and $L^*=0$ is black
- $a^*>0$ is red and $a^*<0$ is green
- $b^*>0$ is yellow and $b^*<0$ is blue

At first stages colour is conditioned by the amount of hematite that can be found inside. In Peramola sample the increase of a^* chromatic coordinate after 1200 °C due to the destruction of illite structure, where Fe^{3+} is liberated, forming new phases or crystalize into hematite increasing the reddish colour (Figure 24) (Bouzidi et al., 2014; De Bonis et al., 2017). The decrease of a^* coordinate can be associated to the formation mullite, which can absorb part of hematite leading to whitter colours. In both materials, Peramola and Sant Joan de Mediona materials, L^* coordinate decrease due to formation of iron and/or titanium oxides. In the case of Sant Joan de Mediona sample, the results coincide with the typical carbonated clay. At first instance show a reddish colour due to the presence of hematite, later the calcite reacts with other silicates and alumina, forming calcium aluminosilicates, such as gehlenite and anorthite, increasing the L^* and b^* coordinate, giving a whiter colour to the sample until near 1150°C, after this temperature, amorphous phase increase and the L^* and b^* coordinate decrease (Figure 25).

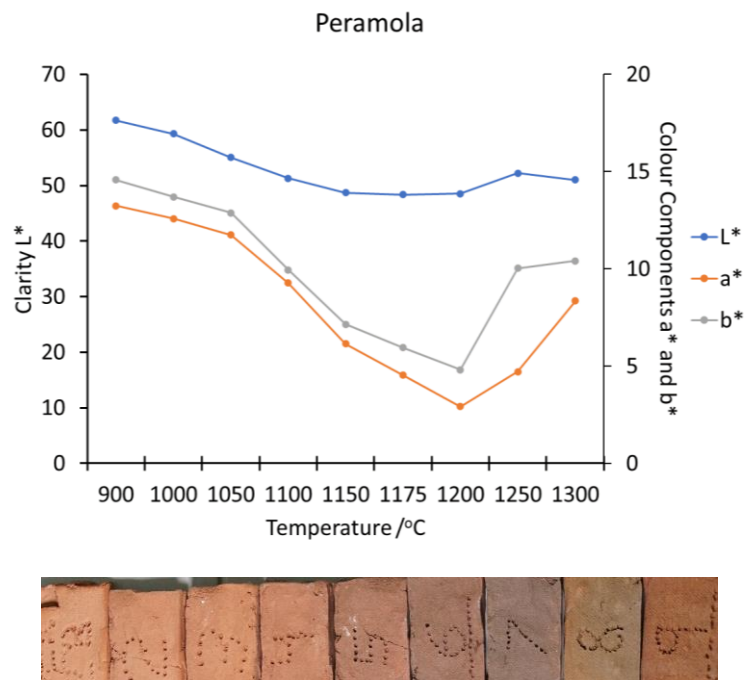


Figure 24. Chromatic coordinates of fired samples from Peramola.

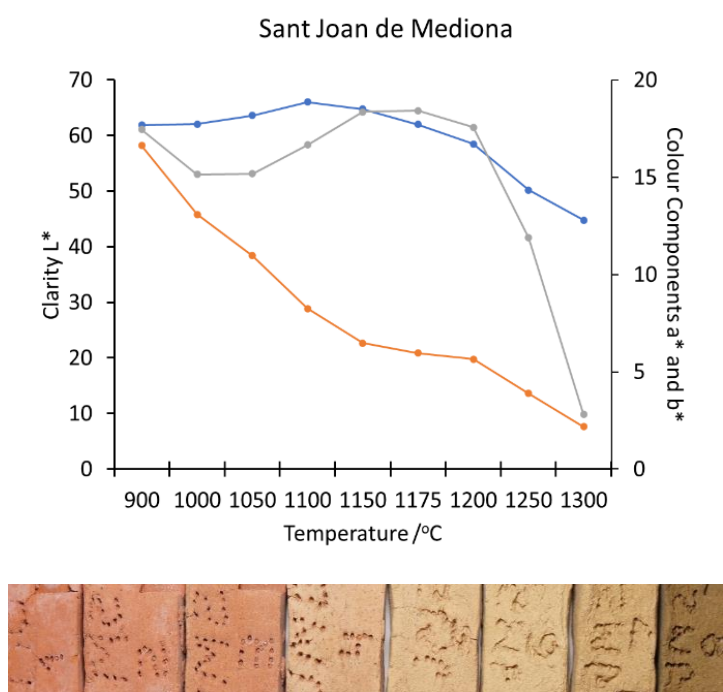


Figure 25. Chromatic coordinates of fired samples from Sant Joan de Mediona.

Conclusions

Materials from bauxite deposits, dumps and tailings of Peramola and Sant Joan de Mediona could be a potential resource of raw materials for the ceramics industry or could be a potential raw material for geopolymers or cementing materials. They show appreciable amount of kaolinite and boehmite, mixed with lower quantities of hematite, and sometimes mixed at some points with calcite, being similar to other bauxites from the NE of Spain, Catalonia. Due to this mineralogy, their density is a little higher than other material such as kaolinic materials, crystallinity index of kaolinite are high and their plasticity is low, being hard to work with them. This samples show the typical deformations which appear with presence of kaolinite and boehmite and having the melting point over 1450 °C, except for the samples that include calcite. Finally, the sintering temperatures of Peramola bauxites is 970 °C and for Sant Joan de Mediona bauxites is 1190 °C.

The materials studied cannot be used directly to make ceramics and they should be mixed with additional raw materials due to their low phyllosilicates content, lack of plasticity and high working temperatures. Another possible application is the production of geopolymers cementing materials. The composition of these bauxitic materials is similar to raw materials for cementing materials production. To know if they are suitable for this application, it is necessary to conduct additional experiments which will be carried out on further investigations. Even though, if there could be a possible application, the industrial usage would be difficult because of the lack of enough material for a sustained production. Also, there is the problem of homogeneity of the composition all along the dump, that combined with the lack of material makes it unlikely to be profitable. However, this work could be a starting point for characterization of bauxitic materials and study their viability for industrial use.

References

- Abbas, R., Khereby, M. A., Ghorab, H. Y., & Elkhoshkhany, N. (2020). Preparation of geopolymers concrete using Egyptian kaolin clay and the study of its environmental effects and economic cost. *Clean Technologies and Environmental Policy*, 22(3), 669–687. <https://doi.org/10.1007/s10098-020-01811-4>
- AENOR. (1976). *UNE 7-377-75 Determinación del Límite Líquido de un Suelo por el Método de la Cuchara*.
- AENOR. (1993). *UNE 103-104-93 Determinación del Limite Plástico de un Suelo*.
- AENOR. (2018). *UNE-EN ISO 10545-3 Determinación de la absorción de agua, de la porosidad abierta, de la densidad relativa aparente, y de la densidad aparente*.
- Alfonso, P., Penedo, L. A., García-Valles, M., Martínez, S., Martínez, A., & Trujillo, J. E. (2022). Thermal behaviour of kaolinitic raw materials from San José (Oruro, Bolivia). *Journal of Thermal Analysis and Calorimetry*, 147(9), 5413–5421. <https://doi.org/10.1007/s10973-022-11245-3>
- Aparicio, P., & Galán, E. (1999). Mineralogical interference on kaolinite crystallinity index measurements. *Clays and Clay Minerals*, 47(1), 12–27. <https://doi.org/10.1346/CCMN.1999.0470102>
- Assi, L., Carter, K., Deaver, E. (Eddie), Anay, R., & Ziehl, P. (2018). Sustainable concrete: Building a greener future. *Journal of Cleaner Production*, 198, 1641–1651. <https://doi.org/10.1016/j.jclepro.2018.07.123>
- Baccour, H., Medhioub, M., Jamoussi, F., & Mhiri, T. (2009). Influence of firing temperature on the ceramic properties of Triassic clays from Tunisia. *Journal of Materials Processing Technology*, 209(6), 2812–2817. <https://doi.org/10.1016/j.jmatprot.2008.06.055>
- Baki, V. A., Ke, X., Heath, A., Calabria-Holley, J., Terzi, C., & Sirin, M. (2022). The impact of mechanochemical activation on the physicochemical properties and pozzolanic reactivity of kaolinite, muscovite and montmorillonite. *Cement and Concrete Research*, 162. <https://doi.org/10.1016/j.cemconres.2022.106962>
- Balde, M. Y., Djangang, C. N., Diallo, R. B., Blanchart, P., & Njopwouo, D. (2021). Physicochemical Characterisation for Potential Uses as Industrial Mineral of Bauxite from Débélé, Guinea. *Journal of Materials Science and Chemical Engineering*, 09(03), 9–22. <https://doi.org/10.4236/msce.2021.93002>
- Barba, A., Beltrán, V., Felíu, C., García, F., Sánchez, E., & Sanz, V. (1997). *Materias primas para la fabricación de soportes de baldosas cerámicas*. Instituto de Tecnología Cerámica.
- Bárdossy, G., & Aleva, G. J. J. (1990). *Lateritic bauxites: developments in economic geology*. Elsevier Scientific Publication.
- Bartolomé, J. (1997). El Caolín: composición, estructura, génesis y aplicaciones. *Boletín de La Sociedad Española de Cerámica y Vidrio*, 36(1), 7–19.
- Bauluz, B., Yuste, A., Mayayo, M. J., & Canudo, J. I. (2014). Early kaolinization of detrital Weald facies in the Galve Sub-basin (Central Iberian Chain, north-east Spain) and its relationship

- to palaeoclimate. *Cretaceous Research*, 50, 214–227. <https://doi.org/10.1016/j.cretres.2014.03.014>
- Benhelal, E., Shamsaei, E., & Rashid, M. I. (2021). Challenges against CO₂ abatement strategies in cement industry: A review. In *Journal of Environmental Sciences (China)* (Vol. 104, pp. 84–101). Chinese Academy of Sciences. <https://doi.org/10.1016/j.jes.2020.11.020>
- Bokhimi, X., Toledo-Antonio, J. A., Guzmán-Castillo, M. L., Mar-Mar, B., Hernández-Beltrán, F., & Navarrete, J. (2001). Dependence of boehmite thermal evolution on its atom bond lengths and crystallite size. *Journal of Solid State Chemistry*, 161(2), 319–326. <https://doi.org/10.1006/jssc.2001.9320>
- Bouzidi, N., Siham, A., Concha-Lozano, N., Gaudon, P., Janin, G., Mahtout, L., & Merabet, D. (2014). Effect of chemico-mineralogical composition on color of natural and calcined kaolins. *Color Research and Application*, 39(5), 499–505. <https://doi.org/10.1002/col.21813>
- Burbank, D. W., Verges, J., Munoz, J. A., & Bentham, P. (1992). Coeval hindward- and forward-imbricating thrusting in the south-central Pyrenees, Spain: timing and rates of shortening and deposition. *Geological Society of America Bulletin*, 104(1), 3–17. [https://doi.org/10.1130/0016-7606\(1992\)104<0003:CHAFIT>2.3.CO;2](https://doi.org/10.1130/0016-7606(1992)104<0003:CHAFIT>2.3.CO;2)
- Cargnin, M., De Souza, S. M. A. G. U., De Souza, A. A. U., & De Noni, A. (2015). Modeling and simulation of the effect of the firing curve on the linear shrinkage of ceramic materials: Laboratory scale and industrial scale. *Brazilian Journal of Chemical Engineering*, 32(2), 433–443. <https://doi.org/10.1590/0104-6632.20150322s00002876>
- Çelik, H. (2017). Technological Characterization and Comparison of Two Ceramic Clays Used for Manufacturing of Traditional Ceramic Products in TurkeyTürkiye ’ De GelenekselSeramikÜrünlerinİmalatında Kullanılan. *Mining*, 56(4), 137–147.
- Closas i Miralles, J. (1949). *Els nous jaciments de Bauxita*.
- Closas y Miralles, J. (1954). Las bauxitas NE España. *DIX Congr. Geol. International*, 199–223.
- Darbari, Z., Jaradat, K. A., & Abdelaziz, S. L. (2017). Heating–freezing effects on the pore size distribution of a kaolinite clay. *Environmental Earth Sciences*, 76(20). <https://doi.org/10.1007/s12665-017-7069-8>
- Day, R. W. (1999). *Geotechnical and foundation engineering: design and construction*. McGraw-Hill.
- De Bonis, A., Cultrone, G., Grifa, C., Langella, A., Leone, A. P., Mercurio, M., & Morra, V. (2017). Different shades of red: The complexity of mineralogical and physico-chemical factors influencing the colour of ceramics. *Ceramics International*, 43(11), 8065–8074. <https://doi.org/10.1016/j.ceramint.2017.03.127>
- de Brito, J., & Kurda, R. (2021). The past and future of sustainable concrete: A critical review and new strategies on cement-based materials. In *Journal of Cleaner Production* (Vol. 281). Elsevier Ltd. <https://doi.org/10.1016/j.jclepro.2020.123558>
- Di Mare, M., Nattrott Monteiro, V., Brial, V., Ouellet-Plamondon, C. M., Fortin, S., Tsesmelis, K., Montini, M., & Rosani, D. (2021). A calculator for valorizing bauxite residue in the cement industry. *Cleaner Materials*, 1. <https://doi.org/10.1016/j.clema.2021.100009>

- Dill, H. G. (2016). Kaolin: Soil, rock and ore. From the mineral to the magmatic, sedimentary and metamorphic environments. *Earth-Science Reviews*, 161, 16–129. <https://doi.org/10.1016/j.earscirev.2016.07.003>
- Du, H., & Pang, S. D. (2020). High-performance concrete incorporating calcined kaolin clay and limestone as cement substitute. *Construction and Building Materials*, 264. <https://doi.org/10.1016/j.conbuildmat.2020.120152>
- Earnest, C. M., Gann, K., & Stong, B. (2018). Improved Quantification of Gibbsite in Bauxite Ores by Thermogravimetric Methods (TGA and DTG). *Advances in Applied Chemistry and Biochemistry*, 1(1), 9–17. <https://doi.org/10.33513/acbc/1801-02>
- Ekosse, G.-I. E. (2005). Fourier Transform Infrared Spectrophotometry and X-ray powder Diffractometry as Complementary Techniques in characterizing Clay size fraction of Kaolin. *J. Appl. Environ. MGT*, 9(2), 43–48. www.bioline.org.br/ja
- Farmer, V. C. (1968). Infrared spectroscopy in clay mineral studies. *Clay Minerals*, 7, 373–387.
- Fennell, P., Driver, J., Bataille, C., & Davis, S. J. (2022). Going net zero for cement and steel. *Springer Nature*, 603, 574–577.
- Filho, R. W. N. D., De Araujo Rocha, G., Montes, C. R., & Vieira-Coelho, A. C. (2016). Synthesis and characterization of boehmites obtained from gibbsite in presence of different environments. *Materials Research*, 19(3), 659–668. <https://doi.org/10.1590/1980-5373-MR-2016-0019>
- Földvári, M. 1944-. (2011). *Handbook of thermogravimetric system of minerals and its use in geological practice*. Geological Institute of Hungary.
- Fransen, T., Lebling, K., Weyl, D., & Kennedy, K. (2021). Toward a Tradable Low-Carbon Cement Standard: Policy Design Considerations for the United States. *World Resources Institute*. <https://doi.org/10.46830/wriwp.20.00112>
- Galán, E. (1981). *Posibilidades de utilización de materias primas españolas en la fabricación de refractarios silicoaluminosos y de alta alumina* (Vol. 20). Bol. soc. esp. ceram. vidr.
- Garcia-Valles, M., Alfonso, P., Martínez, S., & Roca, N. (2020). Mineralogical and thermal characterization of kaolinitic clays from Terra Alta (Catalonia, Spain). *Minerals*, 10(2). <https://doi.org/10.3390/min10020142>
- Garcia-Valles, M., Cuevas, D., Alfonso, P., & Martínez, S. (2022). Thermal behaviour of ceramics obtained from the kaolinitic clays of Terra Alta, Catalonia, Spain. *Journal of Thermal Analysis and Calorimetry*, 147(9), 5303–5312. <https://doi.org/10.1007/s10973-021-11075-9>
- Garcia-Valles, M., Pi, T., Alfonso, P., Canet, C., Martínez, S., Jiménez-Franco, A., Tarrago, M., & Hernández-Cruz, B. (2015). Kaolin from Acoculco (Puebla, Mexico) as raw material: Mineralogical and thermal characterization. *Clay Minerals*, 50(3), 405–416. <https://doi.org/10.1180/claymin.2015.050.3.12>
- Gippini, E. (1979). *Pastas cerámicas*. Sociedad Española de cerámica.

- Guatame-Garcia, A., & Buxton, M. (2018). Prediction of soluble Al₂O₃ in calcined kaolin using infrared spectroscopy and multivariate calibration. *Minerals*, 8(4), 1–14. <https://doi.org/10.3390/min8040136>
- Hinckley, D. N. (1965). *Mineralogical and chemical variations in kaolin deposits of the coastal plain of Georgia and South Carolina*.
- IGME. (1972). Programa sectorial de exploración de bauxita. Fase previa para la investigación de bauxita en el subsector 1. Cataluña, área 3, La Llacuna (Barcelona y Tarragona). *Informe IGME*.
- Kloprogge, J. T., Ruan, H. D., & Frost, R. L. (2002). Thermal decomposition of bauxite minerals: Infrared emission spectroscopy of gibbsite, boehmite and diasporite. *Journal of Materials Science*, 37(6), 1121–1129. <https://doi.org/10.1023/A:1014303119055>
- La Iglesia, Á., & Ordoñez, S. (1990). Cristalinidad de caolinitas en yacimientos de bauxitas carsticas del NE España. *Boletín de La Sociedad Española de Mineralogía*, 13, 81–90.
- Li, Y., Eyley, S., Thielemans, W., Yuan, Q., & Li, J. (2022). Valorization of deep soil mixing residue in cement-based materials. *Resources, Conservation and Recycling*, 187. <https://doi.org/10.1016/j.resconrec.2022.106597>
- Lyu, S., Wang, Y., Huang, J., Li, T., Li, D., Wang, J. K., Zhang, J., Sun, D., & Yu, P. (2021). Sintering behaviors and properties of porous ceramics derived from artificially cultured diatom frustules. *Journal of the American Ceramic Society*, 104(5), 2378–2387. <https://doi.org/10.1111/jace.17611>
- Mañosa, J., Gómez-Carrera, A. M., Svobodova-Sedlackova, A., Maldonado-Alameda, A., Fernández-Jiménez, A., & Chimenos, J. M. (2022). Potential reactivity assessment of mechanically activated kaolin as alternative cement precursor. *Applied Clay Science*, 228. <https://doi.org/10.1016/j.clay.2022.106648>
- Martinez Manent, S., & Ballbe Llonch, E. (1985). Metodo de diferenciacion de caolinitas y cloritas. *Acta Geologica Hispanica*, 20(3–4), 245–255.
- Miller, S. A., Horvath, A., & Monteiro, P. J. M. (2018). Impacts of booming concrete production on water resources worldwide. *Nature Sustainability*, 1(1), 69–76. <https://doi.org/10.1038/s41893-017-0009-5>
- Molina, J. M. (1991). *A review of karst bauxites and related paleokarsts in Spain The Aptian of the Prebetic: Environmental and biotic changes and controlling factors View project South Iberian paleomargin View project*. <https://www.researchgate.net/publication/313172880>
- Montoya, N., Serrano, F. J., Reventós, M. M., Amigo, J. M., & Alarcón, J. (2010). Effect of TiO₂ on the mullite formation and mechanical properties of alumina porcelain. *Journal of the European Ceramic Society*, 30(4), 839–846. <https://doi.org/10.1016/j.jeurceramsoc.2009.10.009>
- Moore, D. M., & Reynolds, R. C. , Jr. (1989). *X-ray diffraction and the identification and analysis of clay minerals*.
- Murray, H. H. (2000). Traditional and new applications for kaolin, smectite, and palygorskite: a general overview. In *Applied Clay Science* (Vol. 17). www.elsevier.nl/locate/clay

- Negrão, L. B. A., Pöllmann, H., & Costa, M. L. da. (2021). Production of low-CO₂ cements using abundant bauxite overburden “Belterra Clay.” *Sustainable Materials and Technologies*, 29. <https://doi.org/10.1016/j.susmat.2021.e00299>
- Ordoñez, S. (1977). *Las bauxitas españolas como mena de aluminio*. Fundación Juan March.
- Plançon, A., Giese, R. F., & Snyderf, R. (1988). The Hinkley index for kaolinites. In *Clay Minerals* (Vol. 23).
- Prasad, M. S., Reid, K. J., & Murray, H. H. (1991). Kaolin: processing, properties and applications. In *Applied Clay Science* (Vol. 6).
- Ramachandran, V. S., Paroli, R. M., Beaudoin, J. J., & Delgado, A. H. (2002). *Handbook of thermal analysis of construction materials*. Noyes Publications.
- Rehan, R., & Nehdi, M. (2005). Carbon dioxide emissions and climate change: Policy implications for the cement industry. *Environmental Science and Policy*, 8(2), 105–114. <https://doi.org/10.1016/j.envsci.2004.12.006>
- Reinhardt, N., Proenza, J. A., Villanova-De-benavent, C., Aiglsperger, T., Bover-Arnal, T., Torró, L., Salas, R., & Dziggel, A. (2018). Geochemistry and mineralogy of rare earth elements (REE) in bauxitic ores of the catalan coastal range, NE Spain. *Minerals*, 8(12). <https://doi.org/10.3390/min8120562>
- Rivas Mercury, J. M., Cabral, A. A., Paiva, A. E. M., Angélica, R. S., Neves, R. F., & Scheller, T. (2010). Thermal Behavior and evolution of the mineral phases of Brazilian red mud. *J Therm Anal Calorim*, 104, 635–643.
- Romero, J., & Prats, M. (1995). *Estudi sobre les bauxites de la llacuna*.
- Sanjuán, M. Á., Andrade, C., Mora, P., & Zaragoza, A. (2020). Carbon dioxide uptake by cement-based materials: A spanish case study. *Applied Sciences (Switzerland)*, 10(1). <https://doi.org/10.3390/app10010339>
- Schneider, H., Majdic, A., & Vasudevan, R. (1986). Kinetics of the quartz-cristobalite transformation in refractory- grade silica materials. *Kinetics and Mass Transport in Silicate and Oxide Systems*, 91–102. <https://doi.org/10.4028/www.scientific.net/msf.7.91>
- Schneider, M., Romer, M., Tschudin, M., & Bolio, H. (2011). Sustainable cement production-present and future. *Cement and Concrete Research*, 41(7), 642–650. <https://doi.org/10.1016/j.cemconres.2011.03.019>
- Todor, D. (1976). *Thermal Analysis of Minerals*. Abacus Press.
- Vaculíková, L., Plevová, E., Koutník, I., Vaculíková, L., Vallová, S., & Koutník, I. (2011). Characterization and differentiation of kaolinites from selected czech deposits using infrared spectroscopy and differential thermal analysis. *Acta Geodyn. Geomater*, 8(1), 59–67. <https://www.researchgate.net/publication/228520072>
- Vasić, M. V., Pezo, L., Zdravković, J. D., Bačkalić, Z., & Radojević, Z. (2017). The study of thermal behavior of montmorillonite and hydromica brick clays in predicting tunnel kiln firing curve. *Construction and Building Materials*, 150, 872–879. <https://doi.org/10.1016/j.conbuildmat.2017.06.068>
- Vergés, J., & Muñoz, J. A. (1990). *Thrust sequences int the southern central Pyrenees*.

Wang, Y., Xing, S., Zhang, Y., Li, Z., Ma, Y., & Zhang, Z. (2015). Mineralogical and thermal characteristics of low-grade Jinlong bauxite sourced from Guangxi Province, China. *Journal of Thermal Analysis and Calorimetry*, 122(2), 917–927. <https://doi.org/10.1007/s10973-015-4742-6>

Worasith, N., Goodman, B. A., Neampan, J., Jeyachoke, N., & Thiravetyan, P. (2011). Characterization of modified kaolin from the Ranong deposit Thailand by XRD, XRF, SEM, FTIR and EPR techniques. *Clay Minerals*, 46, 539–559. <https://doi.org/10.1180/claymin.2011.046.3.539>

Yuste, A., Bauluz, B., & Mayayo, M. J. (2015). Genesis and mineral transformations in Lower Cretaceous karst bauxites (NE Spain): Climatic influence and superimposed processes. *Geological Journal*, 50(6), 839–857. <https://doi.org/10.1002/gj.2604>

Yuste, A., Bauluz, B., & Mayayo, M. J. (2017). Origin and geochemical evolution from ferrallitized clays to karst bauxite: An example from the Lower Cretaceous of NE Spain. *Ore Geology Reviews*, 84, 67–79. <https://doi.org/10.1016/j.oregeorev.2016.12.025>

Annex

In the following pages can be found some additional data which can be useful to understand some of the results exposed and the discussions followed.

Sample localization/field description

Sant Joan de Mediona

- JM-1 and JM-2: Samples taken nearby the entrance of the old mine.

Peramola

- PER-1: Samples from a dump around 30m below the gallery entrance
- PER-2: Materials from inside the gallery. Presence of calcite and clays



- PER-3: Materials from the dump in front of gallery entrance



- PER-10: Materials from upper outcrop
 - o V: Red materials, main ore body, bauxite
 - o B: White material, inside main ore body



- G: Yellow material, contact material with main ore body



- PER-11: Material from a second upper outcrop, around 20m westside from PER-10 outcrop.
 - A: Bauxite, front side of the outcrop
 - B: Red material, back side of the outcrop



- PER-12: Materials found at the sideways of the main path. Dumped material from upper levels. Found few meters above the gallery entrance.



- PER-14: Material from the main gallery zone
 - o 1: Tailing material, took from inside mine build debris.



- 2: Material from the dump in front of gallery entrance, like PER-3 sample
- 3: Material from inside the gallery. Clay materials.



- PER-15: Material from the same dump as PER-1, around 30m below the gallery entrance.
 - 1: Random rocks taken from surface.
 - 2: Mixed material taken randomly from different point of the dump.



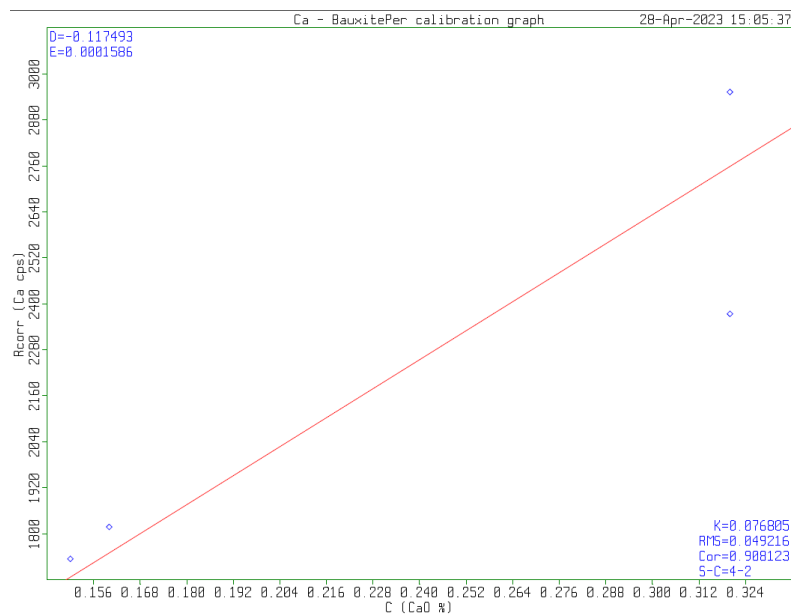
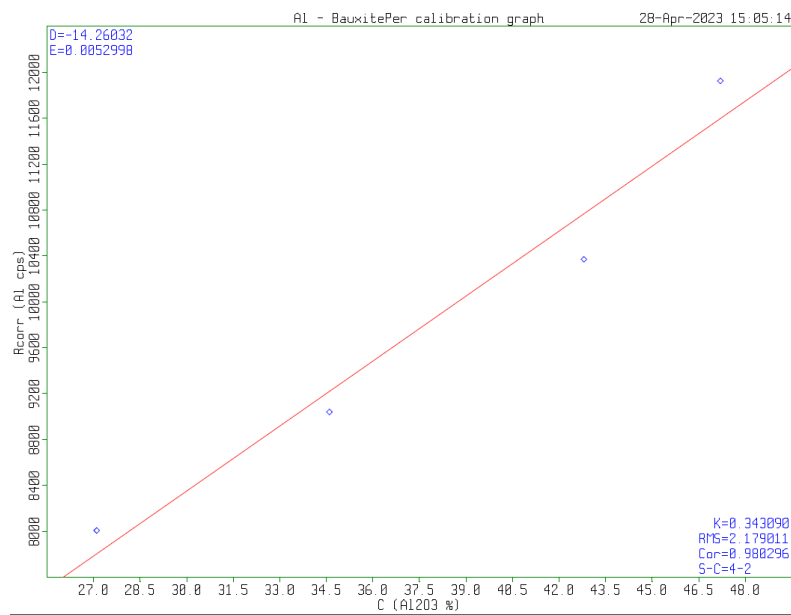
- 3: Red rock, in situ material, found in an outcrop between limestones.
- 4: Red mud, from the outcrop of PER-15-3.

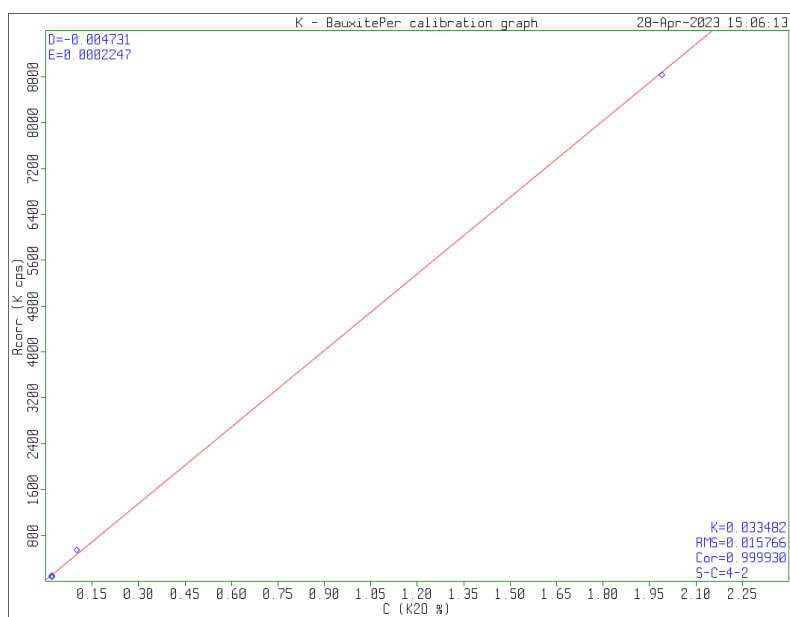
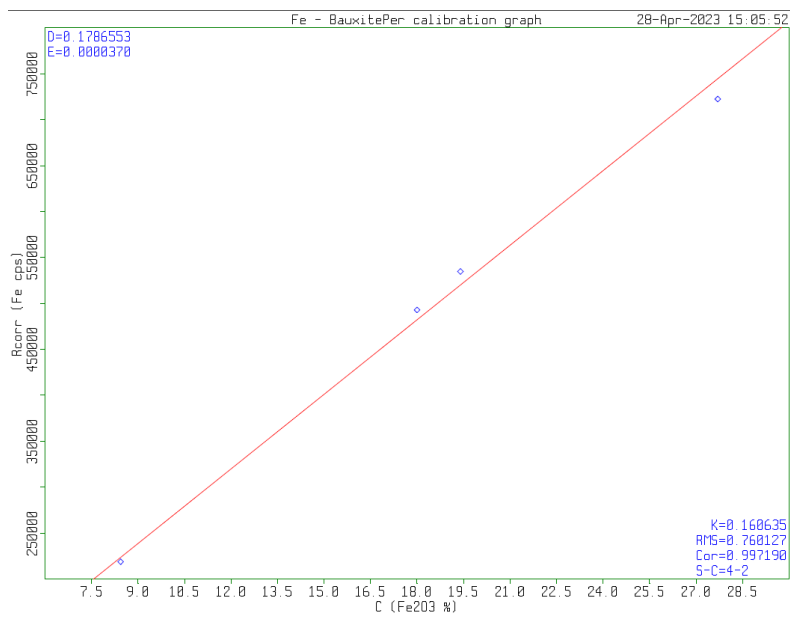


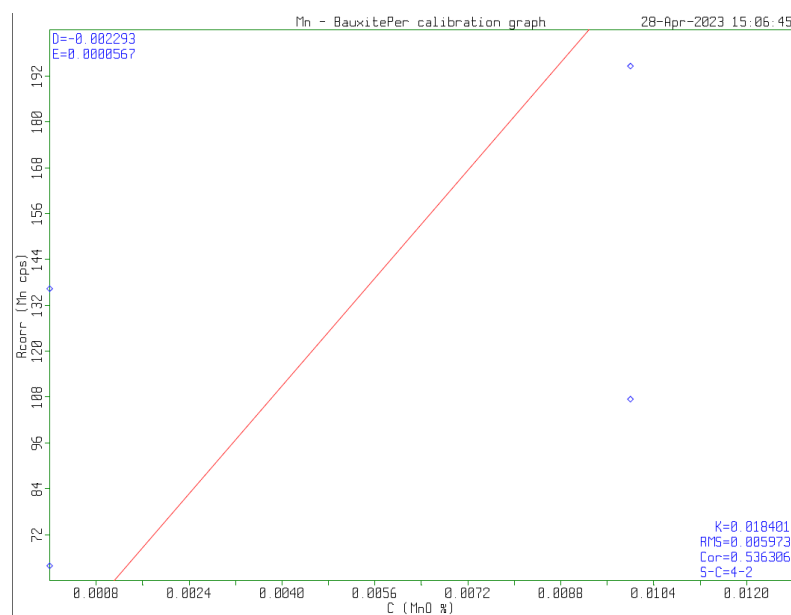
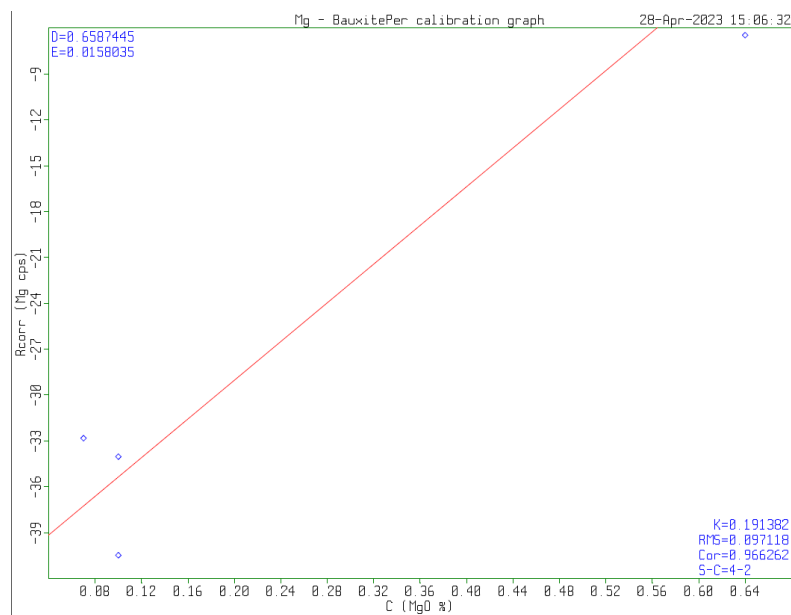
XRF Calibration

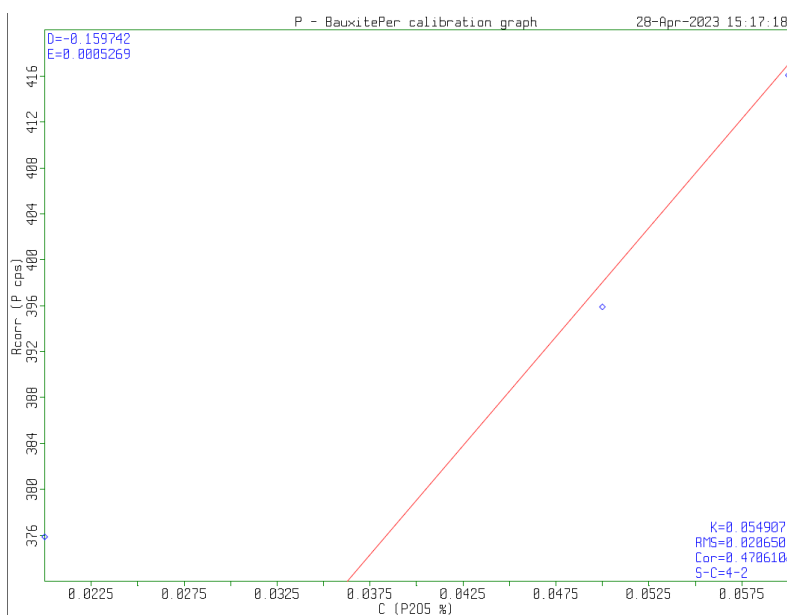
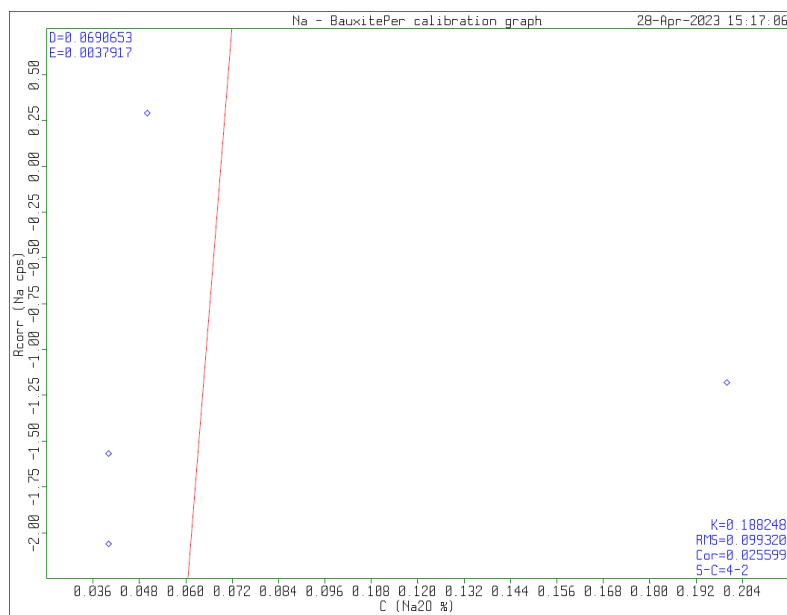
Calibration graph and reports

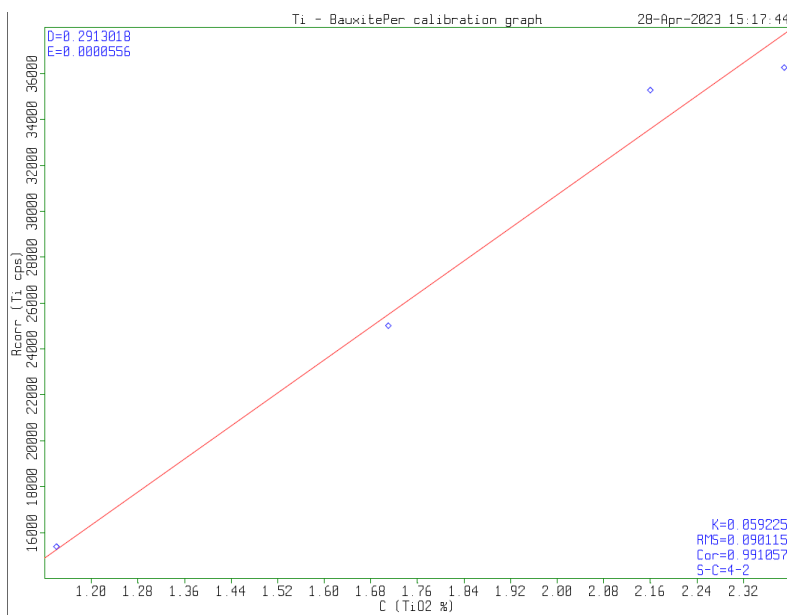
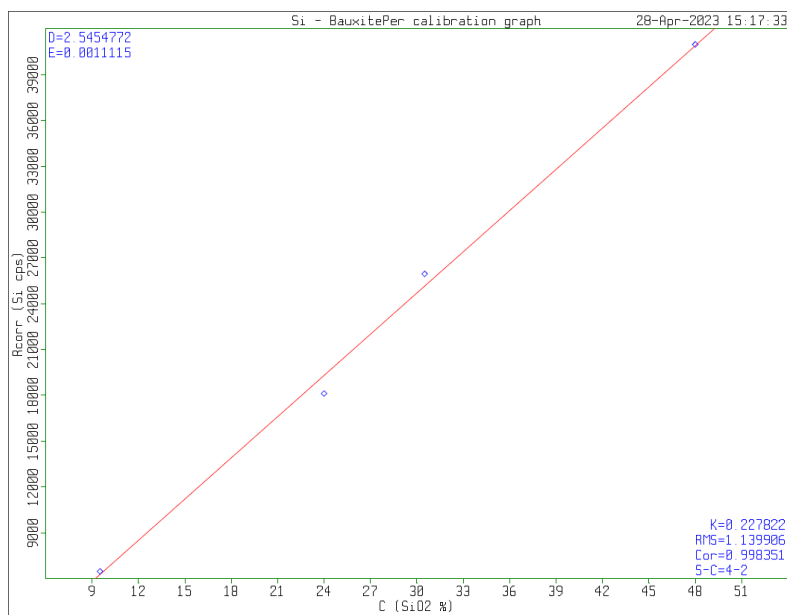
The following figures show the calibration graph and reports done with Epsilon1 XRF from Escola Politècnica Superior d'Enginyeria de Manresa (EPSEM). Samples JM-2, PER-10, PER-11, PER-12, PER-14 and PER-15 have been analysed with this device. JM-1, PER-1, PER-2B, PER-3 were analysed by inductive coupled analysis they were used as standard for calibration procedure.











Al - BauxitePer calibration report

Parameters

D value	-14.2603
E value	0.005300
F value	0.0000000
Ratio channel	None
K factor	0.343090
RMS value	2.179011
Correlation coefficient	0.980296
Nr Standards - Coefficients	4-2
Concentration unit	%

Ident	Qual	I (cps)	Calc	Chem	Diff	D/RMS	L.Ov	Matrix
JM1	High	10370.3	40.70	42.80	-2.10	-0.96	0.000	1.000000
PER1	High	11924.6	48.94	47.20	1.74	0.80	0.000	1.000000
PER2b	High	8007.44	28.18	27.10	1.08	0.49	0.000	1.000000
PER3	High	9039.64	33.65	34.60	-0.95	-0.44	0.000	1.000000

Ca - BauxitePer calibration report

Parameters

D value	-0.11749
E value	0.000159
F value	0.0000000
Ratio channel	None
K factor	0.076805
RMS value	0.049216
Correlation coefficient	0.908123
Nr Standards - Coefficients	4-2
Concentration unit	%

Ident	Qual	I (cps)	Calc	Chem	Diff	D/RMS	L.Ov	Matrix
JM1	High	1817.61	0.17	0.16	0.01	0.22	0.000	1.000000
PER1	High	1734.33	0.16	0.15	0.01	0.15	0.000	1.000000
PER2b	High	2373.79	0.26	0.32	-0.06	-1.24	0.000	1.000000
PER3	High	2952.68	0.35	0.32	0.03	0.63	0.000	1.000000

Fe - BauxitePer calibration report

Parameters

D value	0.178655
E value	0.000037
F value	0.0000000
Ratio channel	None
K factor	0.160635
RMS value	0.760127
Correlation coefficient	0.997190
Nr Standards - Coefficients	4-2
Concentration unit	%

Ident	Qual	I (cps)	Calc	Chem	Diff	D/RMS	L.Ov	Matrix
JM1	High	492865.	18.40	18.00	0.40	0.52	0.000	1.000000
PER1	High	722454.	26.88	27.70	-0.82	-1.08	0.000	1.000000
PER2b	High	218806.	8.27	8.44	-0.17	-0.23	0.000	1.000000
PER3	High	534826.	19.95	19.40	0.55	0.72	0.000	1.000000

K - BauxitePer calibration report

Parameters

D value	-0.00473
E value	0.000225
F value	0.0000000
Ratio channel	None
K factor	0.033482
RMS value	0.015766
Correlation coefficient	0.999930
Nr Standards - Coefficients	4-2
Concentration unit	%

Ident	Qual	I (cps)	Calc	Chem	Diff	D/RMS	L.Ov	Matrix
JM1	High	97.855	0.02	0.02	0.00	-0.17	0.000	1.000000
PER1	High	76.308	0.01	0.02	-0.01	-0.48	0.000	1.000000
PER2b	High	8831.83	1.98	1.99	-0.01	-0.64	0.000	1.000000
PER3	High	546.940	0.12	0.10	0.02	1.15	0.000	1.000000

Mg - BauxitePer calibration report

Parameters

D value	0.658745
E value	0.015803
F value	0.0000000
Ratio channel	None
K factor	0.191382
RMS value	0.097118
Correlation coefficient	0.966262
Nr Standards - Coefficients	4-2
Concentration unit	%

Ident	Qual	I (cps)	Calc	Chem	Diff	D/RMS	L.Ov	Matrix
JM1	High	-34.026	0.12	0.10	0.02	0.22	0.000	1.000000
PER1	High	-32.819	0.14	0.07	0.07	0.72	0.000	1.000000
PER2b	High	-6.466	0.56	0.64	-0.08	-0.86	0.000	1.000000
PER3	High	-40.476	0.02	0.10	-0.08	-0.83	0.000	1.000000

Mn - BauxitePer calibration report

Parameters

D value	-0.00229
E value	0.000057
F value	0.0000000
Ratio channel	None
K factor	0.018401
RMS value	0.005973
Correlation coefficient	0.536306
Nr Standards - Coefficients	4-2
Concentration unit	%

Ident	Qual	I (cps)	Calc	Chem	Diff	D/RMS	L.Ov	Matrix
JM1	High	194.578	0.01	0.01	0.00	-0.21	0.000	1.000000
PER1	High	136.345	0.01	0.00	0.01	0.91	0.000	1.000000
PER2b	High	63.845	0.00	0.00	0.00	0.22	0.000	1.000000
PER3	High	107.460	0.00	0.01	-0.01	-1.04	0.000	1.000000

Na - BauxitePer calibration report

Parameters

D value	0.069065
E value	0.003792
F value	0.000000
Ratio channel	None
K factor	0.188248
RMS value	0.099320
Correlation coefficient	0.025599
Nr Standards - Coefficients	4-2
Concentration unit	%

Ident	Qual	I (cps)	Calc	Chem	Diff	D/RMS	L.Ov	Matrix
JM1	High	0.290	0.07	0.05	0.02	0.20	0.000	1.000000
PER1	High	-1.568	0.06	0.04	0.02	0.23	0.000	1.000000
PER2b	High	-1.180	0.06	0.20	-0.14	-1.36	0.000	1.000000
PER3	High	-2.061	0.06	0.04	0.02	0.21	0.000	1.000000

P - BauxitePer calibration report

Parameters

D value	-0.15974
E value	0.000527
F value	0.000000
Ratio channel	None
K factor	0.054907
RMS value	0.020650
Correlation coefficient	0.470610
Nr Standards - Coefficients	4-2
Concentration unit	%

Ident	Qual	I (cps)	Calc	Chem	Diff	D/RMS	L.Ov	Matrix
JM1	High	416.070	0.06	0.06	0.00	-0.02	0.000	1.000000
PER1	High	395.888	0.05	0.05	0.00	-0.05	0.000	1.000000
PER2b	High	373.915	0.04	0.06	-0.02	-1.10	0.000	1.000000
PER3	High	375.864	0.04	0.02	0.02	0.89	0.000	1.000000

Si - BauxitePer calibration report

Parameters

D value	2.545477
E value	0.001112
F value	0.000000
Ratio channel	None
K factor	0.227822
RMS value	1.139906
Correlation coefficient	0.998351
Nr Standards - Coefficients	4-2
Concentration unit	%

Ident	Qual	I (cps)	Calc	Chem	Diff	D/RMS	L.Ov	Matrix
JM1	High	18115.6	22.68	24.00	-1.32	-1.16	0.000	1.000000
PER1	High	6469.36	9.74	9.51	0.23	0.20	0.000	1.000000
PER2b	High	40980.0	48.10	48.00	0.10	0.08	0.000	1.000000
PER3	High	25954.3	31.39	30.50	0.89	0.78	0.000	1.000000

Ti - BauxitePer calibration report

Parameters

D value	0.291302
E value	0.000056
F value	0.0000000
Ratio channel	None
K factor	0.059225
RMS value	0.090115
Correlation coefficient	0.991057
Nr Standards - Coefficients	4-2
Concentration unit	%

Ident	Qual	I (cps)	Calc	Chem	Diff	D/RMS	L.Ov	Matrix
JM1	High	36257.4	2.31	2.39	-0.08	-0.90	0.000	1.000000
PER1	High	35276.0	2.25	2.16	0.09	1.04	0.000	1.000000
PER2b	High	15389.7	1.15	1.14	0.01	0.08	0.000	1.000000
PER3	High	25015.9	1.68	1.71	-0.03	-0.30	0.000	1.000000

Some elements such as sodium or manganese show poor calibration accuracy. For this reason, this calibration is used only for major elements as Si, Al, Fe and Ca

Standard	XRF analisys through calibration				
	JM-1 (Standard)	JM1	JM1/2022/12/01/	JM2/2022/12/01/	JM2/2022/12/05/
SiO ₂	24	24.17	25.13	26.06	23.43
	%	%	%	%	%
Al ₂ O ₃	42.8	41.4	43.81	24.75	16.69
	%	%	%	%	%
Fe ₂ O ₃	18	18.99	19.27	9.28	8.21
	%	%	%	%	%
CaO	0.16	0.16	0.16	22.01	24.52
	%	%	%	%	%

The raw data obtained through the automatic program from Epsilon1 XRF is

Nr	Ident	1	2	3	4	5	6
		PER-1 omnian	PER-2B omnian	PER-3 omnian	JM-1 omnian	JM-2 omnian	PER-14-2 omnian
Na2O	C	0	0	0	0	0	0
	Unit	ppm	ppm	ppm	ppm	ppm	ppm
MgO	C	0	0.425	0	0	0.449	0
	Unit	ppm	%	ppm	ppm	%	ppm
Al2O3	C	44.742	26.723	31.76	37.114	21.752	40.617
	Unit	%	%	%	%	%	%
SiO2	C	9.489	42.759	28.221	22.157	19.805	9.733
	Unit	%	%	%	%	%	%
P2O5	C	0.361	0.343	0.348	0.367		0.358
	Unit	%	%	%	%		%
SO3	C	0.18	0.265	0.119	0.113	0.102	0.116
	Unit	%	%	%	%	%	%
K2O	C	305.4	2.186	0.137	385.8	0.591	297
	Unit	ppm	%	%	ppm	%	ppm
CaO	C	0.358	0.417	0.435	0.288	24.156	0.4
	Unit	%	%	%	%	%	%
TiO2	C	2.433	1.194	1.747	2.498	1.491	2.315
	Unit	%	%	%	%	%	%
V2O5	C	0.113	319.7	615.9	0.102	520.8	0.104
	Unit	%	ppm	ppm	%	ppm	%
Cr2O3	C	753.4	206.2	414.9	666.4	412.5	710.1
	Unit	ppm	ppm	ppm	ppm	ppm	ppm
MnO	C	138.1	58.4	0	145.1	171.8	155.6
	Unit	ppm	ppm	ppm	ppm	ppm	ppm
Fe2O3	C	26.505	7.098	18.182	16.615	11.387	29.449
	Unit	%	%	%	%	%	%

Chemical Composition

Chemical Composition, Major Oxides Table

Oxides	JM-1	JM-2	PER-1	PER2-A	PER-2B	PER-2C	PER-3	PER-10V	PER-10B	PER-10G	PER-11A	PER-11B	PER-14-1	PER-14-2	PER-14-3	PER-15-1	PER-15-2	PER-15-3	PER-15-4
SiO ₂	24.00	23.43	9.51	83.56	48.00	2.35	30.50	7.91	25.58	42.46	29.10	47.03	15.24	11.30	37.87	10.46	24.88	10.39	16.75
Al ₂ O ₃	42.80	16.69	47.20	7.56	27.10	0.67	34.60	47.95	59.67	10.42	33.13	12.66	30.95	47.17	31.26	37.57	38.64	46.14	41.64
Fe ₂ O ₃	18.00	8.21	27.70	0.15	8.44	1.81	19.40	37.56	1.84	4.09	24.74	5.85	29.08	34.20	13.71	44.57	21.20	35.91	24.80
CaO	0.16	24.52	0.15	0.40	0.32	49.74	0.32	0.35	0.39	14.51	1.02	8.69	9.81	0.46	0.34	0.75	2.68	0.61	4.76
MgO	0.10	0.43	0.07	0.33	0.64	4.76	0.10	0.00	0.00	0.59	0.00	0.73	0.00	0.00	0.00	0.00	0.00	0.00	0.00
Na ₂ O	0.05	0.06	0.04	0.00	0.20	0.00	0.04	0.00	0.00	0.00	0.00	0.00	0.00	0.00	0.00	0.00	0.00	0.00	0.00
K ₂ O	0.02	0.60	0.02	6.08	1.99	0.22	0.10	0.04	0.06	2.87	0.08	2.88	0.17	0.00	3.14	0.06	0.32	0.01	0.23
TiO ₂	2.39	0.95	2.16	0.00	1.14	0.00	1.71	3.07	3.98	0.52	2.00	0.82	2.06	2.69	1.64	2.42	2.28	2.89	2.65
MnO	0.01	0.01	0.00	0.00	0.00	0.01	0.01	0.00	0.00	0.00	0.00	0.02	0.02	0.00	0.00	0.00	0.00	0.00	0.00
P ₂ O ₅	0.06	0.08	0.05	0.44	0.06	0.33	0.02	0.48	0.50	0.43	0.41	0.42	0.41	0.42	0.41	0.44	0.43	0.46	0.42
LOI	12.85	25.10	12.40	1.48	11.85	40.12	12.95	2.65	7.98	24.12	9.52	20.93	12.27	3.75	11.63	3.72	9.57	3.60	8.76
Total	100.44	100.08	99.30	100.00	99.74	100.01	99.75	100.00	100.00	100.00	100.00	100.02	100.02	100.00	100.00	100.00	100.00	100.00	100.00

Chemical Composition, Minor elements Table

Samples	Ba	Ce	Cr	Cs	Dy	Er	Eu	Ga	Gd	Hf	Ho	La	Lu	Nb	Nd	Pr	Rb	Sm	Sn	Sr	Ta	Tb	Th	Tm	U	V	W	Y	Yb	Zr
	ppm	ppm	ppm	ppm	ppm	ppm	ppm	ppm	ppm	ppm	ppm	ppm	ppm	ppm	ppm	ppm	ppm	ppm	ppm	ppm	ppm	ppm	ppm	ppm	ppm	ppm	ppm	ppm	ppm	
Per-1	23.6	27.1	430	0.18	5.79	4.06	0.65	65.1	3.73	17	1.32	7.9	0.67	50.8	8.6	1.98	1.5	2.56	33	48.3	4.1	0.82	43.6	0.66	11.4	665	8	36.8	4.39	646
Per-2b	540	88.8	140	19.05	12	6.73	2.8	38.2	12.9	6.5	2.46	67.7	0.91	26.2	66.9	16.35	122.5	13.65	14	132.5	2.3	1.93	22.5	1	3.93	199	11	80.3	6.06	242
Per-3	39.5	77.4	240	0.79	7.11	4.45	1.16	47.6	5.6	13.9	1.54	22.9	0.76	40	25	6.16	5	5.56	14	41.3	2.2	1.08	31.6	0.73	7.27	344	7	40.7	4.62	546
JM-1	20.4	60.8	430	0.07	7.75	5.28	0.93	67.9	4.99	16.4	1.78	33.7	0.89	52.8	18.3	5.65	0.5	3.2	13	166.5	4.1	1.07	45.6	0.91	5.92	553	6	49.6	5.81	636

Mineralogy

Thin plate

JM-1

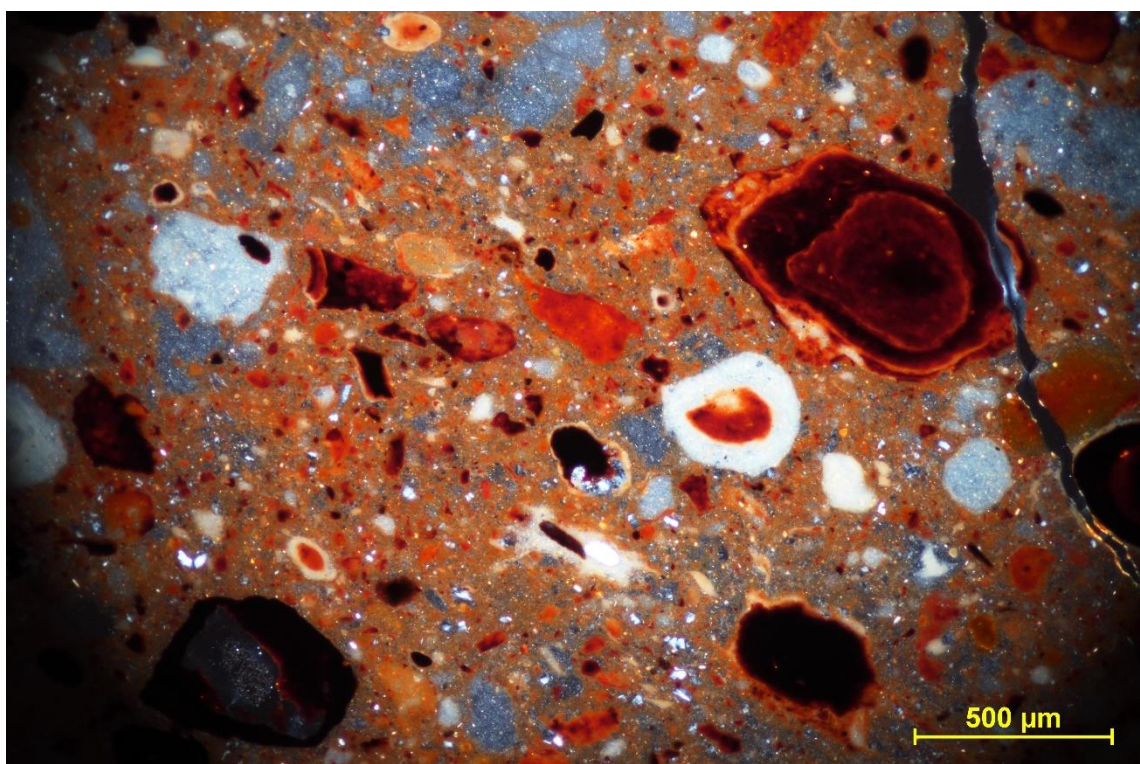
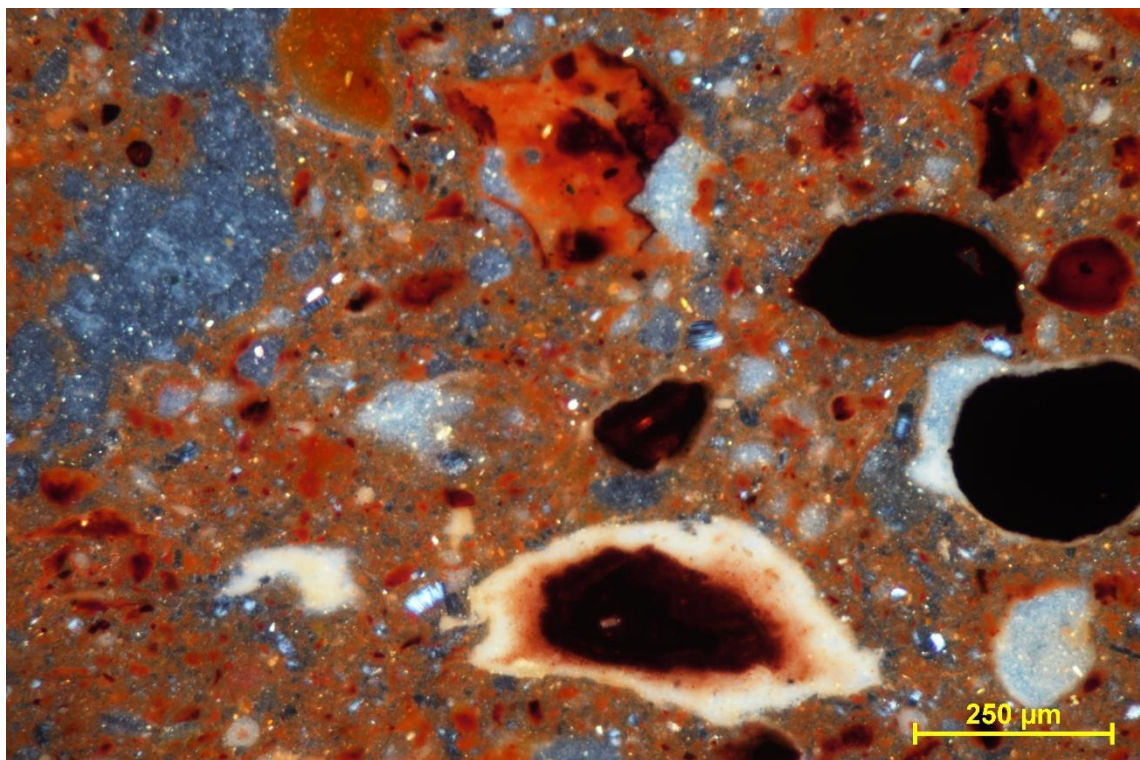


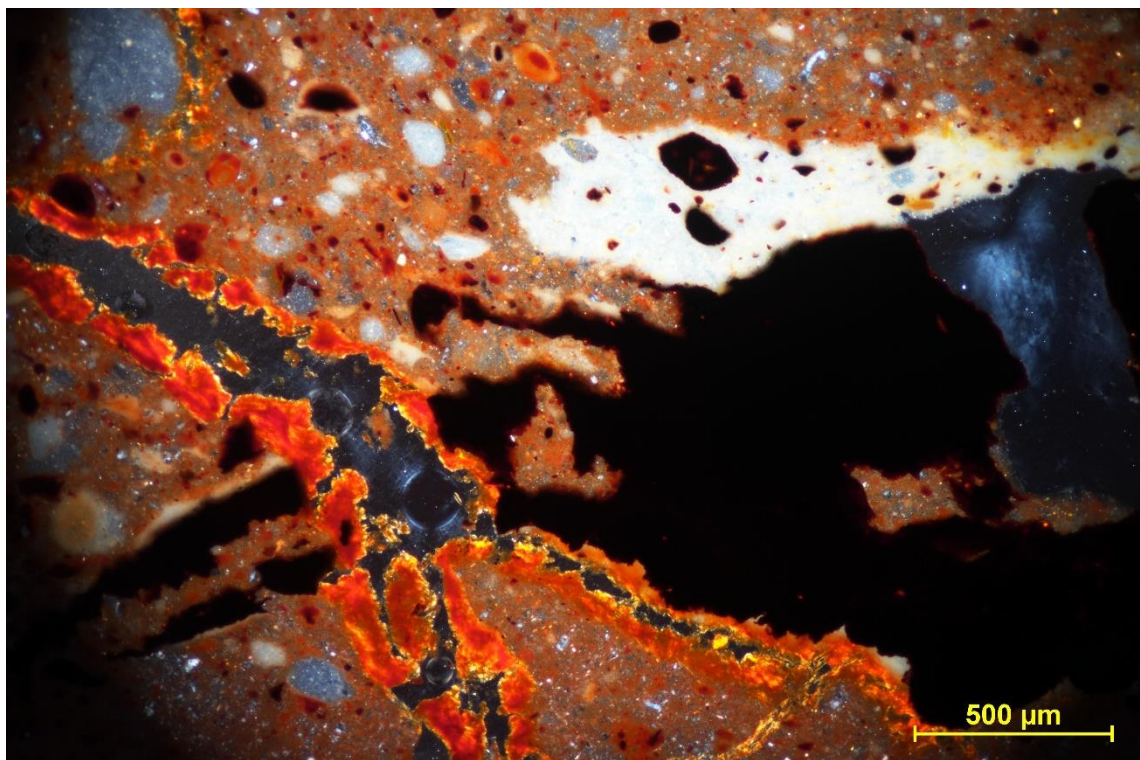
Low order, Immature stage, high percentage of kaolinite.

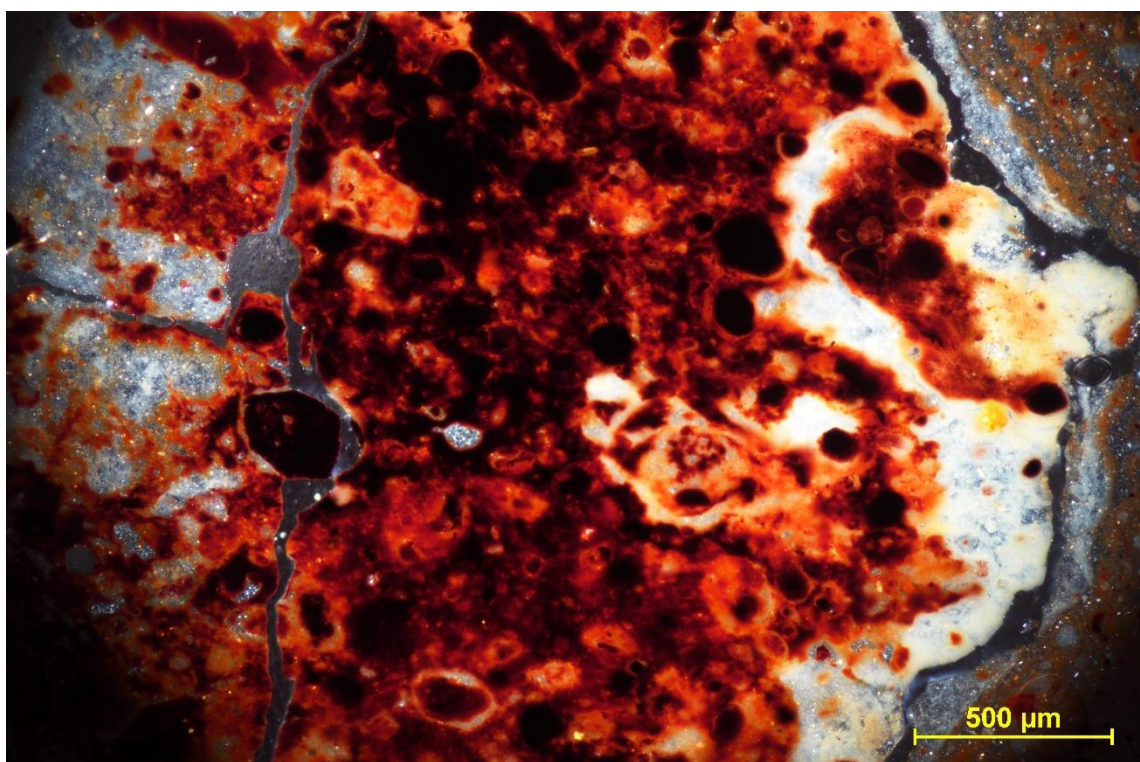
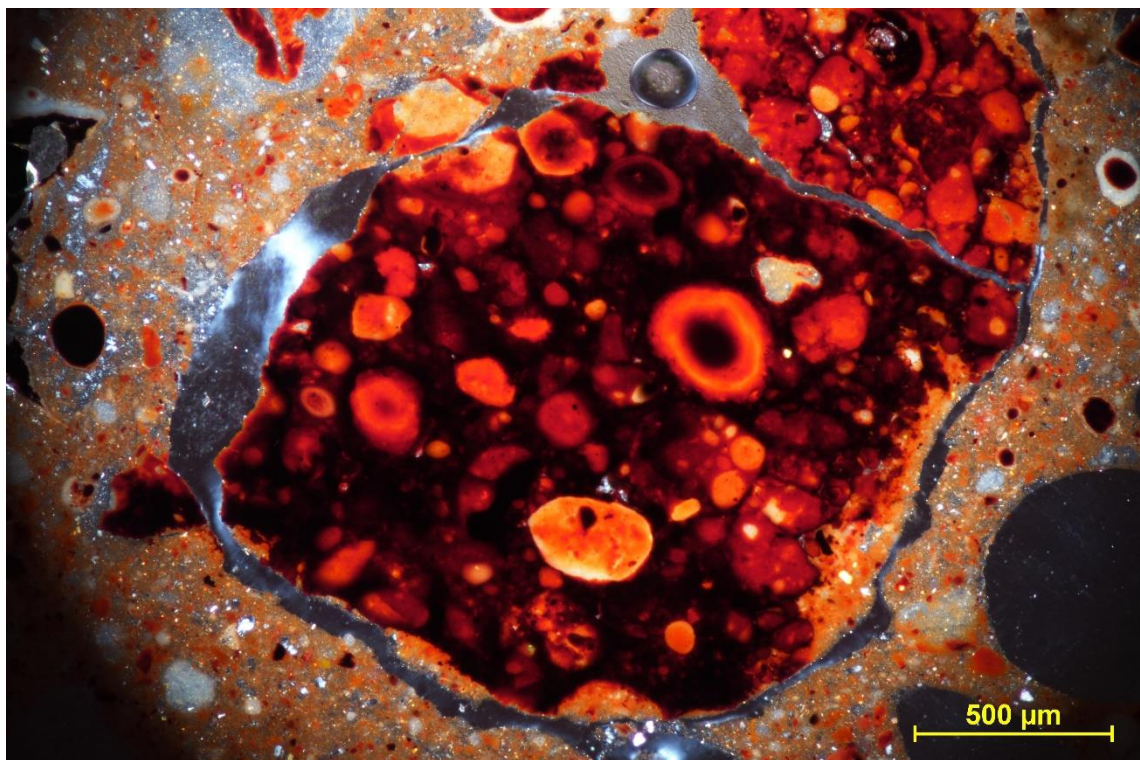
Greywacke → Lithic greywacke

Variable particle size, from few millimetres to lower than 63µm.

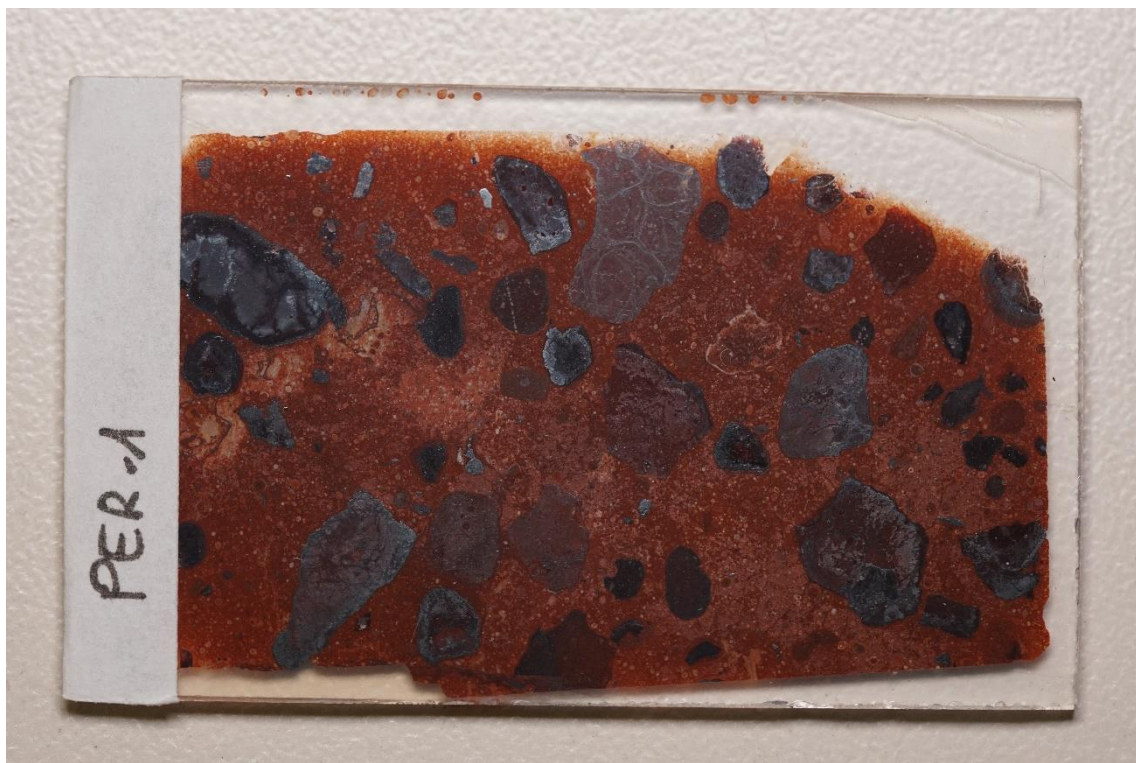
For the matrix can be spotted kaolinite and some quarts. Iron and aluminium oxides are the majority of bigger particles (which can be seen clearly in these images). Iron (red) and aluminium (white) are found most of the together, having a zonation generally from aluminium inside to more iron outside.



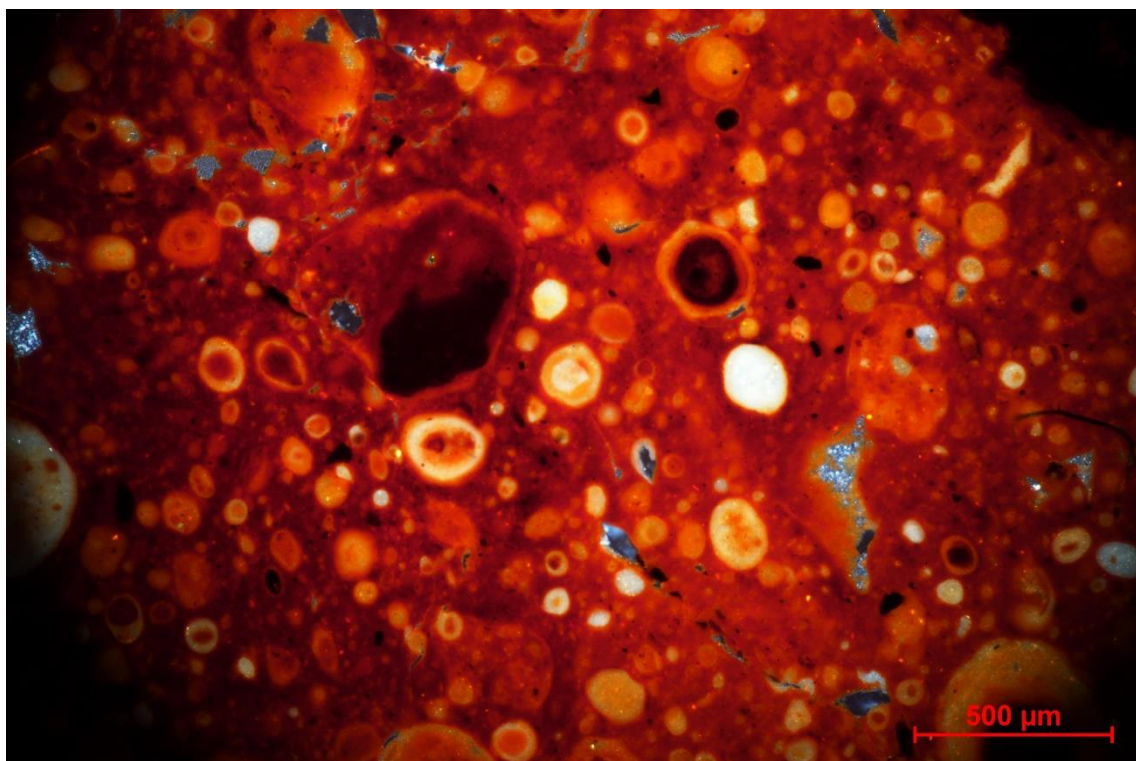


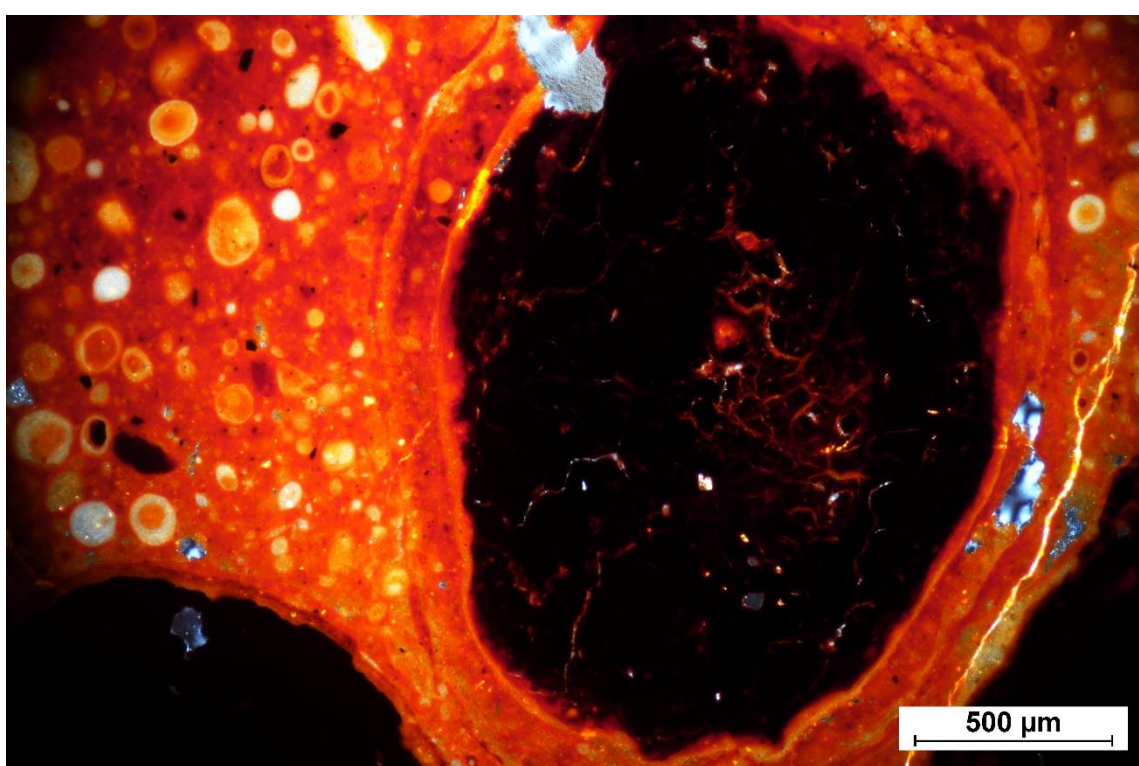
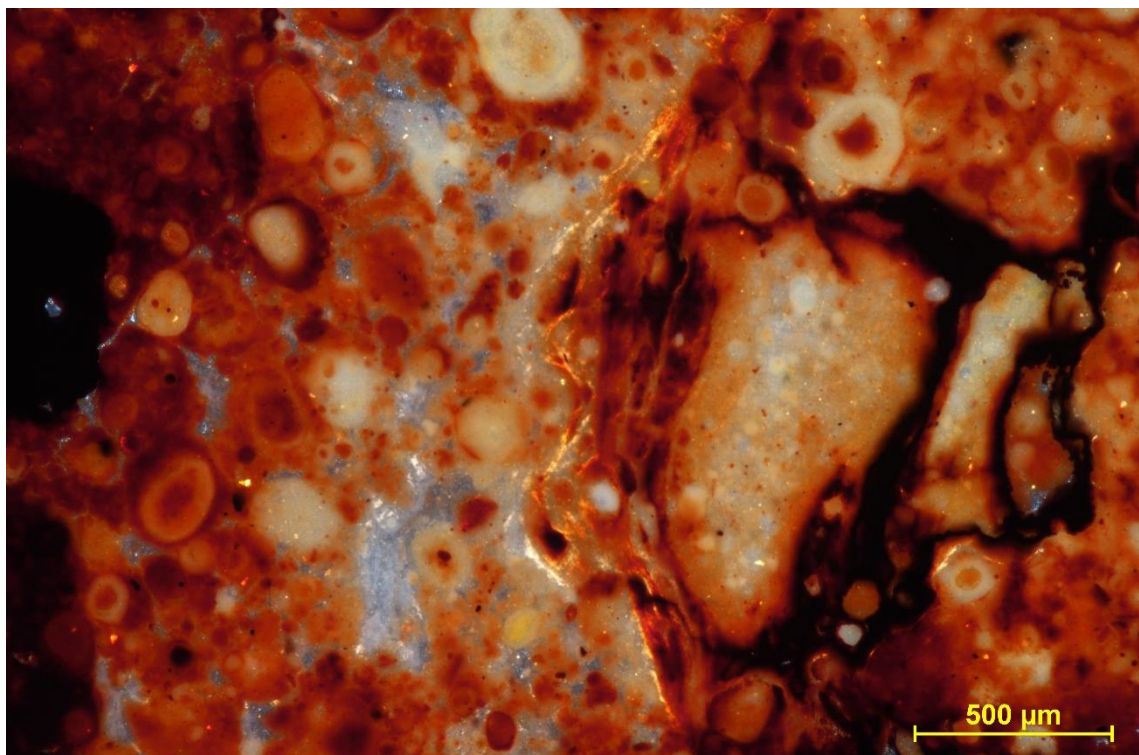


PER-1



Very similar to JM-1 but the amount of iron oxide is higher, giving a redder colour. Big particles are bigger than in JM-1. Is very difficult to find quartz

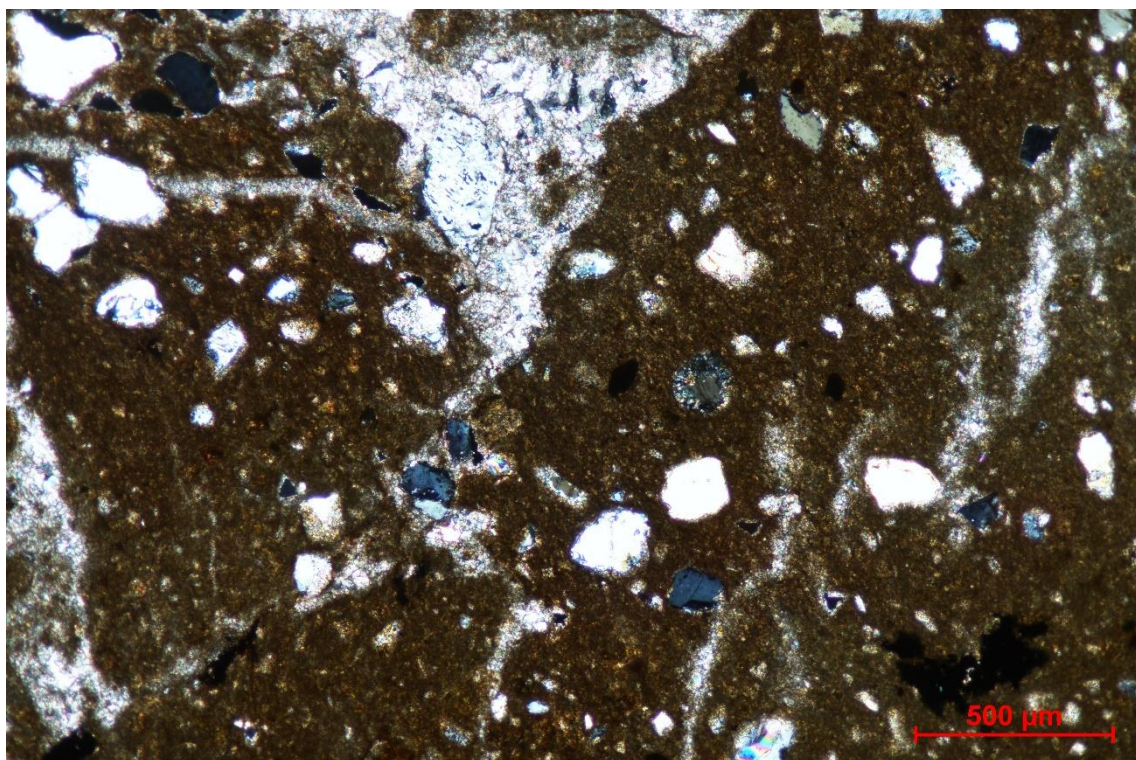


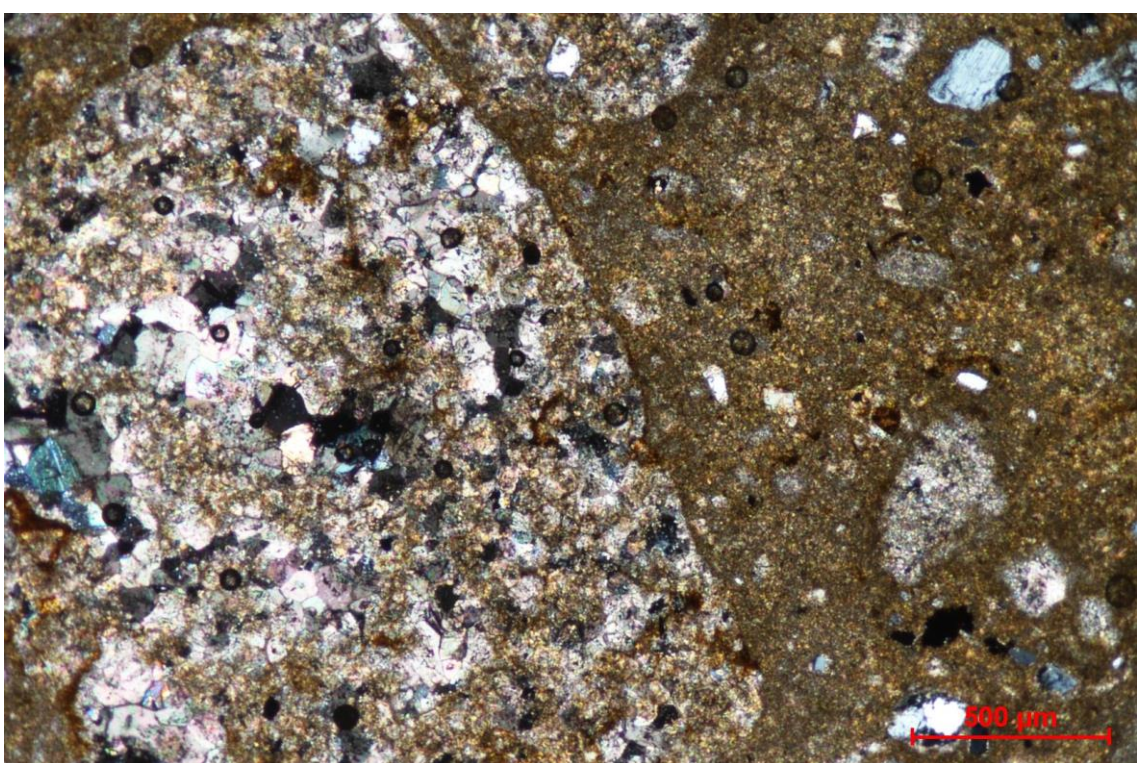
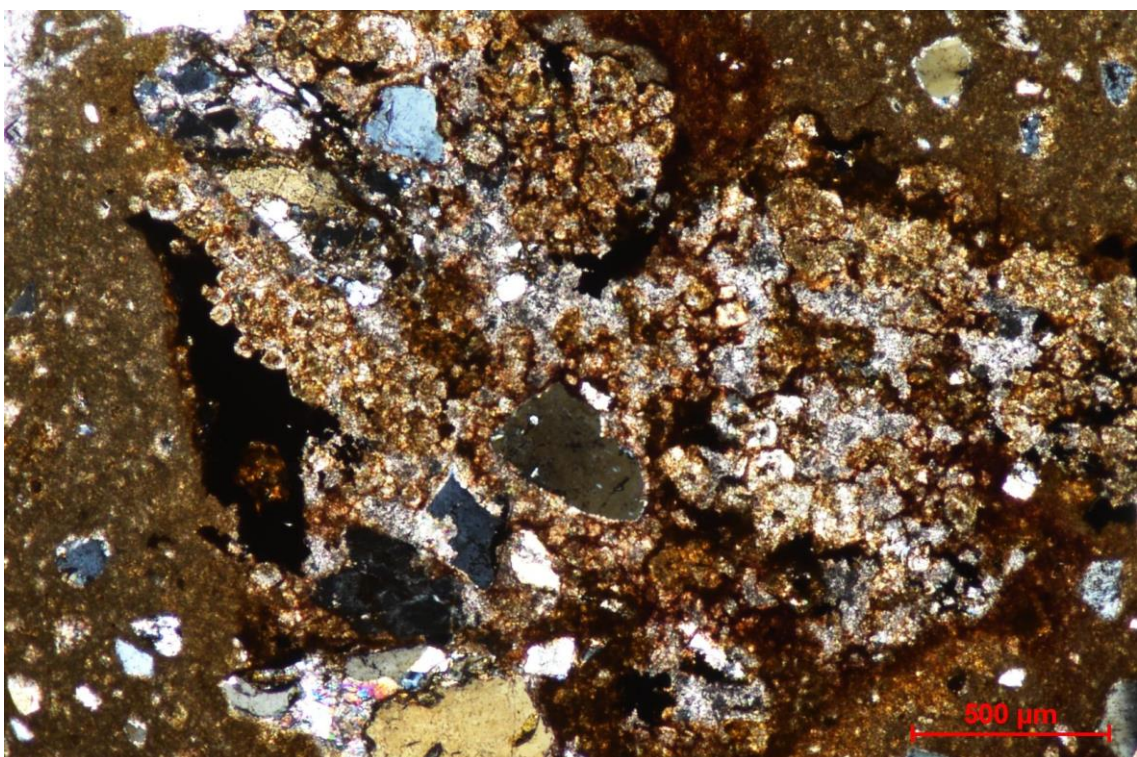


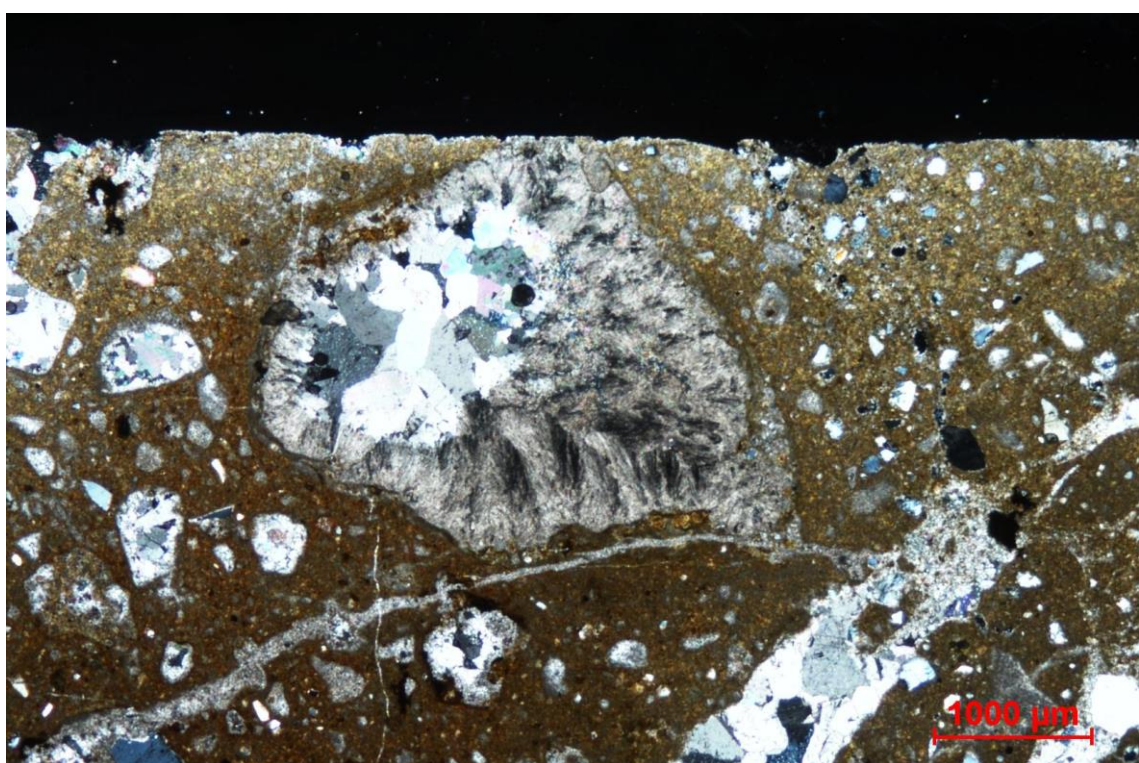
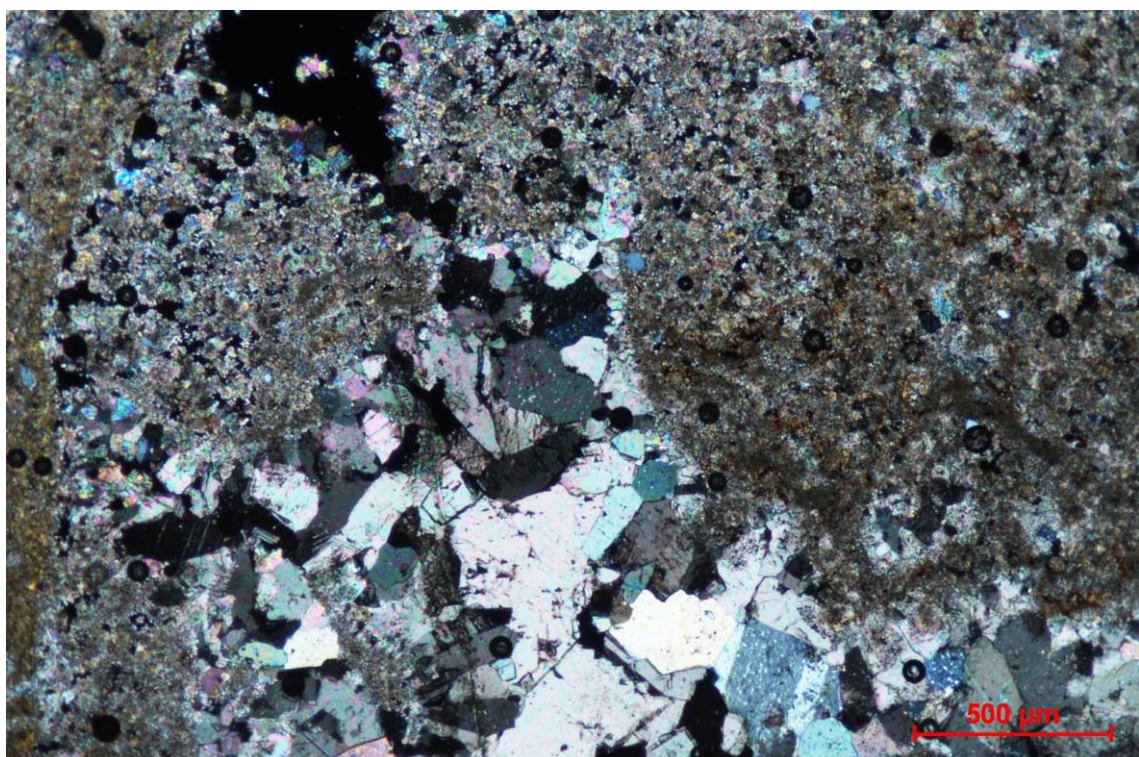
PER-2B



A sample different from previous ones. Iron and aluminium oxides are less important. The main minerals spotted are quartz and a micritic matrix which is most probably a kaolinite and/or other clay minerals. Particle size is lower than the other samples, looking as a more altered sample. At some points feldspars can be observed, being a minority.







Mineralogical composition

Semiquantitative analysis from XRD interpretation (mass%)

	Kaolinite group	Quartz	Bohemite	Hematite	Rutile	Anatase	K-Feldspar	Calcite	Muscovite	Biotite	Zircon	Gypsum	Sericite	Dolomite
PER 3	68		15	13		4								
JM-1	59		25	12		4								
PER 11 A	59		12	14	4	4		3			4			
PER 10 B	45		49		2	4								
PER 2B	43	50		4	3									
PER 14 3	42		1	3	2						3	49		
PER 15 2	41	4	25	11	3	4		10						3
PER 15 1	40		31	22	4	3								
JM-2	32		8	6				54						
PER 14 1	30		31	16		3		20						
PER 15 4	30	6	35	12	3	3		11						
PER 1	25		54	14	3	4								
PER 10 V	24		49	20	4	4								
PER 15 3	23		61	15		1								
PER-2C	14					5	1							80
PER 10 G	9	60	1		3		7	14	6					
PER 11 B	5	42			1			6	39	7				
PER-2A		85				15								

FTIR

Theoretical Kaolinite + autors	Theoretical bohemita + autors	PER-1	PER-2A	PER2-B	PER-2C	PER-3	JM-1	PER 10B	PER 10 G	PER 10 V	PER11- A	PER11 B	PER14-1	PER14-3	PER15- 1	PER15-2	PER15-3	PER15-4	Assigment	
3670-56		3693.49	3695.08	3698.64	3940.58	3695.47	3696	3694.6	3696.69	3693.19	3694.68	3697.44	3694.23	3697.35	3693.21	3695.28	3694.23	3693.83	Al-OH stretching	
			3668																Al-OH stretching	
3645		3653.77	3648.17	3654.2		3655	3654	3653		3648.03	3654.52		3654.15	3651.94	3652.17	3654.98	3651.19	3654.5	Al-OH stretching	
3620		3622.07	3620.51	3625.2	3621.43	3623.03	3622	3622	3621.4	3620.68	3622.52	3622.51	3622.05	3622.86	3621.08	3622.43	3622.47	3622.31	Al-OH stretching	
	3295				3301.63	3299.19	3300	3300.26	3301.85	3296.52	3296.34		3298.3		3290.32	3298.04	3302.49	3297.01	Al-OH stretching	
	3090	3103.3				3104.26	3037	3101.34		3105.02	3101.24		3099.2		3093.46	3100.08	3107.1	3101.46	Al-OH stretching	
					2983.92				2985.62			2987.37							(Calcite)	
					2875.37				2876.75			2875.98								
					2515.06				2511.87			2512.43	2513.76			2515.72		2517.35		
					2237.17				2228.21			2228.48								
					2136.72				2134.86			2137.14	2098.59							
					2090.1				2075.09	2088	2089.09	2093.16	2083.45			2094.68	2086.73	2095.02	2094.99	C=O
	1969.59	1991.94				1939.94	1970	1970.57	1973.29	1971.34	1935.54	1973.71	1970.35			1970.34	1970.84	1970.3	1970.45	
					1870.99	1822.67			1823	1824	1820.91	1869.32		1822.18	1870.76					
	1782.58	1790.59								1800.06			1796.15	1795.32	1821.53	1815.71	1799.04	1815.33	1796.11	
					1681.67					1795.27										
1638		1637.69	1611.64	1638.71	1629.43	1638.07	1639	1638.72	1617.09	1636.49	1640.62	1624.83	1640.37	1638.18	1638.32	1640.49	1642.24	1638.83	H-O-H stretching	

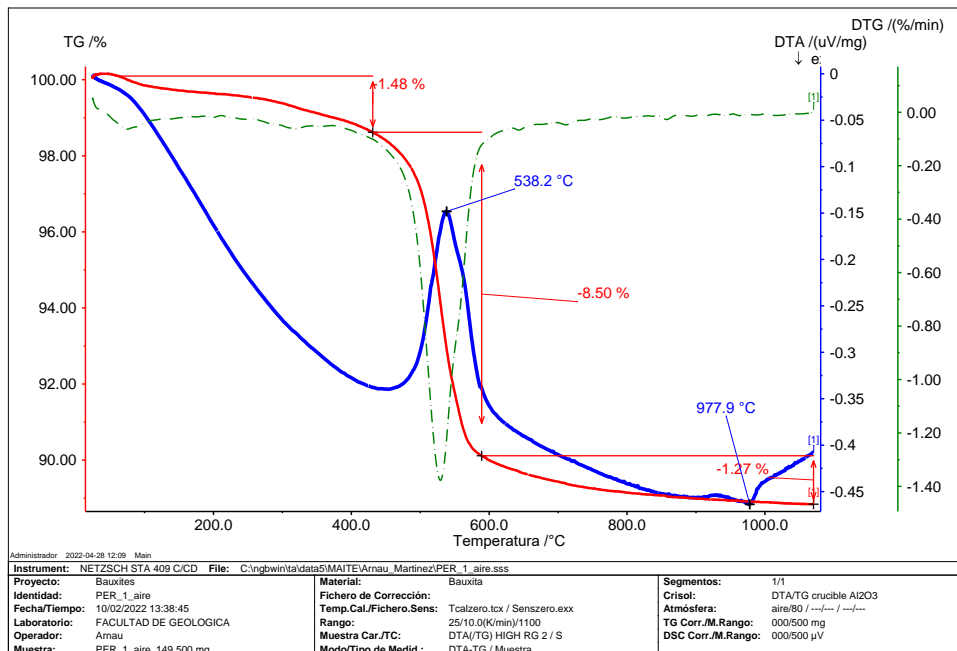
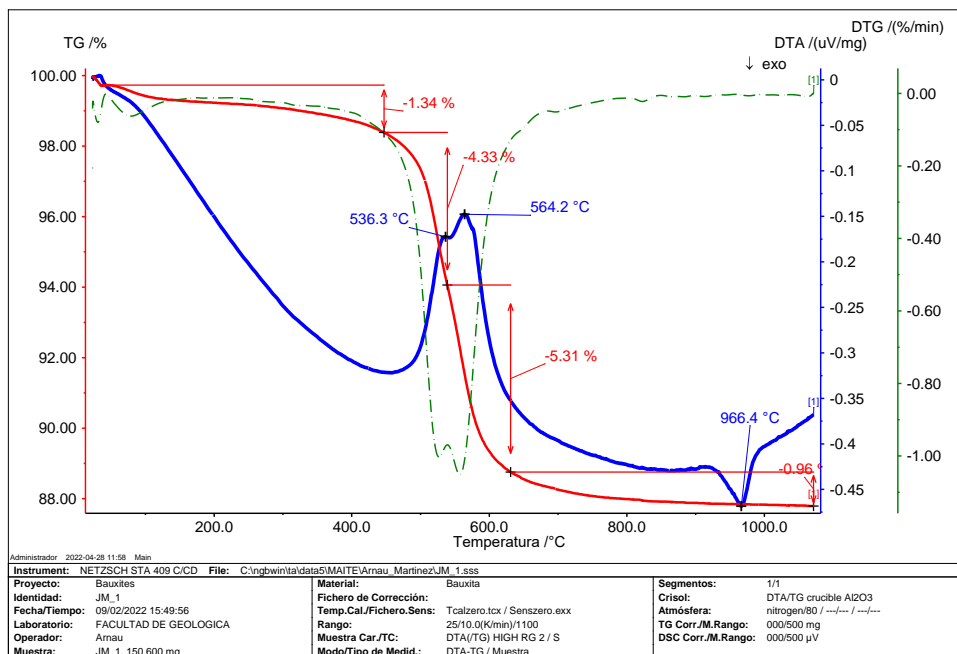
		1447.03	1487.56		1445.04		1439	1446.41	1559.09	1453.28	1447.45		1559.1	1456.89	1464.71	1414.36	1450.59	1450.34	1446.88	1451.74		
				1268.47								1391.53		1279.61								
				1184.03																		
		1160		1159.37	1159.65	1160.65	1164.06	1172		1183.19											H-O-H stretching	
1117-05				1107.71			1112.06		1111.89	1109	1111.33	1108.2	1109.13	1110.23	1111.47	1107.99	1111.02	1109.62	1109.58	1110.06	1110.26	Si-O stretching
																					Si-O stretching	
		1067	1073.5																		H-O-H stretching	
1035-30		1034*		1037.54		1030.9															Si-O stretching	
				1019.83			1019.53		1020.09	1018	1016.82	1009.97	1013.66	1019.97			1019.15		1018.97		1038.81	Si-O stretching
1019-05				944.75			995.8		995.57	948	945.72	936.17		942.25	998.26							Si-O quartz
									946.91		925.83	919.63									Si-O quartz	
									930.56												Si-O quartz	
918-09		919.49		924		914.58						914.42		922.26	922.7	928.45	923.64	924.87	922.47	920.88	OH deformation	
		879.89				877.07					875.65		865.94	876.27	876.67				878.34	876.81	876.46	OH deformation
						848.42						830.23									OH deformation	
800-784		820.78																			OH deformation	
				809.36	802.81			804	809.3	808.95				809.62						812.91	OH deformation	
		748*		793.94		780.72	794.15		750.89		753.01	793.44					789.5			744.45		

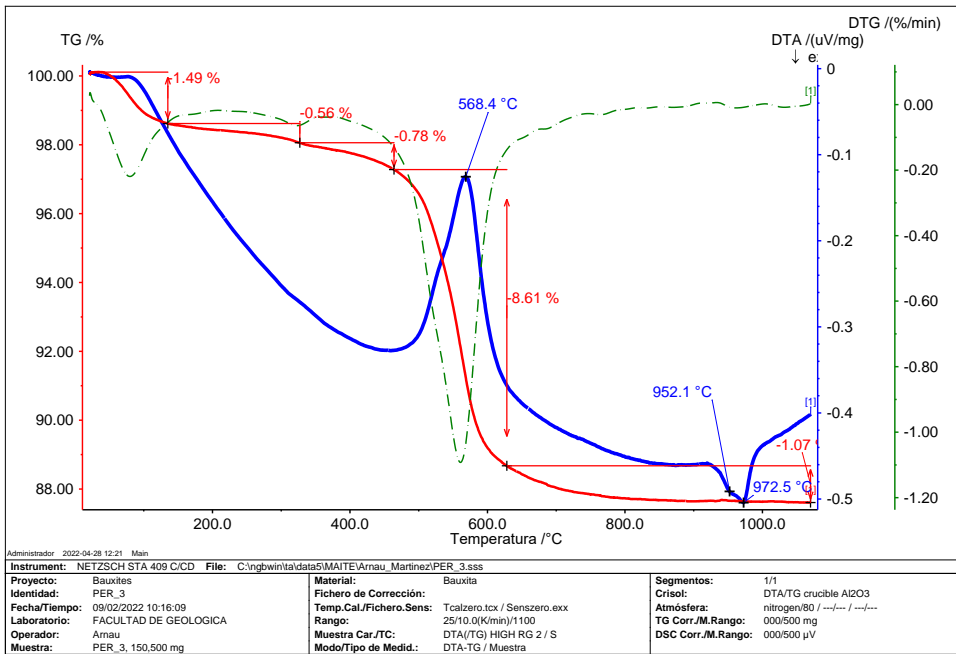
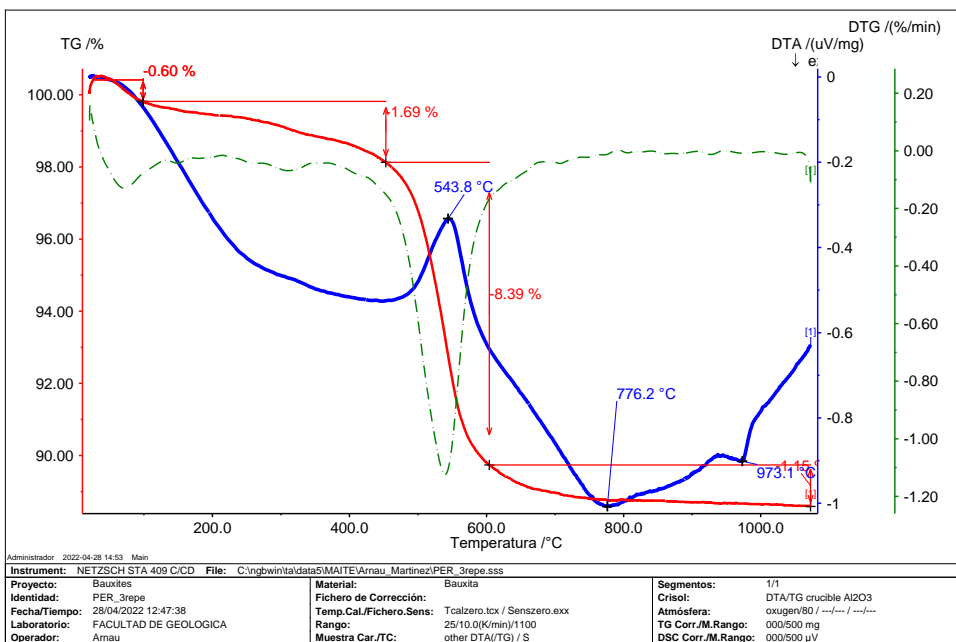
	730	728.48	729.41			715.01	715.79	732	721.01	712.25	713.02	714.39	715.12	712.88	711.51	733.63	724.06	720.02	713.48	719.89	Si-O-Al stretching	
700-686			722.14			715.01	715.79	717	717	712.25	713.02	714.39	715.12	712.88	711.51	733.63	724.06	720.02	713.48	719.89	Si-O	
		709.53	698.07	698.47						697.81				696.13						707.14	Si-O	
			673.37	678.86																	Si-O	
			667.07	664.89																	Si-O-Al stretching	
524-35	624		644.53							594.9	568.85			577.43						545.29	559.29	Si-O-Al stretching
	539*	528.36			518.18	535.22														520.09		
			502.81	503.22	498.43	498.43		506				510.53		495.19		502.41	511.95	505.79	509.66			
475-68	490		491.16	486.55	489.03	489.03		496		496.8							496		493.32	494.1	Si-O-Al stretching	
			461.75	478.94	469.64	469.64		462.06		489	483.64								472.11		Si-O-Si bending	
			440.82	446.2	452.39	440.81		440.81		460								439.28	456.48		Si-O-Si bending	
430		425.6	432.87	430.78					431	420.58		425.34		435.98		428.2				438.83	405.97	Si-O Bending
			415.58	420.23															418.51		Si-O	
			404.27	410.31																		

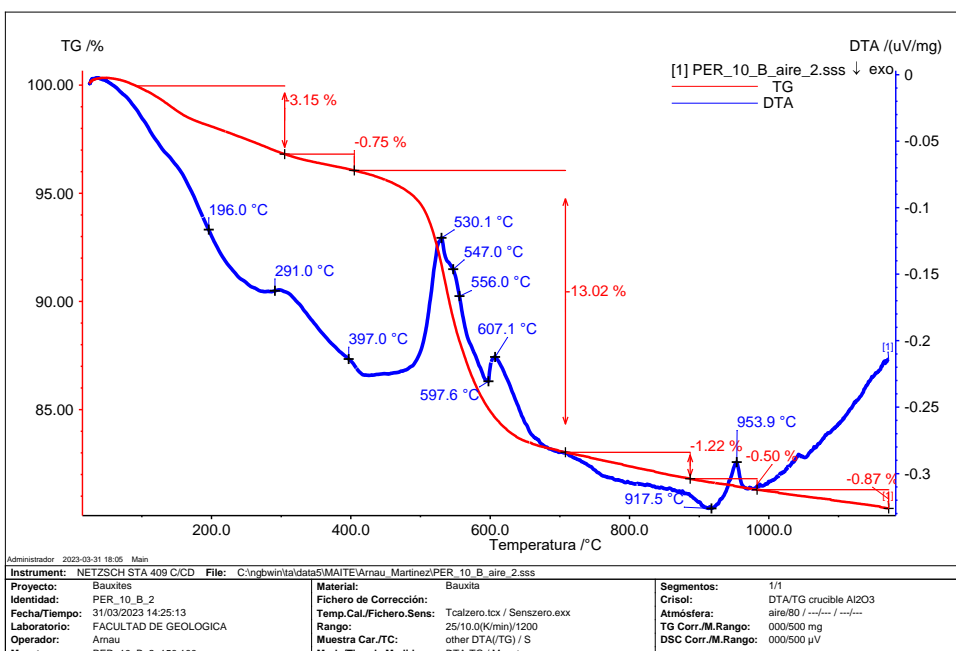
Thermal Properties

ATD-TG

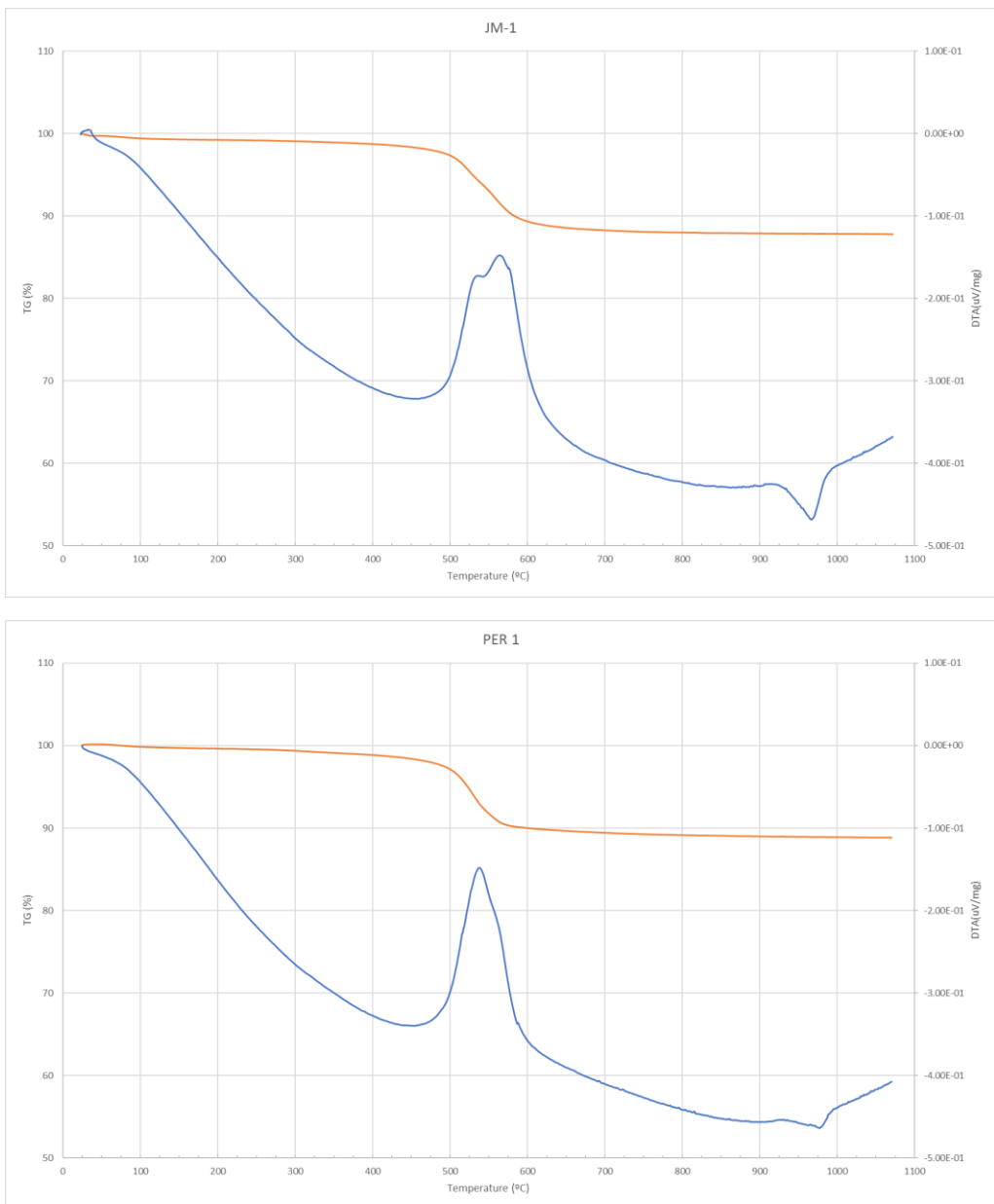
Plots generated from measuring devise.

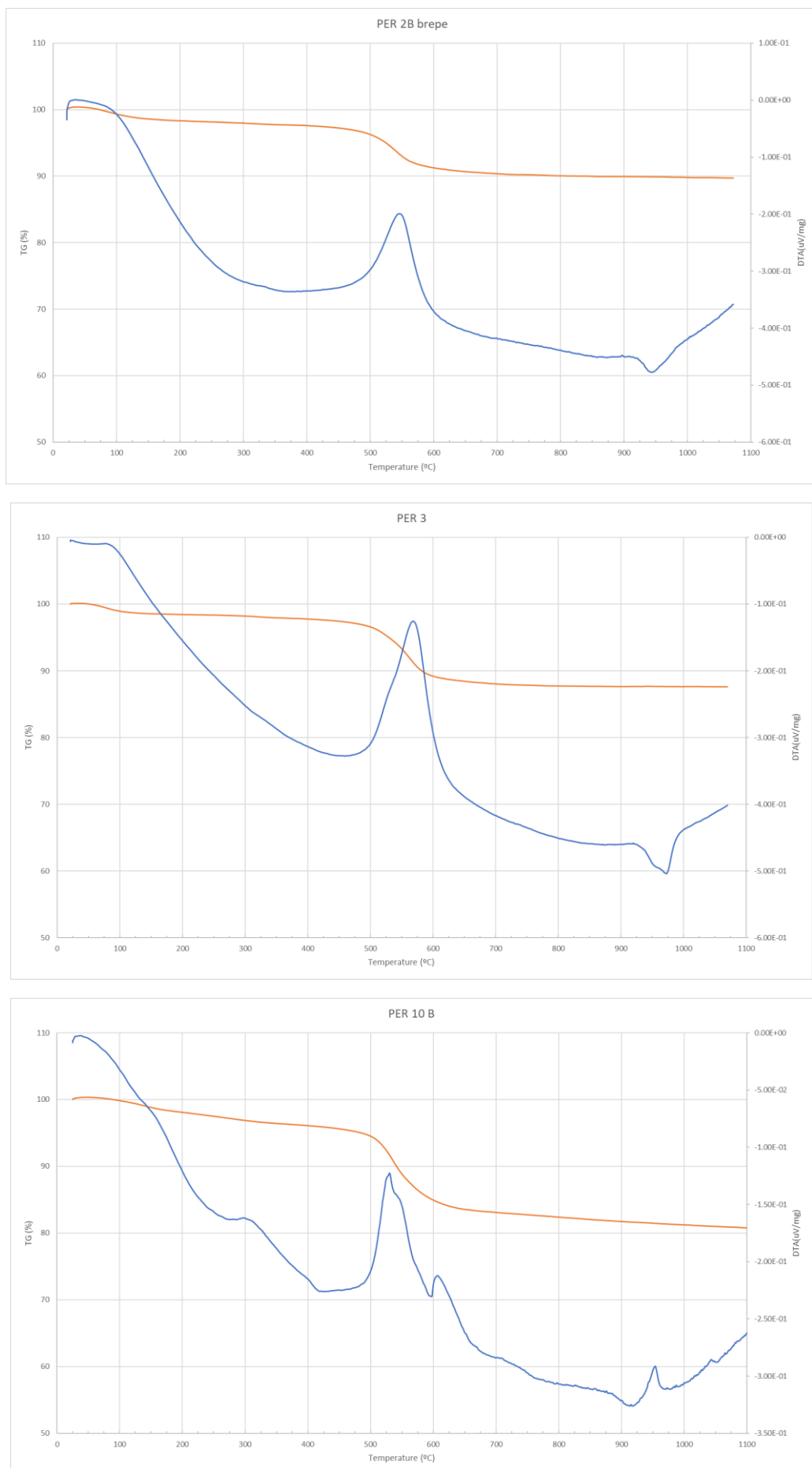




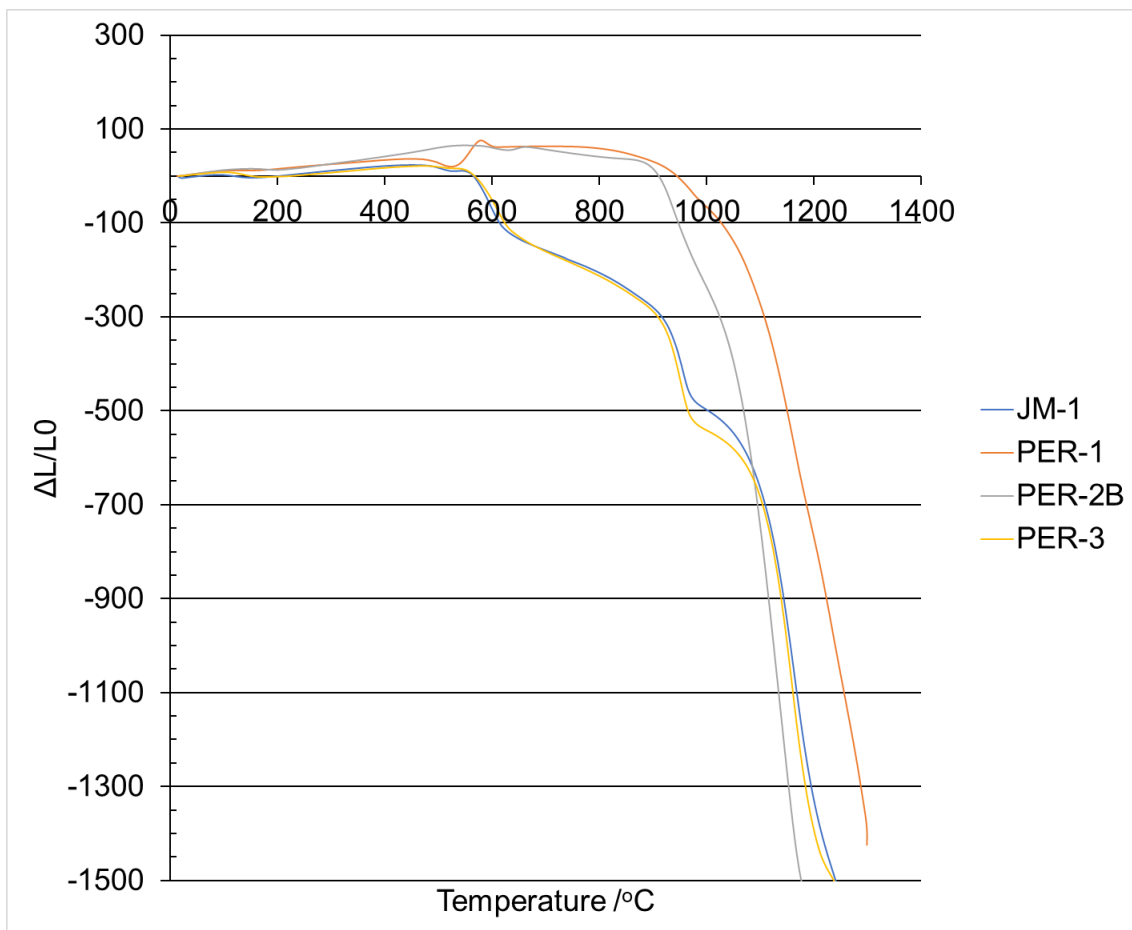


Plots Generated from .txt files.



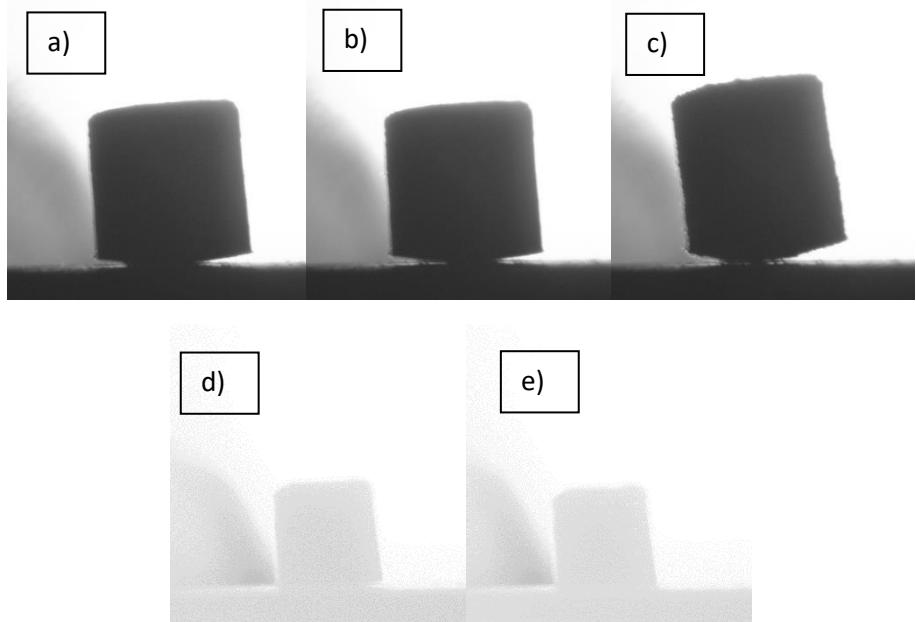


Dilatometry



HSM

PER-1



a) 360 °C First shrinkage.

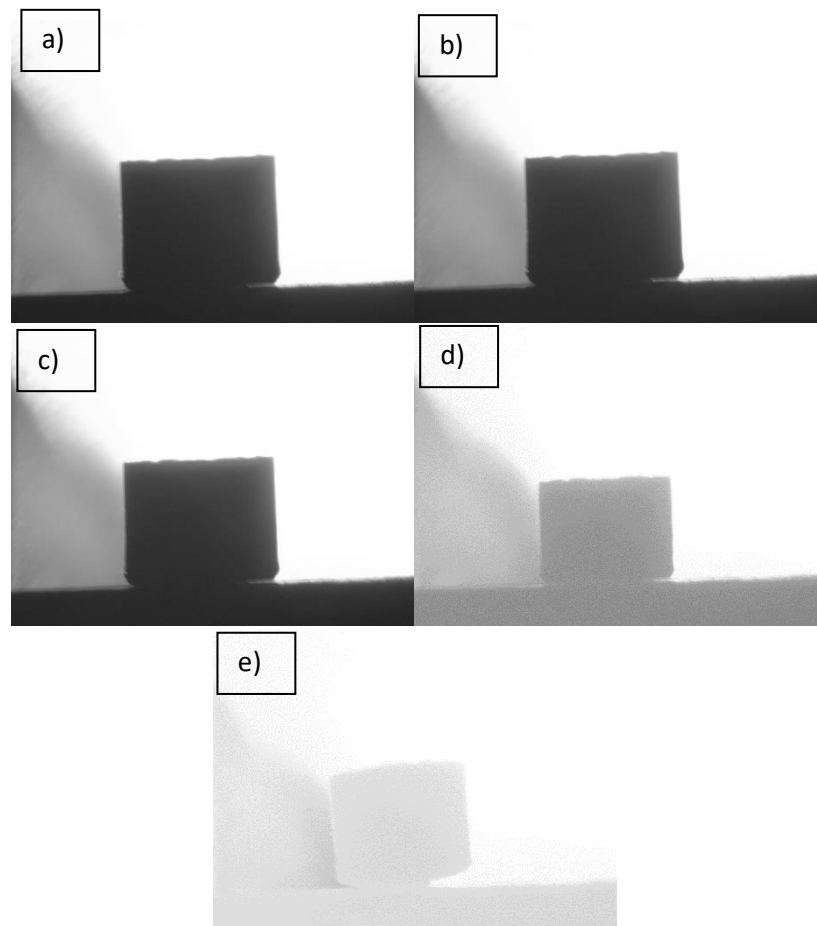
b) 571 °C Begining of expansion.

c) 775 °C Max. expansion.

d) 1439 °C Softening.

e) 1439 °C End.

PER-2B



- a) 265 °C Beginning.
- b) 954 °C Shrinkage.
- c) 1000 °C
- d) 1325 °C Final Shrinkage.
- e) 1450 °C Softening.

Tables

PER-1

Image	T (°C)	Area	Max Lon	Max hight	Area Dif	Stage
1	299	8.95	3	3.11	100.000%	
3	329	8.92	2.98	3.11	99.665%	
5	360	8.86	2.95	3.1	98.994%	First shrinkage
10	435	8.66	2.92	3.06	96.760%	
15	510	8.56	2.89	3.03	95.642%	
17	541	8.53	2.87	3.03	95.307%	
18	556	8.53	2.86	3.03	95.307%	
19	571	8.49	2.9	3.04	94.860%	
20	586	8.52	2.88	3.06	95.196%	
21	601	8.61	2.87	3.09	96.201%	
22	616	8.71	2.89	3.11	97.318%	Beginning expansion
25	661	8.89	2.91	3.15	99.330%	
28	707	9.23	2.95	3.25	103.128%	
30	741	9.79	3	3.4	109.385%	
40	744	9.81	3	3.39	109.609%	
106	760	9.97	3.03	3.48	111.397%	
166	775	10.05	3.01	3.54	112.291%	Max expansion
226	790	10.01	3	3.52	111.844%	
266	800	10.01	3	3.5	111.844%	
326	815	9.98	2.97	3.52	111.508%	
366	825	9.98	2.99	3.449	111.508%	
466	850	9.93	3	3.51	110.950%	
666	900	9.73	2.96	3.44	108.715%	
866	950	9.45	2.91	3.4	105.587%	
1066	1000	9.26	2.89	3.4	103.464%	
1467	1100	8.64	2.75	3.26	96.536%	
1867	1200	7.98	2.67	3.15	89.162%	
2267	1300	7.34	2.55	3.01	82.011%	
2367	1325	6.93	2.47	2.95	77.430%	
2467	1350	6.4	2.4	2.79	71.508%	
2567	1375	5.81	2.3	2.66	64.916%	
2667	1400	5.03	2.15	2.45	56.201%	
2767	1425	4.27	2.02	2.19	47.709%	
2825	1439	3.84	1.95	1.99	42.905%	Softening
2831	1441	3.78	1.94	1.98	42.235%	
2867	1450	3.46	1.84	1.89	38.659%	

PER 2B

Imatge	T (°C)	Area	Max Lon	Max hight	Area Dif	Stage
1	265	7.35	3	2.47	100.000%	
9	384	7.35	3	2.47	100.000%	
20	549	7.35	3	2.46	100.000%	
30	699	7.31	2.95	2.46	99.456%	
350	800	7.3	2.95	2.47	99.320%	
550	850	7.31	2.96	2.44	99.456%	
750	900	7.31	3	2.46	99.456%	
950	950	7.31	3	2.46	99.456%	
962	953	7.29	2.99	2.46	99.184%	
966	954	7.27	2.99	2.46	98.912%	First shrinkage
970	955	7.25	2.99	2.46	98.639%	
990	960	7.23	2.99	2.46	98.367%	
1030	970	7.21	2.97	2.43	98.095%	
1151	1000	6.95	2.92	2.38	94.558%	
1551	1100	6.3	2.8	2.28	85.714%	
1951	1200	5.49	2.61	2.11	74.694%	
2351	1300	5.11	2.56	2	69.524%	
2420	1317	5.07	2.55	1.99	68.980%	
2432	1320	5.07	2.55	1.99	68.980%	
2452	1325	5.07	2.55	2	68.980%	Softening
2552	1350	5.11	2.59	2.01	69.524%	
2752	1400	5.81	2.59	2.35	79.048%	
2952	1450	5.93	2.62	2.38	80.680%	

PER 3

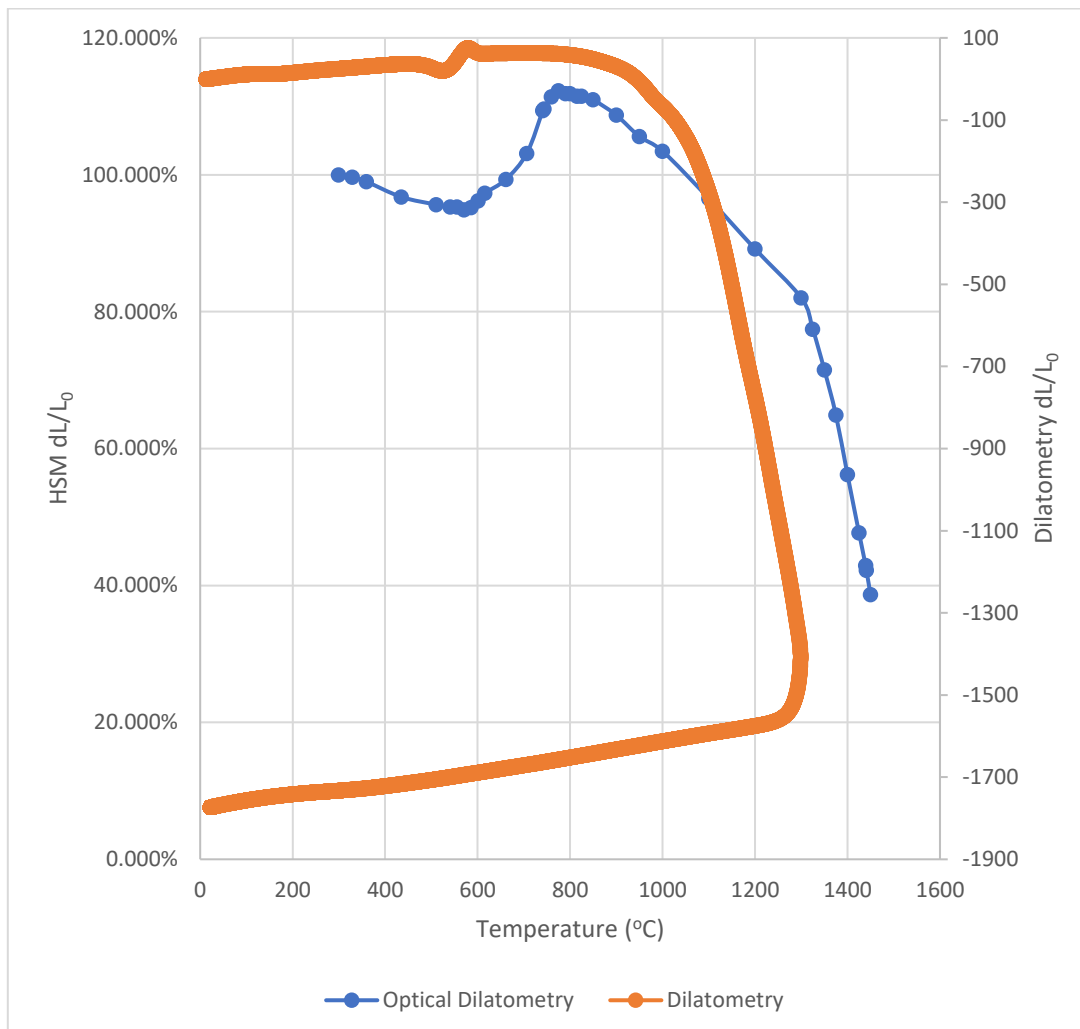
Imatge	T (°C)	Area	Max Lon	Max hight	Area Dif	Stage
1	246	9.53	3	3.22	100.000%	
5	297	9.44	2.98	3.18	99.056%	First shrinkage
10	361	9.41	2.97	3.14	98.741%	
21	501	9.15	2.92	3.11	96.013%	
519	700	9.03	2.91	3.11	94.753%	
897	800	9	2.89	3.11	94.439%	
1275	900	8.95	2.85	3.13	93.914%	
1369	925	8.81	2.84	3.09	92.445%	
1464	950	8.57	2.8	3.09	89.927%	
1653	1000	8.38	2.76	3.05	87.933%	Stop Expansion
1842	1050	8.31	2.76	3.04	87.198%	Beginning shrinkage
2031	1100	8.09	2.72	2.97	84.890%	
2220	1150	7.43	2.61	2.86	77.964%	
2409	1200	7.07	2.55	2.77	74.187%	
2598	1250	6.84	2.5	2.77	71.773%	
2788	1300	6.43	2.46	2.66	67.471%	
2977	1350	6.11	2.37	2.59	64.113%	
3166	1400	5.64	2.26	2.51	59.182%	
3355	1450	5.16	2.24	2.36	54.145%	

JM-2

Imatge	T (°C)	Area	Max Lon	Max hight	Area Dif	d	t	t/d	max W/max H	Mhi/MH1	Stage
1	295	7.12	3	2.37	100.000%						
30	729	7.11	3	2.34	99.860%				1.282	0.987	
100	763	7.05	3.03	2.32	99.017%				1.306	0.978	First shrinkage
500	863	7.02	3.02	2.35	98.596%				1.285	0.991	
530	870	7.05	3.03	2.34	99.017%				1.294	0.987	
550	875	6.99	3.01	2.31	98.174%				1.303	0.974	
600	888	6.86	3	2.29	96.348%				1.310	0.966	
650	900	6.69	2.98	2.24	93.961%				1.330	0.945	
700	912	6.49	2.9	2.22	91.152%				1.306	0.936	
800	937	6.02	2.83	2.13	84.551%				1.328	0.898	
900	962	5.93	2.8	2.12	83.287%				1.320	0.894	
1000	987	5.84	2.79	2.09	82.022%				1.334	0.881	
1050	1000	5.84	2.79	2.09	82.022%				1.334	0.881	
1400	1087	5.9	2.8	2.1	82.865%				1.333	0.886	
1850	1200	5.84	2.78	2.1	82.022%				1.323	0.886	
1875	1206	5.77	2.78	2.07	81.039%				1.342	0.873	
1900	1212	5.77	2.78	2.07	81.039%				1.342	0.873	
2000	1237	5.68	2.75	2.07	79.775%				1.328	0.873	
2100	1262	5.26	2.67	1.99	73.876%				1.341	0.839	
2200	1287	4.6	2.49	1.85	64.607%				1.345	0.780	
2250	1300	4.08	2.33	1.76	57.303%				1.323	0.742	
2300	1312	3.72	2.26	1.67	52.247%				1.353	0.704	
2321	1318	3.78	2.25	1.68	53.090%				1.339	0.708	
2331	1320	3.87	2.28	1.75	54.354%				1.302	0.738	Softening
2349	1325	4.46	2.29	2.11	62.640%	3.35	2.92	0.871	1.085	0.890	
2363	1328	4.7	2.61	2.11	66.011%	3.36	2.88	0.857	1.236	0.890	Ball
2443	1348	3.62	2.33	1.87	50.843%				1.245	0.789	
2512	1365	3.25	2.3	1.69	45.646%				1.360	0.713	
2513	1366	2.19	3.05	0.99	30.758%				3.080	0.417	Half Ball
2515	1366	1.96	3.26	0.88	27.528%				3.704	0.371	
2520	1367	1.79	3.29	0.8	25.140%				4.112	0.337	
2550	1375	0.97	2.98	0.48	13.624%				6.208	0.202	
2564	1378	0.73	2.98	0.37	10.253%				8.054	0.156	Flow

PER-1

Comparison between HSM results and dilatometry results.



Technological Properties Gresification curves

Tiles before test



Tiles after firing test

